ISSN: 2708-7956

الأكاديمية
للهندسة والعلوم

Academic
For Engineering and Science

مجلة علمية محكمة فصلية
تصدر عن نقابة الأكاديميين العراقيين
المجلد (4) العدد (2)
حزيران - السنة 2022

رقم الإيداع في الدار الوطنية
2422 لسنة 2020

الأكاديمية للعلوم الهندسية والعلوم
http://aphjournal.iraqiacademic.com
ISSN: 2708-7956 DOI prefix: 10.47719

الأكاديمية

للهندسة والعلوم

Academic

For Engineering and Science

مجلة علمية محكمة فصلية

تصدر عن نقابة الأكاديميين العراقيين

المجلد (4) العدد (2)

1 /6/ 2022

كـــلمة العدد (2) لسنة (2022)

يسعدنا ان نقدم لكم **العدد الثاني/ السنة 2022** لمجلة **الأكـاديمـية للهندسة والعلوم**. أود أن اسجل شكري الجزيل للجهود الكبيرة لكل من ساهم في إظهار هذا العدد. كما أتقدم بالشكر لجميع الباحثين الذين دعموا المجلة من خلال نشر أبحاثهم فيها، خاصاً بعد حصول المجلة على الرقم المعّرف **DOI** في عام 2020.

ضم هذا العدد، بحوث في مختلف المجالات العلمية، هي: الهندسة، والفيزياء، والاستشعار عن بعد، التحليل الإحصائي والرياضيات.

نأمل أن تحقق مجلة الأكاديمية للهندسة والعلوم، من خلال هذه الطبعة، تطلعات الباحثين والمهتمين، وأن نسعى، بعون الله تعالى، إلى تطوير مجلتنا نحو الأفضل، وأن يكون لها حضورا علميا متميزا إقليمياً وعالمياً، ونتطلع ان تكون المجلة في التصنيفات العلمية الدولية.

مع خالص التقدير

أ. د. أحمد كمال أحمد
رئيس هيئة التحرير
حزيران - 2022

نبـــــذة عن
نقابة الاكاديميين العراقيين

أسست نقابة الأكاديميين العراقيين بموجب القانون رقم (61) لسنة (2017)، بغية الاهتمام بالملاك التدريسي والأكاديمي (الأكاديمي: التدريسي الحاصل على شهادة الماجستير أو الدكتوراه ويمارس مهنة التدريس أو يعمل بمراكز البحث العلمي في الجامعات).

والارتقاء بمستوى العاملين في هذا القطاع الحيوي وإعداد الخطط والسياسات التي ترتقي بالعملية التدريسية ومن أجل إنشاء مجالس ونقابات تهتم بشؤون الأكاديميين والدفاع عنهم وحفظ كرامتهم وضمان حرياتهم الأكاديمية، ومن أجل رفع سمعة الجامعات والمعاهد العراقية ومساواتها مع مثيلاتها في الدول المتحضرة. ووفقاً للمادة –2– من البند الثاني من قانونها فأنها:

أولاً: تتمتع نقابة الأكاديميين العراقيين بالشخصية المعنوية والاستقلال المالي والإداري يمثلها (نقيب الأكاديميين العراقيين) أو من يخوله.

ثانياً: يكون مركز النقابة في بغداد ولها فتح فروع في المحافظات وحيثما تقتضي مصلحة النقابة إيجاد تمثيل.

ثالثاً: لأعضاء الهيئات التدريسية في الجامعات والمعاهد العراقية المعترف بها من وزارة التعليم العالي والبحث العلمي الانتماء إلى النقابة.

ووفقاً للمادة –3– فأن أهداف تأسيس النقابة هي:

أولاً: الارتقاء بمهنة التعليم العالي والبحث العلمي لتحقيق رسالتها في خدمة الوطن وأجيال الأمة.

ثانياً: التنسيق والتعاون مع وزارة التعليم العالي والبحث العلمي والجهات ذات الصلة بما يحقق مهام النقابة.

ثالثاً: تعزيز أخلاقيات مهنة التعليم العالي والمحافظة على آداب وتقاليد وشرف المهنة.

رابعاً: تشجيع الدراسات والبحوث والنشاطات والمؤتمرات التعليمية وعقد الدورات والندوات لرفع المستوى العلمي والمهني لتدريسي الجامعات والمعاهد العراقية.

خامساً: تعزيز مكانة الأكاديميين في المجتمع والدفاع عن حقوقهم ومصالحهم وكرامتهم.

سادساً: النهوض والارتقاء بالأعضاء مهنياً واقتصاديا وثقافياً واجتماعياً.

سابعاً: تأسيس صندوق للتكافل الاجتماعي لمساعدة أعضاء النقابة، يؤمن لهم ولأسرهم العيش الكريم في حالات العجز الكامل أو الوفاة وتوفير الرعاية الصحية للأعضاء وأسرهم.

ثامناً: التعاون وتوطيد العلاقات مع الاتحادات العربية والدولية المماثلة.

أ. م. د. مهـند الهـلال
نقيب الاكاديميين العراقيين

المحتوى (العدد 2 لسنة 2022)

أهداف ورؤية المجلة Aims and Scope

- تنشر المجلة الدراسات العلمية ذات الأفكار الأصيلة والحديثة والمتجددة، ويحوت الرسائل والأطروحات، التي لم يسبق نشرها أو المساهمة بها في أحد الملتقيات العلمية، وان تكون هذه البحوث مندرجة ضمن أحد المحاور تخصصات الهندسية والعلوم الصرفة.
- كما تنشر المجلة الكتب المؤلفة والمترجمة ضمن التخصصات أعلاه.

الوصول المفتوح للبحوث Open Access Policy

مجلة **الأكاديمية للهندسة والعلوم** هي مجلة مفتوحة الوصول، بالتالي لا توجد رسوم مطلوبة لتنزيل أي منشور من موقع المجلة من قبل المؤلفين والقراء والمؤسسات، وعلى الموقع:
http://aphjournal.iraqiacademic.com/Journal/GetAllVersions

قواعد النشر:

- البحوث المرسلة إلى المجلة يجب أن تكون سليمة من الأخطاء اللغوية والمنهجية والمعرفية، وملتزمة بالأعراف العلمية المتبعة، ولم يسبق نشرها.
- لا ينبغي أن يتحاوز عدد صفحات البحث عن خمسة عشر ورقة من حجم B5.
- في حالة وجود هوامش في اسفل الصفحة ينبغي اعتماد ترقيم آلي يتجدد في كل صفحة.
- يتضمن البحث ملخصين: الأول بلغة البحث، والثاني باللغة العربية أو الإنجليزية.
- تخضع جميع البحوث للتحكيم العلمي على نحو سري، ويخبر الباحث إما بقبول بحثه، أو بالقبول المشروط ببعض التعديلات التي يبلغ بها، أو بالرفض. وفي هذه الحالة الأخيرة؛ فإن المجلة ليست ملزمة ببيان الأسباب.

توصيات تقنية في كتابة البحوث:

- مقاس الورقة والهوامش: الورقة حجم B5، ويترك هامش بمسافة 2 سم من حواشي الورقة. مع مسافة 1 سم بين الأسطر في المتن والهوامش.
- يُعتمد الخط **Simplified Arabic** (البحوث باللغة العربية)/ و**Times New Roman** (البحوث باللغة الإنكليزية)، مقاس 16 غامق عنوان البحث، مقاس 14 غامق العناوين الأساسية، مقاس 12 غامق العناوين الفرعية، وبمقاس 12 في المتن، مقاس 11 غامق لعناوين الأشكال والجداول، 10 في الحواشي.

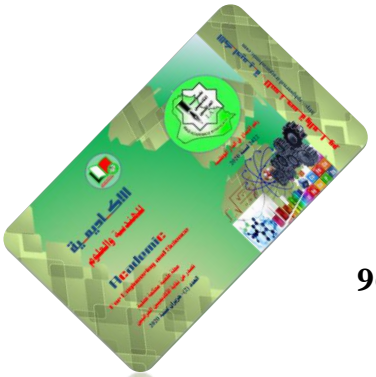

معلومات الاتصال:

- **موقع المجلة:** http://aphjournal.iraqiacademic.com/

ISSN: 2708-7956, DOI prefix: 10.47719

- **البريد الإلكتروني للمجلة:** info@iraqiacademics.iq
dr.ziadmabood@gmail.com

- **أرقام الهواتف: 9647709298631 -9647902746409**

- **رقم الإيداع في الدار الوطنية 2422 لسنة 2020**

A Comparison of PV Solar Module Performance in Two Iraqi Regions

Mohammed Jawad Yaseen[1, a], Naseer K. Kasim[2,b], Ahmed F. Atwan[3, c]
[1, 3] Physics Department, College of Education, Mustansiriyah University, Baghdad, Iraq
[2]Training and Energy Research Office, Ministry of Electricity, Baghdad, Iraq
[a]m1964jy@uomustansiriyah.edu.iq, bbirss2004@yahoo.com,
[c]Ahmed1973@uomustansiriyah.edu.iq
[a] Corresponding Author: m1964jy@uomustansiriyah.edu.iq

Abstract:

The rising demand for electrical energy in Iraq, as well as the severe shortage of processing hours for citizens, particularly during the summer, and the significant environmental pollution it causes, means that the Iraqi government is tending toward clean energy (environmentally friendly). A study was carried out to evaluate the PV solar module's performance in two different regions of Iraq. The first is Abu Al-Khaseeb, which is located in southern Iraq in the province of Basra and is distinguished by its low altitude of 3 (m) above sea level, its high humidity, and the temperature in the summer, while the second is Daquq, which is located in northern Iraq in Kirkuk province and is distinguished by its higher altitude of 150 (m) and the lower temperature and humidity in summer. This study is based on real data collected from two metrological stations in 2019 that includes all influencing weather conditions such as winds, clouds, dust, humidity, and temperature, as well as values that were extracted by computer programs in MATLAB, such as the half-monthly rate for the cell temperature, output power, and electric efficiency. As a result, this work is a comparative study to show an investor interested in solar power stations how to choose the best among the two according to the data and results of the current study. The results of this study show that the performance of the PV solar module is similar in both areas studied, with the only difference being the environmental conditions. This indicates that the two areas are suitable for the construction of solar power plants to generate electricity.

Keywords: Solar radiation, PV solar module, Solar cell performance, Solar cell efficiency, Meteorological Station.

المستلخص:

إن الطلب المتزايد على الطاقة الكهربائية في العراق، فضلاً عن النقص الحاد في ساعات المعالجة للمواطنين، خاصة خلال فصل الصيف، والتلوث البيئي الكبير الذي يسببه، يعني أن الحكومة العراقية تتجه نحو الطاقة النظيفة (الصديقة للبيئة). تم إجراء دراسة لتقييم أداء وحدة الطاقة الشمسية الكهروضوئية في منطقتين مختلفتين من العراق. الأول هو أبو الخصيب الذي يقع في جنوب العراق في محافظة البصرة ويتميز بانخفاض ارتفاعه 3 م فوق مستوى سطح البحر وارتفاع نسبة الرطوبة ودرجة الحرارة في الصيف، أما الثاني فهو داقوق التي تقع في شمال العراق في محافظة كركوك وتتميز بارتفاعها العالي البالغ 150م وانخفاض درجة الحرارة والرطوبة في الصيف. تستند هذه الدراسة إلى بيانات حقيقية تم جمعها من محطتين مترولوجيتين في عام 2019 تضمنت جميع الظروف الجوية المؤثرة مثل الرياح والغيوم والغبار والرطوبة ودرجة الحرارة، وكذلك القيم التي تم استخلاصها بواسطة برامج الكمبيوتر في MATLAB، مثل النصف. المعدل الشهري لدرجة حرارة الخلية وطاقة الخرج والكفاءة الكهربائية. ونتيجة لذلك فإن هذا العمل عبارة عن دراسة مقارنة تبين للمستثمر المهتم بمحطات الطاقة الشمسية كيفية اختيار الأفضل بين الاثنين حسب بيانات ونتائج الدراسة الحالية. تظهر نتائج هذه الدراسة أن أداء وحدة الطاقة الشمسية الكهروضوئية متماثل في كلا المجالين المدروسين، مع الاختلاف الوحيد هو الظروف البيئية. وهذا يدل على أن المنطقتين مناسبتان لإنشاء محطات طاقة شمسية لتوليد الكهرباء.

الكلمات المفتاحية: الإشعاع الشمسي، الوحدة الشمسية الكهروضوئية، أداء الخلايا الشمسية، كفاءة الخلايا الشمسية، محطة الأرصاد الجوية.

1. Introduction

Internationally, there is a significant increase in energy consumption, especially electricity. The excessive use of fossil fuels in various aspects of life has led to an increase in the level of pollution in the atmosphere. The emission of gases associated with the combustion of fossil fuels has led to a rise in global temperature as a result of global warming. In other words, the world wants to give up the energy that causes pollution for clean and environmentally friendly energy like solar, wind, and other renewable energies for the generation of electrical power [1-4].

The output power from the PV solar module is affected by some factors, such as the high humidity that characterizes the city of Basra in southern Iraq compared to the low humidity of the city of Kirkuk in northern Iraq. These two cities are under the current study, as is dust and the high temperature that characterizes the Iraqi atmosphere, especially in the summer. These factors affect the performance of the PV solar module and reduce the efficiency of the PV solar panel. Investments in the construction of solar power plants should take these weather conditions into consideration [5, 6].

Despite the pessimistic picture, Iraq is one of the countries located in a high-density solar energy region, and most of its regions are suitable for building high solar energy plants [7-9]. Iraq possesses huge natural gas reserves, which will support the implementation of electric power generation projects as well as projects to build renewable energy plants [10]. Iraq has more than enough water to clean the solar plant of dust and bird droppings. In Iraq, massive amounts of electricity are currently required. In this situation, considering solar energy production and assisting with that generated by gas turbine stations at night is a brilliant and acceptable idea, see [11,14] for more information.

The price of depletable petrochemical fuels is increasing dramatically, which is unlike photovoltaic units whose prices are dropping rapidly, which led to their widespread use. It is believed that photovoltaic energy is useful and attractive only in isolated and remote areas [15–18].

2. Iraq Solar Energy Potential

Iraq's energy profile remains barred from patterns common to the pre-2003 period. Other than hydropower, the contribution of renewable energy is insignificant, with no clear steps to tap its renewable resources expected. Iraq has abounding solar energy potential with intensive daylight throughout the year because it lies within the world's sunbelt geographic area (the Global Sunbelt is the area where the most solar power stands to be harvested). By 2030, the 66 countries in the Global Sunbelt could reach an installed solar PV capacity of 1.1 TW), [19]. Using PV panels, each unutilized 100 km^2 of the western and southern desert (Al-Badiya Al-Shimaliya Wal Al-Janoubiya) has the potential to provide 30 million tons of oil equivalent (MTOE) per year. This makes Iraq a perfect place for investment in solar energy and will be a long-term solution to the electricity shortage. The average daylight is 3244 hours per year (of a doable 4383) with an average of 9 hours of daylight per day. The average solar radiation resource in Iraq provides an annual Global Horizontal Irradiation (GHI) of 2350 kWh/m^2, which might be thought of as an awfully robust resource and compares favorably to South Africa, which incorporates a GHI of 2218 kWh/m^2, however, but the Atacama Desert in Chile, that has a GHI of 3000 kWh/m^2 in the bound area and is amongst the best resources in the world) [19]. While the average efficiency of a modern solar panel is between 15 and 25%, total solar energy is estimated to be around 3.4 billion kWh per year, equating to 16% efficiency. Solar energy can be used in roughly two-thirds of Iraq's regions. In Iraq's southern and western regions, horizontal radiation is greater than 6.5–7 kWh/m, with solar radiation durations of 2800

and 3000 hours per year, respectively (see table 1). As a result, the two regions are ideal for solar power plant investment.

Table 1. Average direct normal irradiation (DNI) for different locations [19].

Location	Karbala	Najaf	Samawah	Mosul	Ramadi	Baghdad	Erbil
Average Annual Global Horizontal Irradiation (GHI) [kWh/m^2]							
	2248	2233	2226	2200	2193	2190	2171

During the 1980s, the Republic of Iraq made a formidable commitment to developing alternative energy sources for generating electricity. The renewable energy law was issued in 1982, and the first rooftop solar panels in the Middle East were installed at the Solar Energy Research Center in Jadriyah, Baghdad, in 1986. However, three decades of resulting wars and economic sanctions have drastically undermined the renewable energy plans. Any progress was stalled till 2009 when the Ministry of Electricity proclaimed a concept to put in six thousand off-grid solar-powered street lamps to remove darkness from the streets of Baghdad as a part of a bigger theme to pay up to the US $1.6 billion to add four hundred megawatts of solar and wind generation stations by 2016. The plan was ditched after the crash of international oil prices. Interest in solar power revived yet again in November 2017, once the government proclaimed an EOI for PPP to create around 700 MW of solar plants by the end of 2018, table 1.2, [19]. The international market's 75 percent drop in PV module prices has encouraged the public to install off-grid rooftop solar panels to replace private diesel generators and non-subsided district power run by private companies [19].

Table 2. Iraq's IPP renewable energy plan (2017) [19].

Province	Project	Capacity (MW)
Muthana	Sawa-1	30
Muthana	Sawa-2	50
Muthana	Kbadber	50
Najaf	Haydayriyha	100
Anbar	Ramadi	100
Anbar	Falluja	40
Anbar	Amireya Sumud	50
Anbar	Qarma	50
Babel	Iskandariya	225
Total		695

For the present work, Abu-Al-Khaseeb and Daquq Meteorological Stations have been selected for the purposes of analyzing the data obtained from them. The data includes the horizontal solar radiation rates, ambient temperature, and wind speed rates. This information is later used for the prediction of the performance of solar module fields placed in this geographical zone. At the same time, the Daquq meteorological station is located in the Daquq district, which is a district of the Kirkuk Governorate in northern Iraq, at an elevation of 150 m above sea level, with a longitude of 44.42° E and latitude of 35.16° N.

On the other hand, a monocrystalline solar module, type SHARB (NT-R0E3E-SHARP), was used as a unit of the solar plant so that its performance would be detected. The characteristics of this module are listed in table 3.

Table 3. Characteristics of monocrystalline solar module (NT-R0E3E-SHARP).

Parameter	Value
P_{mp} (W)	170
V_{oc} (V)	44.2
I_{sc} (A)	5.3
V_{mp} (V)	35
I_{mp} (A)	4.86
Module efficiency	13.10%
Fill Factor	72.60%
Power Tolerance	-5.00% ~ 10.00%
Maximum System Voltage V_{max} (V)	1000
Maximum Series Fuse Rating (A)	15
Temperature coefficient of I_{sc}	0.053 %/ºC
Temperature coefficient of V_{oc}	-0.35 %/ºC
Temperature coefficient of P_{mp}	-0.49 %/ºC
Cell Type	Monocrystalline
Cell Size(mm)	125 × 125
Number of Cells	6 × 12
Dimensions	1575.0 × 826.0 × 46.0mm
Weight	17.0Kg

3. Mathematical Remediation

Since the current work combines the real data collected from the Abu-Al-Khaseeb and Daquq metrological stations with the theoretical data computed using MATLAB programs, in order for the outputs from the PV solar module to be accurate, such as the output power and electrical conversion efficiency, the performance of this PV solar module can be expected based on these results. Therefore, depending on the mathematical equations taken from [20], which describe the open-circuit voltage V_{oc}, short circuit current I_{sc}, and output power from the PV solar module, the open-circuit voltage V_{oc} is inversely proportional to the operating cell temperature T, and the short circuit current I_{sc} is directly proportional to the incident global solar radiation G. Therefore, I_{sc} and V_{oc} can be described by the following equations. [20].

$$I_{sc}(G) = I_{sc}(STC)\ x\ G\ \left(in\ 1\ \frac{kW}{m^2}\right) \quad (1)$$

$$V_{oc}(T) = V_{oc}(STC) - 0.0023\ x\ number\ of\ cells\ x\ (T - 25) \quad (2)$$

The operating cell temperature T is calculated with wind speed v_{wind} by [20].

$$T = T_{am} + \left(\frac{0.32}{8.91+2v_{wind}}\right) G \quad (3)$$

Were T_{am}, ambient temperature. The output power P of the PV solar module can be calculated by the following equation [20].

$$P(G,T) = I_{sc}(G)V_{oc}(T) \quad (4)$$

While the conversion electrical efficiency η (%) of the PV solar module is defined as the ratio of output power P (G, T) to the incident optical power (input power (P_{in})) [21].

$$\eta(\%) = \frac{P(G,T)}{P_{in}} x100\% \quad (5)$$

Where P_{in} is given by:

$$P_{in} = AG \quad (6)$$

Where A is the area of the PV solar module.

4. Results and Discussion

The results of the metrological stations alone, without a comparison between them, may not provide the investor with confidence in the study. As a result, the most important outputs that provide evidence of the study's credibility and the investor's desire to choose the appropriate area for him to invest in the field of solar energy, namely solar fuel, output power, and electric conversion efficiency of the PV solar module installed in each station under study, were compared.

The variables measured by Abu-Al-Khaseeb and the Daquq meteorological station in this work correspond to the year 2019. The daily radiation rates incident on a horizontal surface, measured in megajoules per square meter, the daily ambient temperature, and wind speed rates are all measured.

Figure 1 indicates the monthly average variation of ambient temperature during the year. From the figure, it is seen that the rates increase towards the summer and that the ambient temperature rates recorded in Abu Al-Khaseeb station are higher than their counterparts recorded in Daquq station. The difference in temperature is obvious because the Abu Al-Khaseeb station is located in the Basra Governorate in southern Iraq, which is characterized by high humidity and high temperatures, especially in the summer, in contrast to the Kirkuk Governorate, where the Daquq station is located, which is characterized by low humidity and lower temperatures in the summer.

The maximum value of the monthly rate of ambient temperature is 45.93 ^{o}C in July, as recorded in Abu Al-Khaseeb station, while it is 41.20 ^{o}C in July, also recorded in Daquq station.

The monthly rates of wind speed at both stations are depicted in Figure 2. Although wind activity in Iraqi airspace is moderate and rarely subject to hurricanes, we can see from this Figure that wind actively in the Abu Al-Khaseeb station is higher throughout the year than in the Daquq station, with the highest value of wind speed in the Abu Al-Khaseeb station being 4.53 (m/s) in July and 2.51 (m/s) in June.

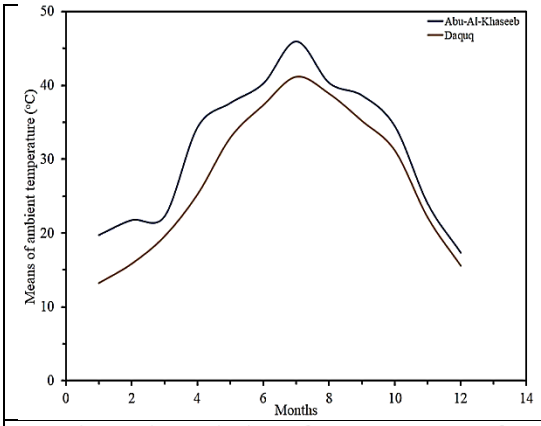

Figure 1. Variation of monthly rates of ambient temperature, along the year

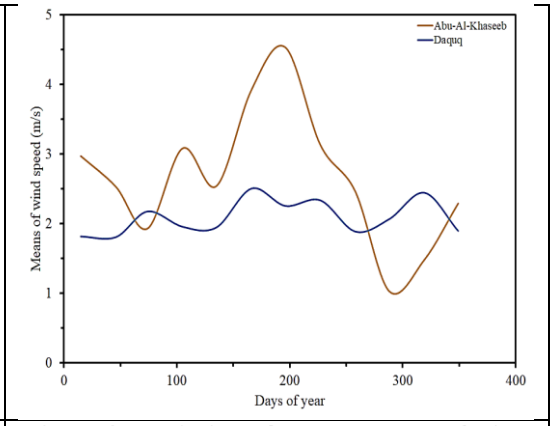

Figure 2. Variation of monthly rates of wind speed throughout the year

Monthly averages of total solar radiation falling on the horizontal surface during the year for the two stations under study are shown in Figure 3. It is clear from Figure 3 that the levels of radiation increased towards the summer and reached their maximum (6622.2 Wh/m^2/day) in July at Abu Al-Khaseeb station and (7416.67 Wh/m^2/day) in July at Daquq station.

According to the variance in the amount of incident solar radiation, there were variances in the peak sun hours, which represent the solar fuel as shown in Figure 4. These values are promising for an investment in solar energy, especially in the summer, which reached 6.62 hours in Abu-Al-Khaseeb station and 7.42 hours in Daquq station. The annual peak solar hours were 4.70 and 4.75 hours, respectively, in Abu-Al-Khaseeb and Daquq stations.

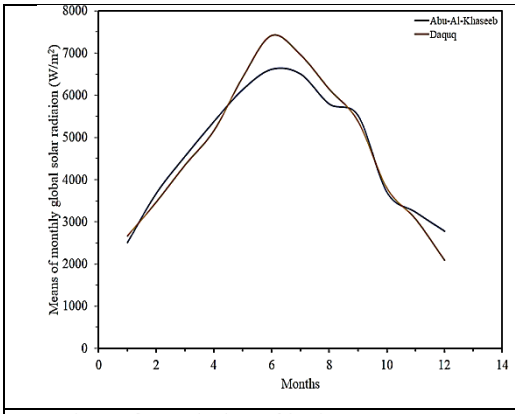

Figure 3. Variation of incident global solar radiation rates in horizontal surface along year

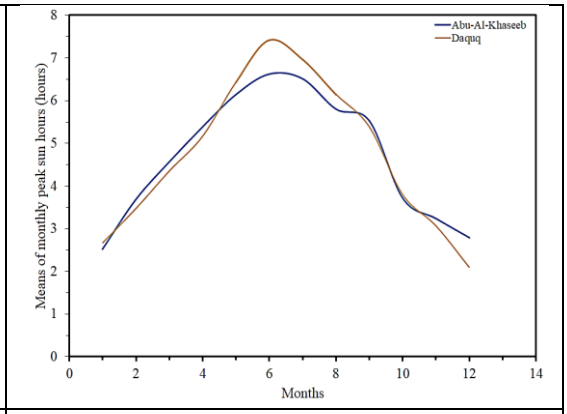

Figure 4. Variation of monthly peak sun hours along the year

Figure 5, shows the global solar radiation values were calculated in (W/m^2) at each hour of the half-month throughout the year with a tilt angle of 30^o which represents the best annual angle at which the solar module will be tilted for both stations. These values are required to predict the performance of the PV solar modules in the solar plant that will be used to generate electric energy.

For the Abu Al-Khaseeb station, the annual value of the half-monthly rates of global solar radiation falling on the PV solar module inclined at an angle of 30^o with the horizon is around 113 (kWh/m^2/year), while the Daquq station is around 114 (kWh/ m^2/ year).

Figure 6 describes the half-monthly rate of the solar cell temperature. The high half-monthly rates of solar radiation cause an increase in T, of the PV solar module and, consequently, an increase in the (I-V) curve as well as the maximum point [22, 23]. On the other hand, the high level of T, contributes to the decrease in the performance efficiency of the PV solar module. However, the output power of the PV solar module increases in parallel with the sun's radiation and the output current [24]. The maximum value of the half-monthly rates of cell temperature of the PV solar module placed in Abu-Al-Khaseeb station is 56.23 ^{o}C in July, while the maximum value of the half-monthly rates of the Daquq station is 53.97 ^{o}C in July as well.

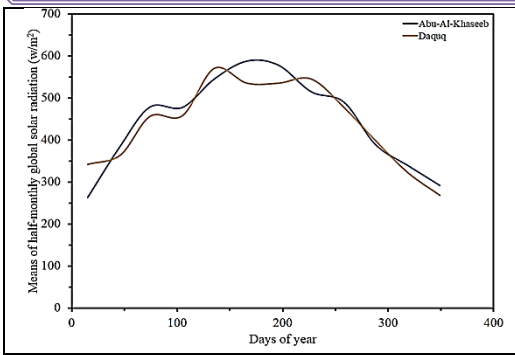

Figure 5. Variation of half-monthly rates of global solar radiation received with the tilt angle of 30° along the year

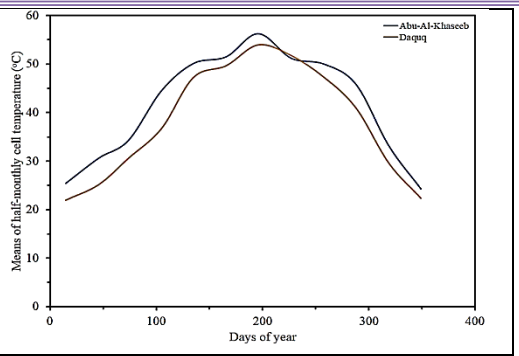

Figure 6. Variation of half-monthly rates of solar cell temperature during the year.

Although an increase in PV solar cell temperature rates leads to a decrease in the output power, the output power increases as we move towards the summer because it depends more on the amount of incident solar radiation than the cell temperature. High temperatures affect the solar cell voltage, while the value of the photocurrent increases further by increasing the level of the incident rays and is, clearly, not affected by the increase in cell temperature. This fact is demonstrated in Figure 7. Also, it is clear that the summer days are leading the rest of the year in terms of power generation output. The output power rates reach their maximum values in June while falling to their minimums in December. The maximum values of the output power of Abu-Al-Khaseeb station are 83.84 W in June and the Daquq station is 83.52 W in May.

When the sun's rays fall on the PV solar module, a portion of this radiation is converted into electrical energy is called efficiency. The half-monthly rates of PV module Figure 8 show the efficiency of the PV solar module depending on the T, of the solar panel. The high temperature of the panel leads to a gradual decrease in the performance of the PV solar module and thus reduces its efficiency in producing electrical energy. That is, the solar radiation that the PV panel receives during the middle of the day, i.e., the peak period of the sun, makes the PV solar panel ineffective [25]. It is true that the electrical energy produced by the PV solar module increases with the increase in solar radiation, but the high temperature of the PV solar module is considered a critical problem in predicting the production of electrical energy. The electric conversion efficiency of Abu-Al-Khaseeb station ranges from 10.75% in the summer to 13.04% in the winter, while Daquq station's ranges from 10.91% in the summer to 13.29% in the winter. In the winter and summer, the electrical conversion efficiency of this solar cell decreased by 1% to 2%.

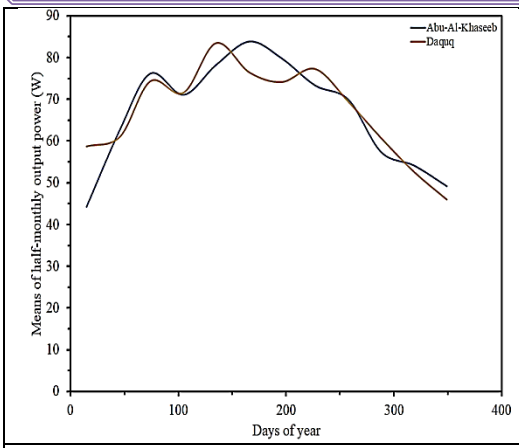

Figure 7. Variation of half-monthly rates of output power along the year

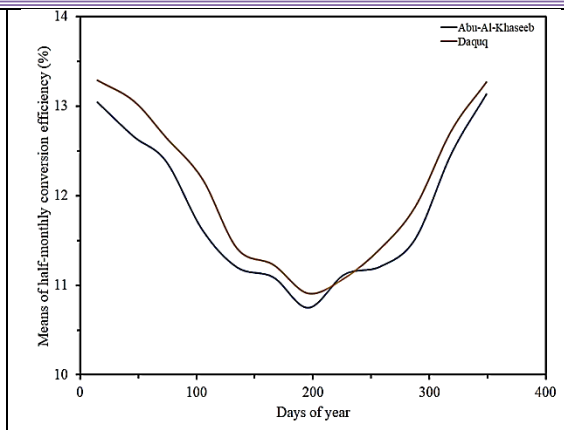

Figure 8. Variation of half-monthly rates of electrical conversion efficiency along the year

5. Conclusions

Clean energy is to fill the country's needs from the lack of electric power produced from fossil fuel stations, which causes great pollution to the living environment, and for the purpose of attracting investors in this field of energy after studying the best places in Iraq in which solar power plants can be built. So, the current work, which represents a comparative study of the performance of the same PV solar module placed in each of the two study locations in Iraq, shows that the PV solar module's performance is very similar in both locations. In other words, despite the slight climatic differences between the two locations, solar power plants can be built in both to generate solar energy.

Acknowledgment

The authors thank Mustansiriyah University for their moral support for this research, as well as the Agricultural Meteorology Center in the Ministry of Agriculture for providing us with the data from most meteorological stations in Iraq.

References

[1] H. A. Kazem, Renewable Energy in Oman: Status and Future Prospects. Renewable and Sustainable Energy Review. 15(2011) 3465–3469.
[2] A. A Dehghan, Status and potentials of renewable energies in Yazd Province, Iran. Renewable and Sustainable Energy Review. 15 (2011) 1491–1496.
[3] Y. Anagreh. A. Bataineh, M. Al-Odat, Assessment of renewable energy potential, at Aqaba in Jordan. Renewable and Sustainable Energy Review. 14 (2010) 1347–1351.
[4] M. T. Chaichan, H. A. Kazem, Thermal storage comparison for variable basement kinds of a solar chimney prototype in Baghdad - Iraq weathers. International Journal of Applied Science (IJAS), 2(2) (2011) 12-20.
[5] A. A. Kazem, M. T. Chaichan, H. A. Kazem, Dust effect on photovoltaic utilization in Iraq: Review article. Renewable and Sustainable Energy Reviews. 37 (2014) 734–749.
[6] Z. A. Darwish, H.A. Kazem, K. Sopian, M. A. Alghoul, M. T. Chaichan, Impact of some environmental variables with dust on solar photovoltaic (PV) performance: review and research status. Int J Energy Environ. 7(4) (2013) 152–9.
[7] F. M. Mohamed, A. S. Jassim, Y. H. Mahmood, M. A. K. Ahmed, Design and study of portable solar dish concentrator. Int J Recent Res Rev. 3 (2012) 52–59.

[8] B. N. Hussein, Dhia I. A. Essa, D. J. Hussein, Introducing a PV design program compatible with Iraq conditions. Energy Procedia. 36 (2013) 852–861.
[9] M. T. Chaichan, H. A. Kazem, Thermal storage comparison for variable basement kinds of a solar chimney prototype in Baghdad – Iraq weathers. Int J Appl Sci. 2(2) (2011) 12–20.
[10] A. M. A. Alasady, Solar energy the suitable energy alternative for Iraq beyond oil. In: Proceedings of the international conference on petroleum and sustainable development (IPCBEE), Singapore. 26 (2011) 11-15.
[11] S. F. A. Sharif, The project: Iraqi DESERTEC is the future second electricity supplier to Europe through Turkey. International Journal of Scientific & Engineering Research, November. 3(11) (2012,) 1-8.
[12] A. A. Mohammed, Dust storms monitoring, prediction and allocation of sources, Scientific and Technical Subcommittee on the Peaceful Uses of Outer Space, Fiftieth Session, Vienna International Center, Vienna, Austria, 2013.
[13] Y. Al-Douri, F. M. Abed, Solar energy status in Iraq: Abundant or not-Steps forward. Journal of Renewable Sustainable Energy. 8 (025905) (2016)1-19.
[14] A. A. A. Al-Khazzar, A. J. Khaled, Comparative Study of the Available Measured Global Solar Radiation in Iraq, (JREE), 4(2&3) (2017) 47-55.
[15] A. M. Humada, Salih Y. Darweesh, Khalid G. Mohammed, Mohammed Kamil, Samen F. Mohammed, Naseer K. Kasim, Tahseen Ahmad Tahseen, Omar I. Awad, Saad Mekhilef. Modeling of PV system and parameter extraction based on experimental data: Review and investigation. Solar Energy. 199 (2020) 742–760.
[16] A. M. Humada, M. Hojabri, M. B. Mohamed, M. H. Bin Sulaiman, T. H. Dakheel, A proposed method of photovoltaic solar array configuration under different partial shadow conditions. Advanced Materials Research. 983 (2014a) 307-311.
[17] A. M. Humada, F. B. Samsuri, M. Hojabria, M. B. Mohamed, M. H. Bin Sulaiman, T. H. Dakheel, Modeling of photovoltaic solar array under different levels of partial shadow conditions. In: Power Electronics and Motion Control Conference and Exposition (PEMC), 16th International. (IEEE), (2014) 461-465.
[18] A. Orioli, A. D. Gangi, A procedure to evaluate the seven parameters of the twodiode model for photovoltaic modules. Renew. Energy. 139 (2019) 582-599.
[19] H. H. Istepanian, Solar Energy in Iraq: From Outset to Offset. Iraqi Energy institute, Publication Number. IEI181018 (2018).
[20] T. Markvart, Solar Electricity, Wiey, Chichester, 2018.
[21] M. R. Rashel, Modleling Photovoltaic Panels under Variable Internal and Environmental Conditions with Non-Constant Load. Ph. D. Thesis, Universidade de Évora, Portugal. (2018) 56.
[22] G. Vokas, N. Christandonis, F. Skittide, Hybrid photovoltaic thermal systems for domestic heating and cooling-A theoretical approach. Solar Energy. 80(2006) 607-615.
[23] S. Park, Y. Miura, T. Ise, A maximum power control scheme based on multi-agent system for distributed flexible network photovoltaic system. International Conference on Renewable Energy Research and Applications (ICRERA), Nagasaki, Japan, (2012) 11-14.
[24] A. W. Leedy; K. E. Garcia, An indirect method for maximum power point tracking for photovoltaic arrays. International Conference on Renewable Energy Research and Application (ICRERA), October, Milwaukee, WI, USA. (2014) 19-22.
[25] A. R. Amelia, Y. M. Irwan, W. Z. Leow, M Irwanto, I. Safwati , M. Zhafarina, Investigation of the Effect Temperature on Photovoltaic (PV) Panel Output Performance. International Journal on Advanced Science Engendering Information Technology. 6 (5) (2016) 682-688.

Investigation the Trajectories of High Voltage Electrons in SEM Using Mirror Effect Phenomena

Tareq Hashim Abbood
Physics Depart., College of Education, Mustansiriyah University, Baghdad, Iraq.
tareqhashimabood@uomustansiriyah.edu.iq

Abstract

A group of physical and mathematical concepts was adopted to calculate the variables affecting the scattering process of electron due to the electron mirror in a Scanning Electron Microscope. These equations were based on simplified engineering mathematics to describe the scattering of the incident electron with the surface potential energy of dielectric sample under study using the matched beam ion microscope and scanning electrons. An acceleration voltage of 30 kV was used for charging the insulator to the saturation with a time of 5 minutes, and the accumulated charge was 0.3 nC, from which the surface voltage was calculated over the working distance (WD= 15 mm). In the second step, scanning voltages (Vsc= 2, 3, and 4 kV) were used, and in each of them it was found that the scattering angle (β) was inversely proportional to the incidence angle (θ) as the angle between the incident and scattered electron (2α) increased with the increase in incident angle. It was also found that the vertical height of the scattering point is inversely proportional to the incident angle of the electron.

Keywords: SEM, Electron Mirror Effect, Electron trajectory.

المستخلص:

تم اعتماد مجموعة من المفاهيم الفيزيائية والرياضية لحساب المتغيرات التي تؤثر على عملية تشتت الإلكترون بسبب مرآة الإلكترون في مجهر المسح الإلكتروني. اعتمدت هذه المعادلات على رياضيات هندسية مبسطة لوصف تشتت الإلكترون الساقط مع الطاقة الكامنة السطحية للعينة العازلة قيد الدراسة باستخدام مجهر شعاع الأيونات المتطابق ومسح الإلكترونات. تم استخدام جهد تسارع قدره 30 كيلو فولت لشحن العازل للتشبع لمدة 5 دقائق ، وكانت الشحنة المتراكمة 0.3 نانو سي، والتي تم حساب الجهد السطحي منها على مسافة العمل (WD= 15 mm). في الخطوة الثانية، تم استخدام جهد المسح (Vsc= 2, 3, 4 kV)، وفي كل منها وجد أن زاوية التشتت (β) تتناسب عكسياً مع زاوية السقوط (θ) كزاوية بين الإلكترون الساقط والمشتت (2α) يزداد مع زيادة زاوية السقوط. وجد أيضًا أن الارتفاع الرأسي لنقطة التشتت يتناسب عكسياً مع زاوية سقوط الإلكترون.

الكلمات المفتاحية: SEM، تأثير مرآة الإلكترون، مسار الإلكترون.

1. Introduction

The scanning electron microscope is one of the effective devices for photographing and analyzing a wide range of materials and showing details that may reach the limits of the nanometer using a focused electronic beam with different voltages starting from (0-30 kV).The mechanism that generates the image is the detection of products resulting from the interaction of the primary beam with specimen atoms and a large number of signals will be generated like backscattered electrons, secondary electrons, X-Rays, Auger electrons, cathodoluminescence and specimen current [Hafner 2007].

When using conductive sample, the incident beam of electrons leads to the injection of specimen with electrons quickly flowing through the metal base (on which the sample is based) to the ground, on the contrary, when using non-conductive sample, these injected electrons accumulate on the specimen surface and at a certain depth in it leads to establish a potential that increases with the time of electron irradiation until it reaches the level of saturation at relatively long times, leading to the generation of a repulsive force with the higher energy electrons (relative to the energy of the surface potential) coming towards the sample and the result will lead to a decrease in the energy of the incident electron.

But by using a low scanning energy i.e. low energy of electrons less than what of the specimen surface, the incident electron will gradually slow down by the energy of the surface potential until all of its kinetic energy turns into potential energy, and thus it will stop at the scattering point and disperses at a certain angle to the top part of evacuated chamber at a rate of kinetic energy growing from zero to the scanning voltage (E_i) that is of the electron left the exit column diaphragm, this phenomenon is called the Electronic Mirror Effect and it symbolized as EME.

In 1999, Vallayer et al. studied the electron trajectories using Rutherford scattering cross section and Gauss's approximation, in the case of a point charge and low scanning voltage, to calculate the trajectories and then connected between some variables of the image and trapped charges [Vallayer et al. 1999].

By 2010, Milani et al. discussed a basic model to calculate the inversion point of electrons of the primary beam against the dielectric surface potential with zero incident angle for several scanning potentials [Milani etal. 2010].

After three years, A theoretical study is carried out by Al-Obaidi et al. to describe a scanning electron path using low scanning potential with parabola model of Rutherford scattering [Al-Obaidi etal. 2013].

Additionally, Al-Zahy in (2015) derive an equation for the differential cross-section of reflected electron for low scanning voltages less than (1 kV) by using Electron Mirror Phenomenon [Al-zahy 2015].

This work provides important information about the phenomenon of the mirror effect in relation to the angles of incident electron during scanning process, the angles at which the electron scatters and the trajectories in which it falls on the inner parts of the upper surface of the vacuum chamber by the influence of the equipotential surface to the surface potential arising from the accumulated charge on the insulating specimen as well as distance work and the diameter of the electronically irradiated area on the dielectric.

2. Method

An insulator specimen irradiated with scanning potential 30 kV, it will be accumulated charge (Q_t) at each time on the insulator surface until reach the saturation (Q_s) at long time according to equation:

$$Q_t(t) = Q_s e^{-\frac{t}{\tau}} \dots (1)$$

Where τ is the time constant of the specimen. When the accumulated charge on insulator surface at saturation 0.3 nC [Milani etal. 2010] as a result of the incident electrons in a regular scanning pattern with an accelerating potential 30 kV within (5-minutes) scan period, then a potential energy and electric field will be generated as a result of that accumulated charge can be calculated as [Abbood 2010]:

$$eV_S(R,y) = \frac{2eQ_t}{4\pi\epsilon_0 R^2}\left(\sqrt{y^2+R^2}-y\right), E_y(R,y) = \frac{Q_t}{2\pi\epsilon_0 R^2}\left[1-\frac{y}{(y^2+R^2)^{\frac{1}{2}}}\right] \dots (2)$$

As the voltage will be a function of both the radius of the irradiated area (R) and the working distance (WD) between the chamber stage and the diaphragm exit of the incident electrons.

Now, when an electron falls vertically with a scanning voltage less than the surface potential of the dielectric sample, it will be affected by a repulsive force that reduces its energy at every point of its path toward the sample surface, and a portion of its kinetic energy turns into potential energy with the sum of its kinetic and potential energy remaining constant according to the equation:

$$eV_s = K.E. + P.E. \dots (3)$$

Until it reaches a certain point in its path, all its kinetic energy turns into potential energy, then the electron stops and scatters back (at a point called the scattering point) and begins to be affected by the surface voltage with a gradual increase in its kinetic energy and a decrease in its potential energy and collides with the walls of the vacuum chamber (upper), which leads to release the secondary and backscattered electrons, the secondary electrons are gathered through the Everhart Thornley detector to show an image of the inner walls of the microscope (instead of the usual microscope doing which is to produce an image of the specimen surface under study) in the electronic mirror effect process. At scattering point at ($eV_{SC}=eV_s$) and by utilizing equation (1), one can determine the vertical height of scattering point (r_e) by the equation:

$$r_e(Q_t, V_{SC}) = \frac{Q_t{}^2 - \lambda^2 R^2}{2Q_t\,\lambda} \ldots (4)$$

where $= 2\pi\epsilon_0 V_{SC}$.

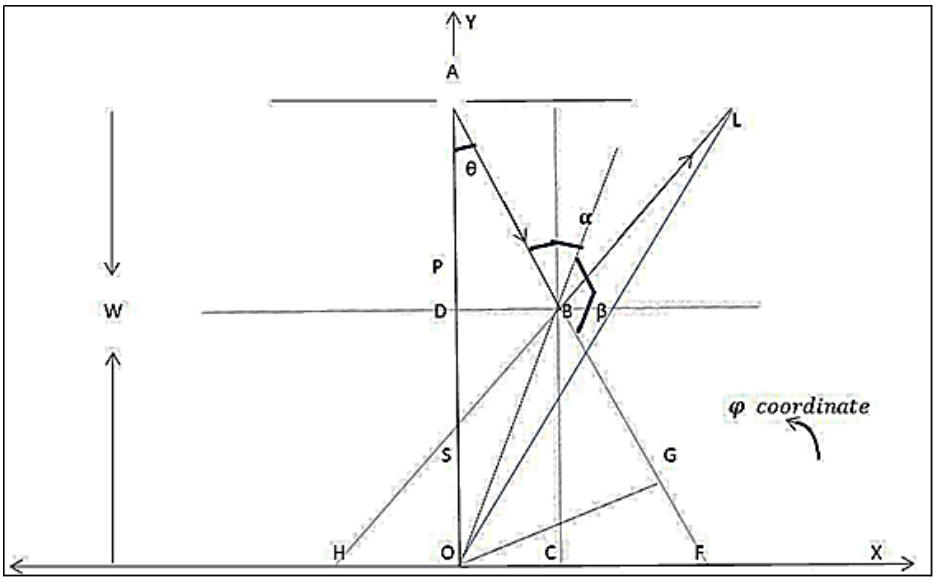

Figure (1): A schematic diagram of the incidence and scattered electrons with its angles and trajectories

As shown in figure (1), the scattering point (r_e = P) is a vertical height of reflection point at ($\theta = 0$) according to the last equation.

It is clear that the height of scattering point have decrease (towards the specimen surface) with the increasing of scanning potential V_{SC} because the increasing of scanning potential means that the electron has kinetic energy enough to move more towards the specimen surface until it will stop at a point more close to the insulator.

In fact (OP) equals the radius of equipotential surface (OB) of that scanning potential and accumulated charges density (as a form of charged disc) in the specimen which have radius (R=0.3mm) and height equal to the penetration depth (PD) of incident electron, in specimen PET with density (ρ =1.38g/cm^3), is 11.91μm according to the equation [Potts 1987]:

$$PD(\mu m) = \frac{0.1E_i^{1.5}}{\rho} \ldots (5)$$

In figure (1) the incidence angle (θ), scattering point (B), and the scattering angle (β) of an incident electron with a scanning voltage (V_{sc}) on a dielectric sample, can be recognized by

an irradiation area with radius (R=0.3 mm). As it is known, the scanning mode allows the electron to scan the irradiated area according to the spherical coordinates system (r,θ,φ) where (r) represents the path of the incident electron, (θ) the angle of incidence and (φ) the angle that is line moves to the second line, and so on. Work in this research will be limited to coordinates (r,θ), while (φ=0) that is, in the plane (x, y), and the scan will be on the width of the irradiated region from (-R to R).

According to the angle of OBG which is equal to α, so:

$$\sin(\alpha) = \frac{OG}{r_e} \ldots. (6)$$

In triangle OAG; $OG = W\ sin\theta$ … (7)

The angle ABL, CBF and OBF are equal to (2α), θ and α respectively, so OBC angle is (α- θ) and in triangle OBC;

$$OC = OB \sin(\alpha - \theta) \ldots..(8)$$

$$OF = W \tan\theta \ldots.. (9)$$

$$CF=OF-OC \ldots. (10)$$

The height of scattering point (BC) can be calculated by:

$$BC = OB\ \cos(\alpha - \theta) \ldots(11)$$

From figure (1) and equations. (6and7), the angle (**α**) can be calculated through the equation:

$$\alpha = \arcsin\frac{OG}{OB} \ldots (12)$$

Obviously, the scattering angle is obtain by the following:

$$\beta = 180 - 2\alpha$$

3. Results and discussion

Figure (2) shows the relation between the angle of incidence (θ) and the angle of scattering (β) and notes that the angle of scattering decreases with increasing the angle of incidence, i.e. the angle between the incident and scattered electrons (2**α**) increases linearly in the scanning voltage (V_{sc}=2 kV) and then moves away from the linearity in the voltages (V_{sc} = 4 and 6 kV) as a result of the increase in the repulsion force impacted on the electron approaching the sample surface as shown in Figure (3).

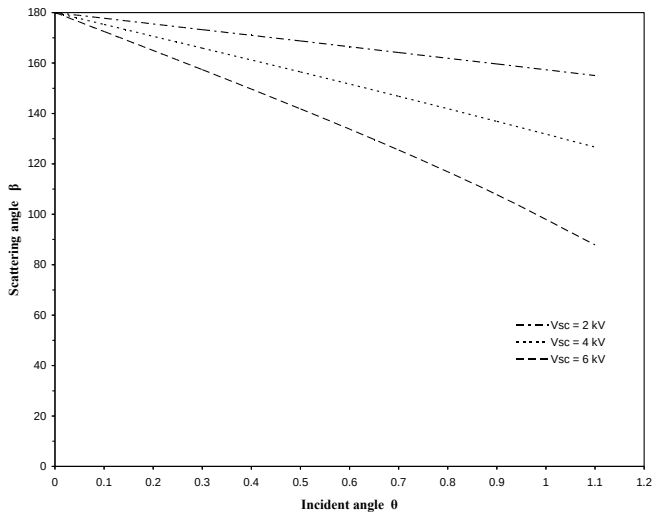

Figure (2): The relation between the incident angle (θ) and scattering angle (β).

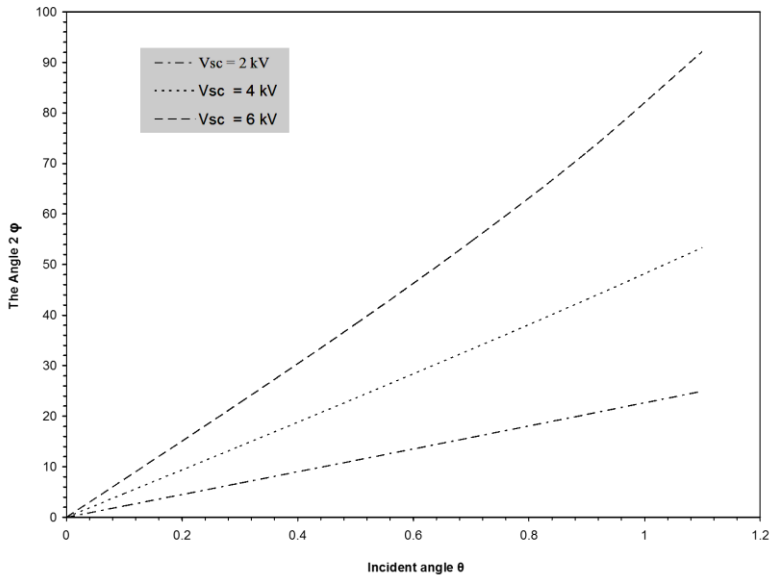

Figure (3): The relation between the incident angle (θ) and the angle (2α).

The increase in the incident angle of electron means that the path of the electron will move away from the axis (y) and rebound from the reflection point on the surface equal to the spherical voltage from the vertical height of reflection point (BC) that decreases with the increase in the angle of incidence (θ) as shown in figure (4).

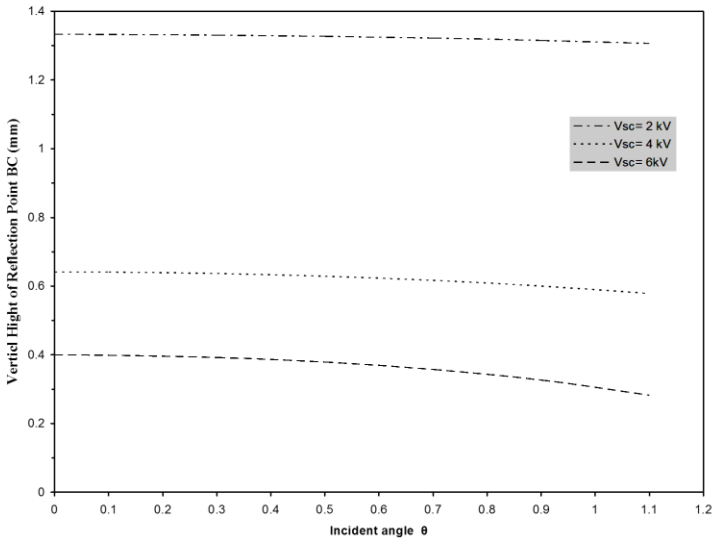

Figure (7): The relation between the impact factor (BC) and incident angle (θ).

Finally, the trajectory of electron can be drawn from knowing its starting point (O,WD), its scattering point B (OC,BC), and its collision point (of the upper surface) with the walls of the vacuum chamber (AL,WD), as shown in Figure (5).

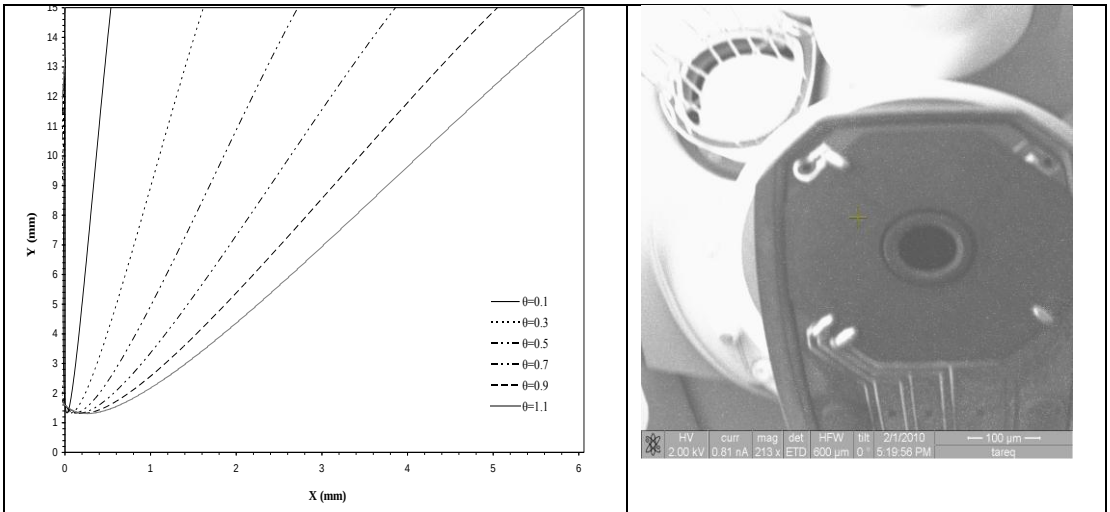

Figure (5): The trajectories of scattered electrons for V_{SC}=2 kV and different incident angles.

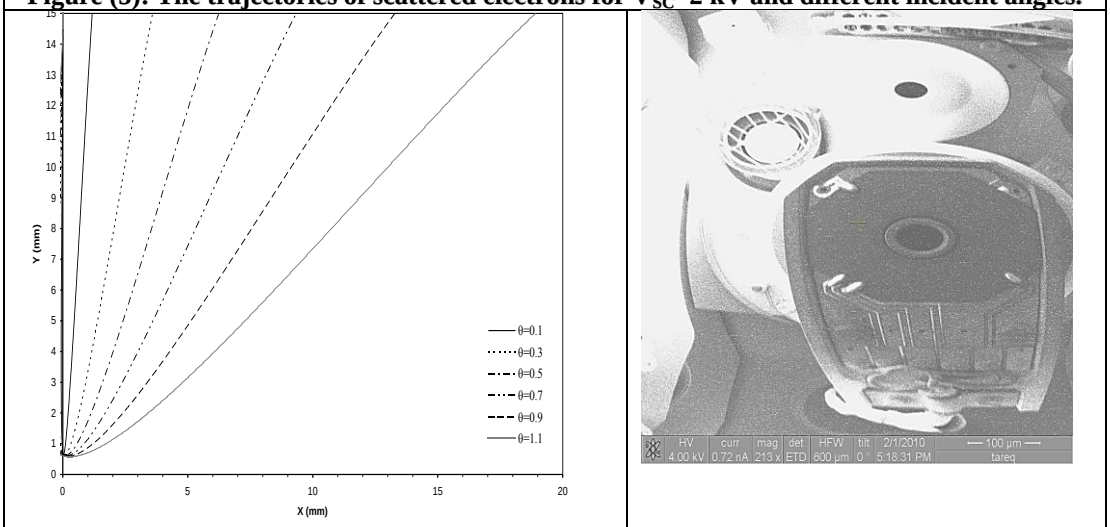

Figure (6): The trajectories of scattered electrons for V_{SC}=4 kV and different incident angles.

We notice from the figure (5) that the greatest collision distance with the upper surface is at the largest angle of incidence ($\theta=1.1^0$) and is equal to (6.0553 mm) while in the scanning voltage (4 kV) the imaged region has radius equal to (18.9061 mm) as shown in figure (6). At the scanning voltage (6 kV), it becomes clear that the area of the imaged region is large with a radius equal to (43.6254 mm) at the angle of incidence ($\theta=0.9^0$) figure (7), while the path of the electron at the angle of incidence ($\theta=1.1^0$) shows that the electron has dispersed at an angle of ($\beta= 87.84^0$) and appeared as a refracted ray and not reflected because it scattered from the last point on the circumference of the equipotential surface, and therefore, with the effect of the force towards the positive axis (x), it did not go upwards, but went to collide with the non-irradiated region of the insulating, and this is evident from the small increasing in the photographed region at the top of the vacuum chamber of device, as shown in figures (7 and 8).

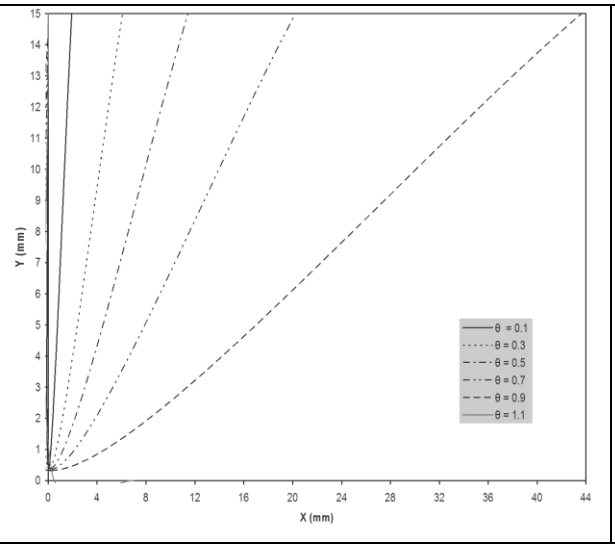

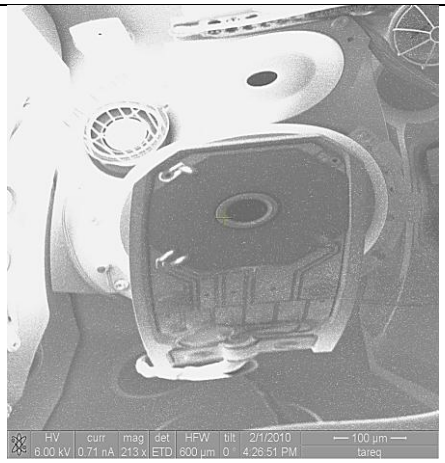

Figure (7): The trajectories of scattered electrons for V_{SC}=6 kV and different incident angles.

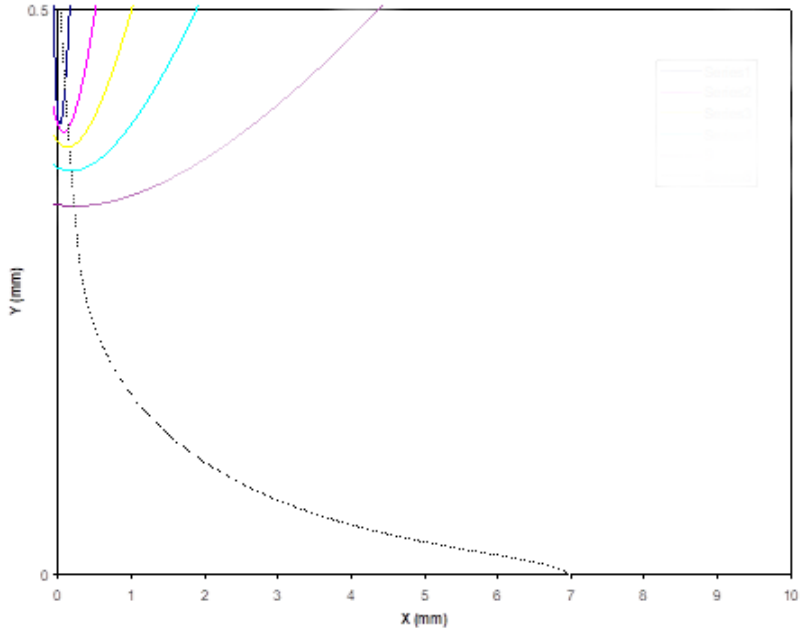

Figure (8): The trajectory of scattered electron for V_{SC}=6 kV and incident angle (θ=1.1^0).

For a specific scanning potential, the electrons scattering points at different incident angles along the scan line between + R and -R represent a line of equipotential surface, with a radius of r_e, as a result of the effect of surface potential energy (by the trapped charge 0.3 nC) on the scanning potential of electron as shown in figure (9).

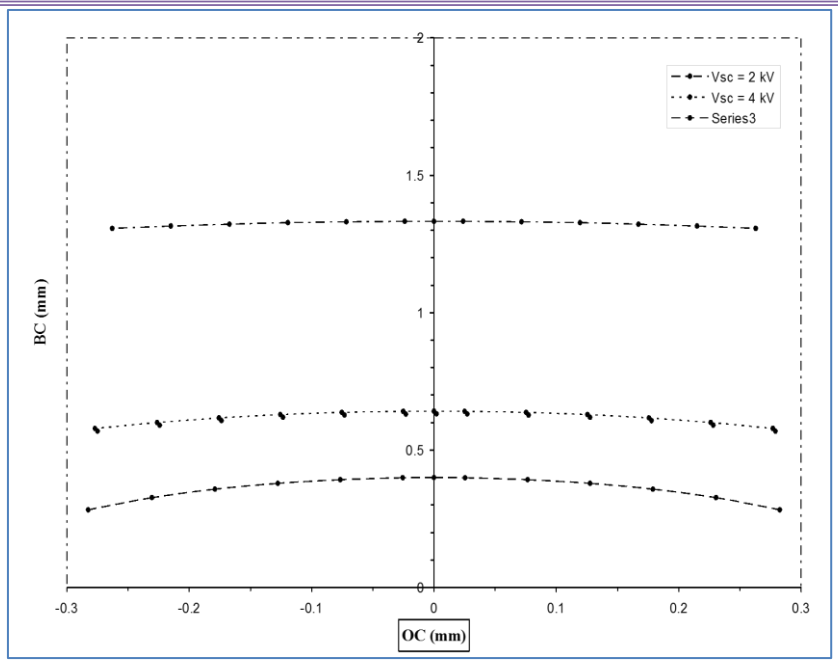

Figure (9): The equipotential surface resulting from the line connected between scattering points of electrons with different scanning potentials V_{SC}

The obtained results of this work showed that the scattering angle (β) was inversely proportional to the incidence angle (θ) as the angle between the incident and scattered electron (2α) increased with the increase in the angle of incidence. It was also found that the vertical height of the scattering point is inversely proportional to the angle of incidence of the electron.

References

- Hafner, B., (2007),"**Scanning Electron Microscopy**", Primer University of Minnesota.
- Belhaj, M., Jbara, O., Filippov, M., Rau, E., and Andrianov, M., (2001a), "**Analysis of two methods of measurement of surface potential of insulators in SEM: electron spectroscopy and X-ray spectroscopy methods**", Appl. Surf. Sci., vol. 177, pp. 58.
- Vallayer, B., Blaise, G., and Treheux, D., (1999), "**Space charge measurement in a dielectric material after irradiation with a 30 kV electron beam: Application to single-crystals oxide trapping properties**", Rev. Sci. Instr., vol. 70, No. 7, pp. 3102.
- Milani, M., Abdul-Wahab H., Abbood T., Savoia C., and Tatti F., (2010), '**Rear window: looking at charged particles hitting a charged target in a FIB/SEM**', Microscopy: Science, Technology, Applications and Education.
- Al-Obaidi H., Khaleel I., (2013), **Modelling of electron trajectories inside SEM chamber concerning mirror effect phenomenon**, vol. 11, No.21, pp.12-19.
- Al-Zahy Y., (2015), '**Differential cross section for reflected electrons measured by electron mirror method**', J. of Nanophotonic, V. 9.
- Abbood T., (2010), **Formal Invedtigation of the Mirror Effect in SEM**, PhD. Thesis: College of Education, University of Al-Mustansiriyah, Baghdad, Iraq.
- Potts, P., (1987), A Handbook of Silicate Rock Analysis, Blackie, p. 336.

Optical Characterization of SnO_2:F Thin Films Produced by Spray Pyrolysis

Salam Amir Yousif
Department of Physics, College of Education, Mustansiriyah University, Baghdad, Iraq
salammomica@uomustansiriyah.edu.iq

Abstract

Transparent conducting thin films of fluorine doped tin oxide (FTO) have been deposited successfully by simple and cost effective chemical spray pyrolysis (SP) technique onto quartz substrate at different fluorine doping (0, 5, 10, 15, 20%) at substrate temperature (450℃). The transmittance value of 50% for the undoped films is found to increase to 70% for 20% of fluorine doping (at 890 nm). The increase in the transmittance spectra of the SnO_2:F thin films due to the decreasing in the film thickness because of the growth rate is decreased with increase fluorine content in the films and, the color of the undoped tin oxide thin film is milky white that turned colorless when the doping concentration increased to (20%). The optical band gap are found to be (3.5, 3.57, 3.65, 3.7, 3.75) eV for fluorine doping concentration (0, 5, 10, 15, 20%), respectively.

المستخلص:

تم تحضير أغشية ثنائي اوكسيد القصدير المشوبة بالفلور الرقيقة بواسطة تقنية التحلل الكيميائي الحراري على قواعد من الكوارتز ولنسب تشويب مختلفة (0, 5, 10, 15, 20%) عند درجة حرارة (450℃). لقد لوحظ ان قيمة النفاذية قد ازدادت من 50% للأغشية الغير مشوبة الى 70% للأغشية المشوبة بنسبة 20% عند طول موجي (890 nm). ان الزيادة في طيف النفاذية لأغشية ثنائي أوكسيد القصدير المشوبة بالفلور ناتج من النقصان الحاصل في سمك الاغشية المحضرة وذلك لان نسبة الانماء تقل بزيادة نسبة التشويب بالفلور، كما ان لون الاغشية يتغير من اللون الابيض (الحليبي) بالنسبة للأغشية الغير المشوبة الى الشفاف عند التشويب بالفلور بنسبة 20%. ان قيم فجوة الطاقة البصرية تساوي eV (3.5, 3.57, 3.65, 3.7, 3.75) المقابلة لنسب التشويب (0, 5, 10, 15, 20%) على التوالي.

1. Introduction

Transparent conducting oxide (TCO) thin films such as zinc oxide, indium oxide, tin oxide, indium tin oxide and cadmium oxide have attracted considerable attention because of their low resistivity and high optical transmittance [1]. Due to their optical and electrical properties, TCOs are used for photovoltaic solar cells, phototransistors, liquid crystal displays, optical heaters, gas sensors, transparent electrodes and other optoelectronic devices [2, 3]. Among these TCOs, SnO_2 films are inexpensive, chemically stable in acidic and basic solutions, thermally stable in oxidizing environments at high temperatures and also mechanically strong, which are important attributes for the fabrication and operation of solar cells [4, 5]. SnO_2 has a tetragonal structure, similar to the rutile structure with the wide energy gap of E_g= 3.6 – 4.0 eV and behaves as an n-type semiconductor [6, 7]. Antimony (Sb), arsenic (As), phosphorus (P), indium (In), molybdenum (Mo), fluorine (F) and chlorine (Cl) have been selected as doping elements for SnO_2 films [8, 9]. SnO_2 thin films are produced by different techniques such as thermal evaporation, sputtering, spray pyrolysis, sol–gel and hydrothermal [10, 11]. Among these, spray pyrolysis is well suited for the preparation of doped tin oxide thin films because of its simple and inexpensive experimental arrangement, ease of adding various doping materials, reproducibility, high growth rate and mass production capability for uniform large area coatings [1, 12].

The aim of this work is to investigate the effect of Fluorine incorporation on the optical properties of SnO_2 thin films produced by (SP) technique.

2. Experimental part

Fluorine doped tin oxide (FTO) films were prepared on quartz substrate ($2.5 \times 2.5\ cm^2$) at a substrate temperature (450℃) for different fluorine doping (0, 0.05, 0.1, 0.15) by a homemade spray pyrolysis technique under ambient atmosphere. The experimental setup and other details have been reported elsewhere. The spray solution prepared from tin tetrachloride penthydrate ($SnCl_4.5H_2O$) dissolved in distilled water at ($0.1\ M$) concentration and ammonium fluoride (NH_4F) was added into the solution for fluorine doping. The deposition parameters were the same for the series of $SnO_2:F$ films. The optical measurements of the SnO_2:F thin films are calculated from the transmittance and absorbance spectrum at normal incidence over the range (300 – 900 nm), using UV-VIS spectrophotometer type (SHIMADZU) (UV-1600/1700 series).

3. Results and discussion

3.1 Transmittance (T)

The UV-visible transmittance spectra of $SnO_2:F$ thin films as a function of wavelength for different fluorine doping have been shown in Fig. 1. It is seen that the transmittance of the $SnO_2:F$ films increases with increasing fluorine doping in the films, and the average transmittance in the visible region (at 550 nm) has been found (40%, 47%, 52%, 59%, 61%) for the fluorine doping (0, 5, 10, 15, 20%) respectively. The transmittance value of 50% for the undoped films is found to increase to 70% for 20% of fluorine doping (at 890 nm). The increase in the transmittance spectra of the $SnO_2:F$ due to the decreasing in the film thickness because of the growth rate is decreased with increase fluorine content in the films and, the color of the undoped tin oxide thin film is milky white that turned colorless When the doping concentration increased to (20%), which is in a good agreement with the report [2]. The increase of transmittance of $SnO_2:F$ thin films with increasing fluorine doping concentration is caused by the decrease of surface roughness that leads to the decrease of optical scattering in the films.

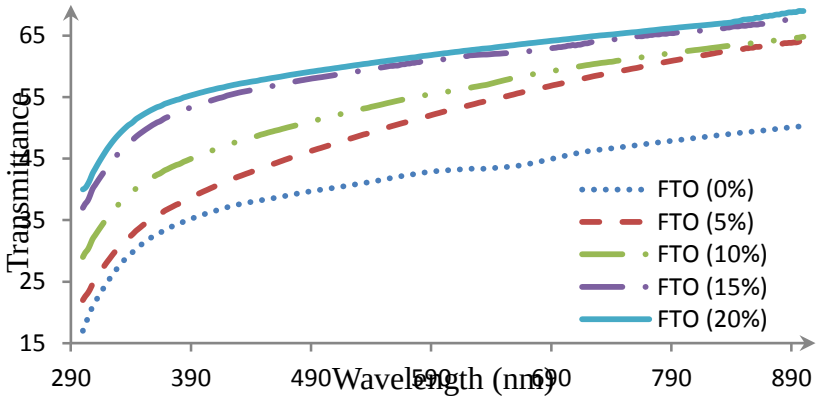

Fig. 1 Transmittance spectra of SnO_2: F thin films deposited at different fluorine doping

3.2 Absorbance (A)

The absorbance spectra of SnO_2:F thin films as a function of wavelength deposited on quartz substrate at different fluorine doping concentrations are shown in Fig. 2. In the high energy spectral range, where the film is strongly absorbent, and the absorbance of SnO_2:F films decreases with increasing fluorine content.

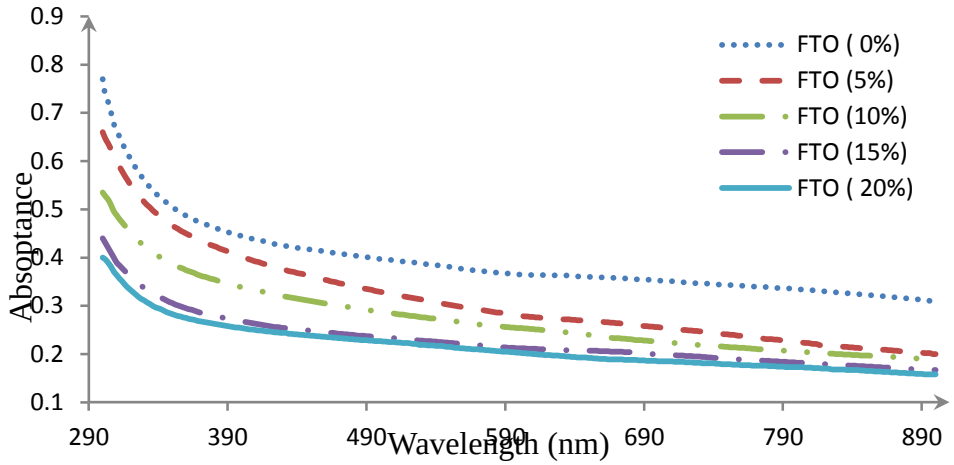

Fig. 2 Absorbance spectra of SnO_2:F thin films deposited at different fluorine doping

3.3 Reflectance (R)

Reflectance spectra of SnO2:F thin films are shown in Fig. 3. It is determined that the average reflection value of pure SnO2 films is about (20%) and this value remarkably decreases with fluorine incorporation. That decrease of reflectance results from the surface roughness, grain boundaries and morphology of the fluorine doped films, as these properties affect the intensity of the reflected light. Because of this information, it can be said that the pure SnO2 films which have highest average reflection value, lowest transmittance value and highest roughness as compared with others.

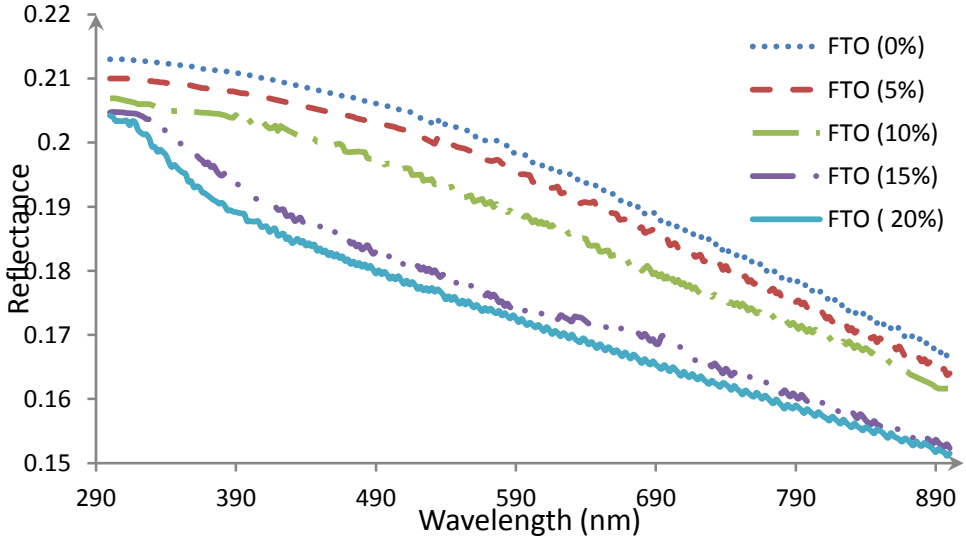

Fig. 3 Reflectance spectra of SnO_2:F thin films deposited at different fluorine doping

3.4. Absorption Coefficient (α)

The absorption coefficient (α) has been calculated from equation (1) [13, 14, 15].

$$\alpha = \frac{2.303\ A}{t} \qquad (1)$$

This coefficient depends on the incident photon energy (hυ), the energy gap of semiconductor and the type of the electronic transitions. Fig. 4 shows the change of the absorption coefficient of the SnO_2:F thin films for different fluorine doping as a function of

wavelength. It is observed that the absorption coefficient (α) decreases gradually with increasing fluorine doping concentration, the value absorption coefficient is greater than ($10^4 cm^{-1}$) which indicates the strong possibility of direct electronic transitions.

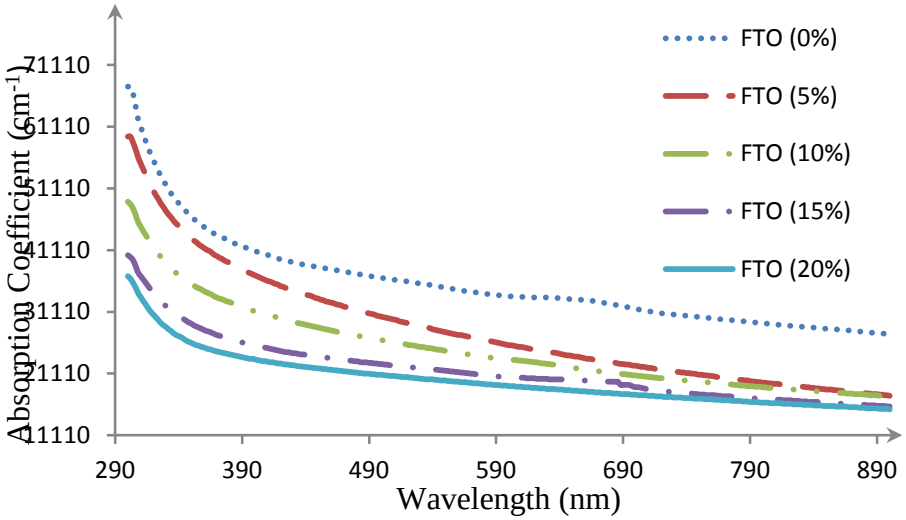

Fig. 4 Absorbance Coefficient of SnO_2:F thin film deposited at different fluorine doping

3.5 Absorption Index (Extinction coefficient) (K)

The extinction coefficient (K_o) is calculated by equation (2) [13, 14, 15].

$$K = \frac{\alpha\lambda}{4\pi} \qquad (2)$$

Fig. 5 shows the extinction coefficient versus wavelength plotted for different fluorine doping concentration. This behavior agrees with the behavior of absorption coefficient which has a direct relation with (K_o) as in equation (2). The extinction coefficient decreases with increasing fluorine doping.

3.6. Optical Conductivity ($\sigma_{optical}$)

The optical conductivity of SnO_2:F thin films prepared at different fluorine doping concentration (0 - 20) % has been calculated using equation (3) [16]:

$$\sigma_{optical} = \frac{\alpha n C}{4\pi} \qquad (3)$$

Fig. 6 shows the optical conductivity of SnO_2:F thin films as a function of wavelength for different fluorine doping. It is observed that the optical conductivity decreases with increasing fluorine doping concentrate in the films and the optical conductivity ($\sigma_{optical}$) depends directly on the absorption coefficient as shown in equation (3). We can see that the optical conductivity increases with increasing the energy; this suggests that the increase in optical conductivity is due to electron exited by photon energy which leads to the increase in the concentration of charge carriers.

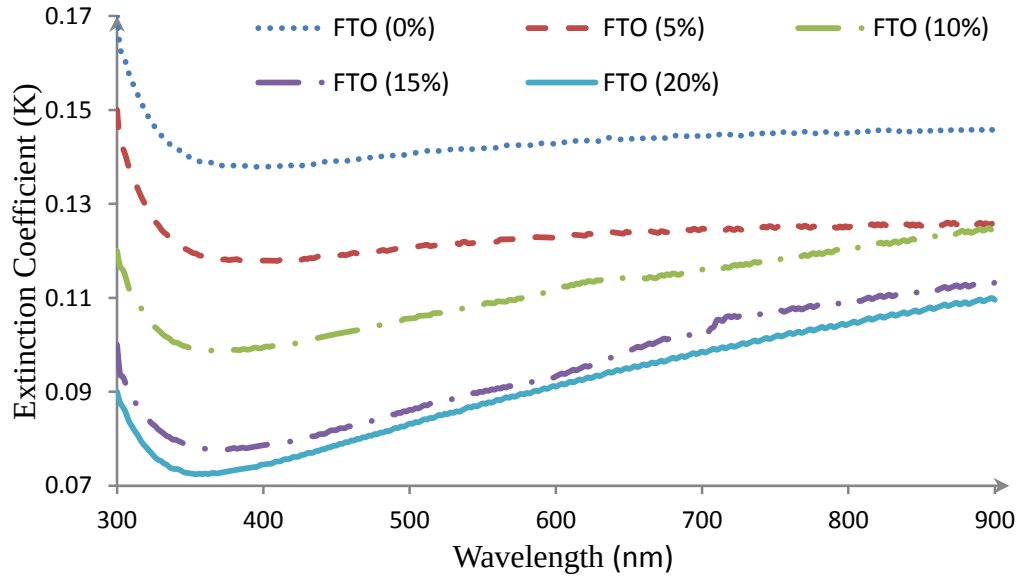

Fig. 5 Extinction coefficient of SnO_2:F thin films deposited at different fluorine doping

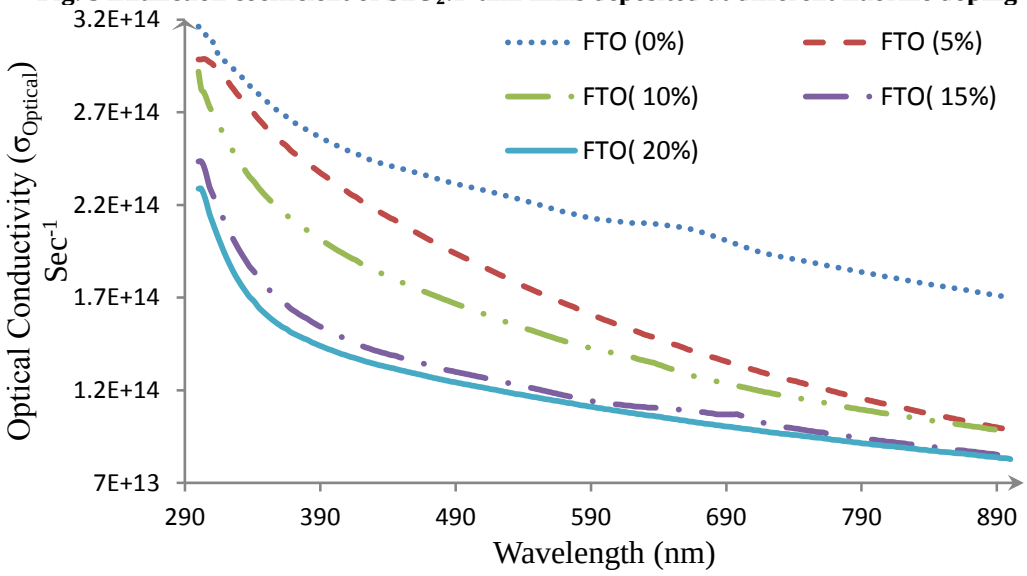

Fig. 6 Optical Conductivity of SnO_2:F thin films deposited at different fluorine doping

3.7 Refractive Index (n)

The refractive index (n) of SnO2:F thin films for different fluorine doping are determined from equation (4) [17] as shown in Fig. 7.

$$n = \left[\left(\frac{4R}{(R-1)^2}\right) - K^2\right]^{1/2} - \frac{R+1}{R-1} \qquad (4)$$

All films show similar behavior in refractive index. There is a little decrease in refractive index value with increasing fluorine doping concentration. It is concluded that the reflection index highly depend on the production technique, surface roughness, grain boundaries and morphologies of the produced films, and these properties are changed with Fluorine doping concentration.

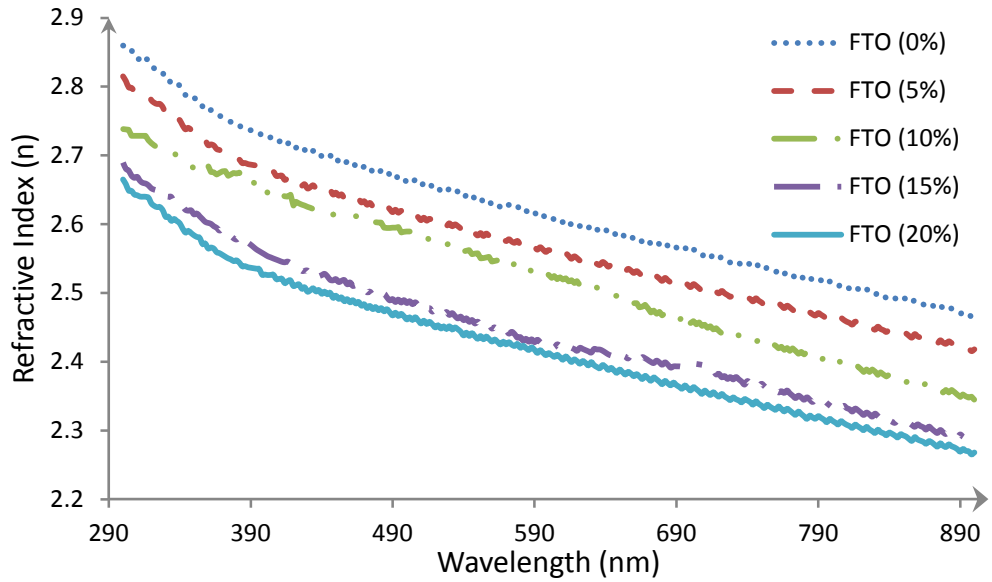

Fig. 7 Refractive index of SnO_2:F thin films for different fluorine doping

3.8 Real and Imaginary Part of Dielectric Constant (ε_1), (ε_2)

An absorbing medium is characterized by a complex dielectric constant. The real and imaginary part of dielectric constant of SnO_2:F thin films prepared at different fluorine doped (0, 0.05, 0.1, 0.15, 0.2) by spray pyrolysis technique on quartz substrate at substrate temperature (450°C) have been calculated using equations (5), (6) [18].

$$\varepsilon_1 = n^2 - K^2 \quad (5), \qquad \varepsilon_2 = 2nK \quad (6)$$

The real and imaginary parts of dielectric constant as a function of wavelength of SnO_2:F thin films deposited at different fluorine doping are shown in Figs. 8, 9 respectively. It is found that the real and imaginary parts of dielectric constant of SnO_2:F thin films decreases with increase fluorine doping concentration. The real parts of dielectric constant of SnO_2:F thin films decreases with increasing wavelength while the imaginary part of dielectric constant increases with increasing wavelength in the visible region spectra.

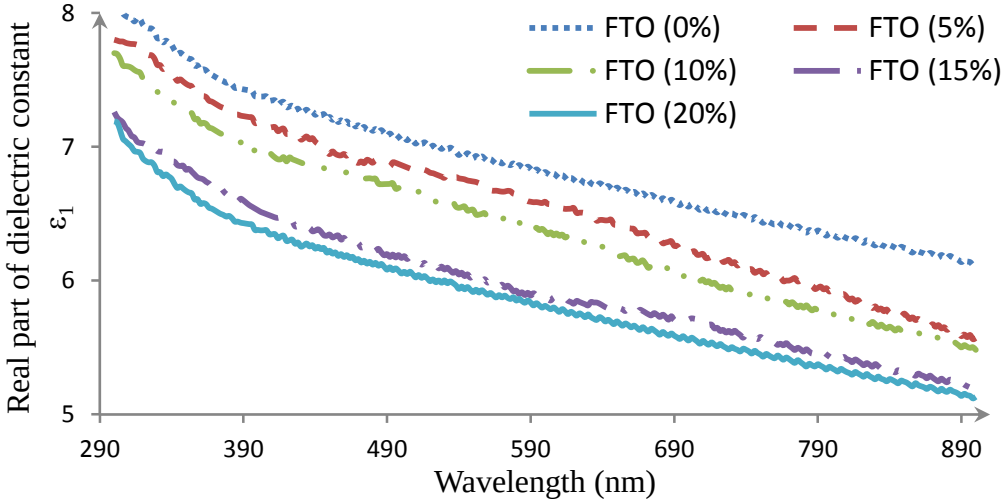

Fig. 8 Real part of dielectric constant of SnO_2:F thin films for different fluorine doping

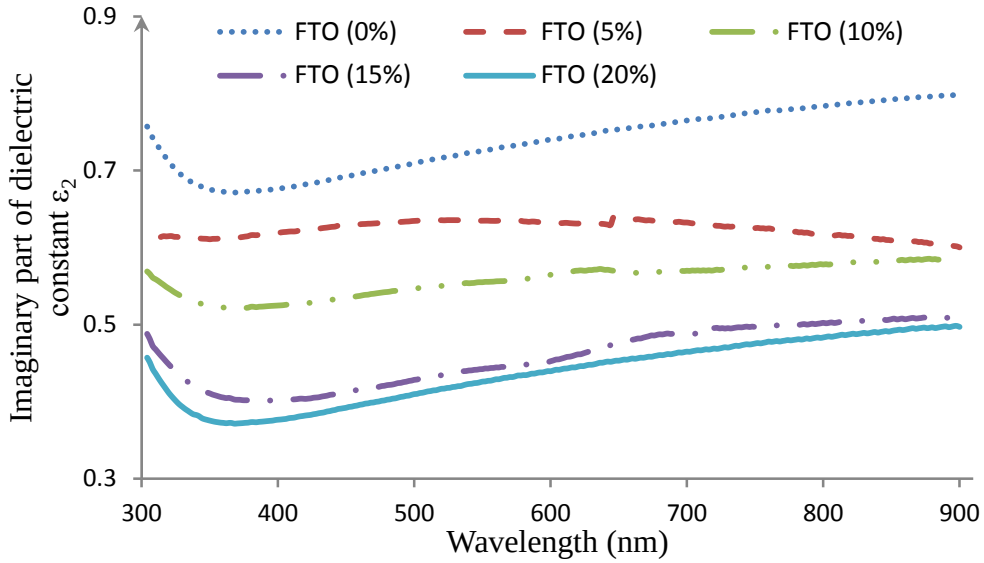

Fig. 9 imaginary part of dielectric constant of SnO_2:F thin films at different fluorine doping

3.9 Optical Band Gap (E_g)

The optical band gap (E_g) of the SnO_2: F thin films is calculated from the allowed direct transition given by $\alpha h\gamma = A(h\gamma - E_g)^X$ where (hγ) is the photon energy, (E_g) the bandgap and (A) the edge parameter. The value of (x) is (1/2) for direct allowed transitions and (2) for indirect allowed transition. The films prepared in the present study have direct allowed transitions. The optical band gap is determined by extrapolating of the linear part of the curve $(\alpha h\gamma)^2$ which intercepts the energy axis, E_g are found to be (3.5, 3.57, 3.65, 3.7, 3.75) eV for fluorine doping concentration (0, 5%, 10%, 15%, 20%), respectively. As shown in Fig. 10, the optical band gap is increase with increasing fluorine doping concentration in the films. This result is in a good agreement with the report [2].

3.10 Urbach Energies (E_U)

It is well-known fact that semiconductors represent band tails due to the deformation and high carrier concentration. Defects in structure lead to local electric fields that affect the band tails, and band tiling is a result of impurity, disorder or any other defects. The absorption coefficient (α) in the low Energy range follows the well-known exponential low, that is the Urbach tail expressed by $\alpha(v) = \alpha_0 \exp(\frac{hv}{E_u})$ where (α_o) is constant and E_U denotes an energy which is constant for weakly dependent on temperature and is often interpreted as the width of the tail of localized states in the bandgap [19, 20, 21]. E_U values are estimated from the slope of the linear relationship (lnα) against (hγ) using above equation.

Fig. 11 shows Urbach plots of the SnO_2:F thin films. The values of E_U obtained from the inverse of the slope of (lnα) versus (hγ) are given in Table 1. Urbach energy of SnO_2:F thin films increases with increasing fluorine doping concentration in the films.

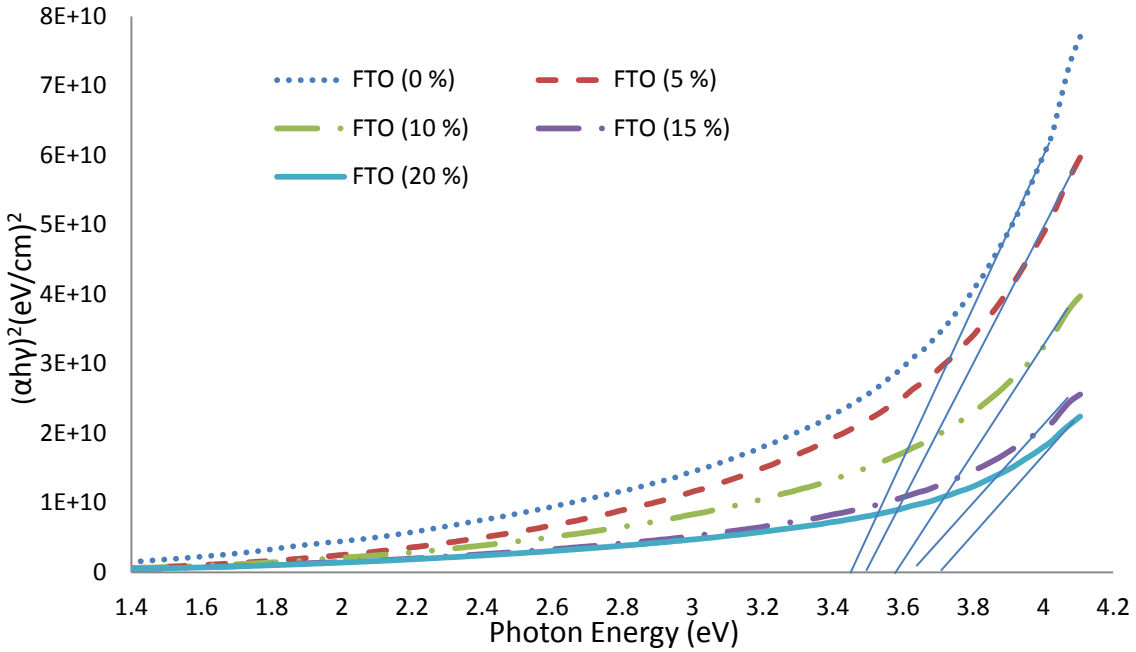

Fig. 10 Optical band gap of SnO_2: F thin films deposited at different fluorine doping

Table 1 Optical properties of SnO_2 :F thin films

Doping %	(E_U) (meV)	(E_g) (eV)	Transmittance (at 550 nm) %
0	360	3.5	40
5	342	3.57	47
10	278	3.65	52
15	231	3.7	59
20	199	3.75	61

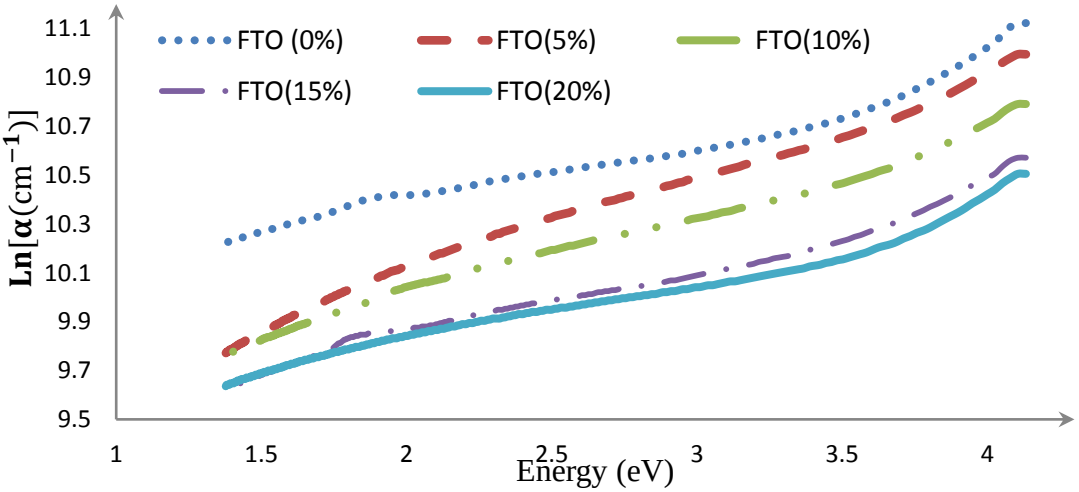

Fig 11 Urbach plots of SnO_2: F thin films for different fluorine doping

4. Conclusions

Fluorine doped tin oxide (FTO) films were successfully prepared on quartz substrate at a substrate temperature equal to 450℃ by a homemade spray pyrolysis technique. The average transmittance in the visible region (at 550 nm) has been found (40, 47, 52, 59, 61%) for the fluorine doping (0, 5, 10, 15, 20%) respectively. The increase in the transmittance spectra of the SnO_2: F due to the decreasing in the film thickness because of the growth rate is decreased with increase fluorine content in the films and, the color of the undoped tin oxide thin film is milky white that turned colorless When the doping concentration increased to (20%). The optical band gap is increase with increasing fluorine doping concentration in the films and, Urbach energy of SnO_2:F thin films decreases with increasing fluorine doping concentration in the films.

References

[1] E. Elangovan, K. Ramamurthi, Appl. Surf. Sci. 249 (2005) 183.
[2] F. Atay, M. Demir, S. Kose, V. Bilgin, I. Akyuz, J. Optoelectron. Adv. M. 9 (7) (2007) 2217.
[3] B. Thangaraju, Thin Solid Films 402 (2002) 71.
[4] H. Kim, R.C.Y. Auyeung, A. Pique, Thin Solid Films 516 (2008) 5052.
[5] Houng-LeiMa, Xiao-TaoHao, J. Ma, Ying-Ge Yang, J. Huang, De-Heng Zhang, Xian-Gang Xu, Appl. Surf. Sci. 191 (2002) 313.
[6] A.V. Moholkar, S.M. Pawar, K.Y. Rajpure, C.H. Bhosale, Mater. Lett. 61 (2007) 3030.
[7] Sung-Sik Chang, M.S. Jo, Ceram. Int. 33 (2007) 511.
[8] H. Kim, A. Pique, Appl. Phys. Lett. 84 (2004) 218.
[9] B. J. Lokhande, D. Uplane, Appl. Surf. Sci. 167 (2000) 243.
[10] D. R. Acosta, E.P. Zironi, E. Montoya, W. Estrada, Thin Solid Films 288 (1996) 1.
[11] H. Cachet, J. Bruneaux, G. Folcher, C. Levy-Clement, C. Vard, M. Neumann-Spallart, Sol. Energ. Mat. Sol. C. 46 (1997) 101.
[12] I. Taniguchi, D. Song, M. Wakihara, J. Power Sources 109 (2002) 333.
[13] B. L. Sharma, R. K. Purohit, 'Semiconductor Hetrojunction, 'Pergomon Press, New York (1974).
[14] L. K. Chopra, "Thin film phenomena,"Mc Graw.Hill Book Company (1969).
[15] Salam Amir Yousif, Abdulla Ahmad Rasheed, Nadir Fadhil Habubi. "Fondazione Giorgio Ronchi", Thin Film N. 4, (2011).
[16] Abakaliki, Nigeria. The Pacific Journal of Science and Technology, Volume 7, (2006) Number 1.
[17] J. Parkes, R. D. Tomlinson, and M. J. Hamphire, "J. Solid State Electronic", 16, (1973) 773.
[18] M. Balkanski and R. F. Wollis,"Semiconductor physics and application", Oxford University press (2000).
[19] F. Atay, V. Bilgin, I. Akyuz, E. Ketenci, S. Kose, Optical Characterization of SnO_2:F films by spectroscopic ellipsometry" (2010).
[20] S. Bandyopadhyay, G. K. Paul, S. K. Sen, Sol. Energ. Mat. Sol. C 71 (2002) 103.
[21] Y. Natsume, H. Sakata, Y. Natsume, H. Sakata, Thin Solid Films 372 (2000) 30.

Novel Relation between the Bulge Luminosity and Spiral Arm Pitch Angles

Wasmaa A. Jabbar[1], Ismaeel A. Al-Baidhany[1*], Ashwaq Ali Ismail[2]
[1]Physics Depart., College of Education, Mustansiriyah University, Baghdad, Iraq
[2] Educational Rusafa Directorate-1
[*]Correspondence: ismaeel_2000@uomustansiriyah.edu.iq

Abstract

In this work, a novel relation between the bulge luminosity (Lbulge), and spiral arm pitch angles (P) has been found. We measured the spiral arm pitch angles of a sample of 40 spiral galaxies by using a 2D Fast Fourier Transform decomposition technique (2DFFT) on Spitzer/IRAC 3.6-μm images. We selected a sample of nearly face-on spiral galaxies and used IRAF's ELLIPSE routine to determine the ellipticity and major-axis position angle in order to deproject the images to face-on, and apply a 2DFFT, we determined the spiral arm pitch angles.

The measurements of the bulge luminosity are based on a 2-dimensional (bulge-bar-disk) decomposition program by using Spitzer/IRAC 3.6 μm images. The bulge luminosity was determined for a sample of 40 spiral galaxies by applying the two-dimensional multicomponent decomposition method.

Keywords: spiral galaxies, pitch angle, bulge luminosity, classical bulges.

المستخلص:

في هذا العمل، تم العثور على علاقة جديدة بين لمعان الانتفاخ (Lbulge) وزوايا ميل الذراع الحلزونية (P). تم قياس زوايا ميل الذراع الحلزونية لعينة من 40 مجرة حلزونية باستخدام تقنية تحلل تحويل فورييه السريع ثنائية الأبعاد DFFT(2) على صور Spitzer/IRAC 3.6 ميكرومتر. تم اختيار عينة من المجرات اللولبية شبه المواجهة للوجه واستخدمنا روتين ELLIPSE الخاص بـ IRAF لتحديد زاوية الإهليلجيه وزاوية موضع المحور الرئيسي من أجل إزالة الصور إلى الوجه، وتطبيق DFFT 2، وحددنا زوايا ميل الذراع الحلزونية. تعتمد قياسات لمعان الانتفاخ على برنامج تحلل ثنائي الأبعاد (انتفاخ - شريط - قرص) باستخدام صور Spitzer / IRAC 3.6 ميكرومتر. تم تحديد لمعان الانتفاخ لعينة من 40 مجرة حلزونية من خلال تطبيق طريقة التحلل ثنائي الأبعاد متعدد المكونات.

الكلمات المفتاحية: المجرات الحلزونية، زاوية الملعب، لمعان الانتفاخ، الانتفاخات الكلاسيكية.

Introduction

A black hole is a region of space-time where gravity is so strong that nothing, not even light, can escape from it (Wald 1984).

Black holes can be divided into three types: supermassive black holes (SMBHs), intermediate masses black holes (IMBHs), and stellar masses black holes, (Gebhardt & Rich 2005). The normal black holes are thought to be the endpoint of stellar evolution for the most massive stars (Valeri & Igor 1998). Supermassive black holes are joint at the middle of all or most of galaxies (Mogorrian et al., 1998; Ferrarese & Merritt, 2000) Supermassive black holes are joint at the middle of all or most of galaxies, where observed that with the resolution of the Hubble Space Telescope (HST) with its high sensitivities to observe the centers of spiral galaxies. Also, the central masses of spiral galaxies are in the range of thousands to billions of the masses of our sun (Kormendy & Richstone 1995; Richstone et al. 1998; Kormendy & Gebhardt 2001).

Since the last decades, the researches of galaxies of galaxies have led to the detection that there are many tight relationships locally between the SMBHs masses and the global features of the components of the hosts of spiral galaxies. This suggests an interesting join between galaxy formation and SMBH growth (Yuexing 2007). As a result, astronomers

think that the energy emitted by growing SMBHs play significant role in shaping the characteristics of the host's structure of galaxies (Benson 2010; Fabian 2012).

There is growing guide which points out that relationships between the mass of the SMBH and almost or all the possible parameters of the host galaxy bulges. This suggests that SMBHs play an important role in galaxy formation. Most galaxy bulges contain a central SMBH whose mass strongly correlates with stellar velocity dispersion (σ*) within the effective radius (r_e, M_{BH}-σ*); (Ferrarese & Merritt 2000; Gebhardt et al. 2000a; Tremaine et al. 2002) with the bulge luminosity or spheroid luminosity of the galaxy (L_{bul}, M-L_{bul}; Kormendy & Richstone 1995; Magorrian et al. 1998; Marconi & Hunt 2003- hereafter, MH03; Häring & Rix 2004; Gültekin et al. 2009), with the bulge mass (M_{bul}) (Magorrian et al. 1998, MH03, Häring & Rix 2004, hereafter HR04), and circular velocity (Ferrarese 2002), with the galaxy light concentration (Graham et al. 2001), the dark matter halo (Ferrarese 2002), with the effective radius (Marconi & Hunt 2003), the Sersic index (Graham & Driver 2001, 2007), with the gravitational binding energy and gravitational potential (Aller & Richstone 2007), combination of bulge velocity dispersion, effective radius and/or intensity (Aller & Richstone 2007), with the radio core length (Cao & Jiang 2002), and the inner core radius (Lauer et al. 2007).

As mentioned above, all scaling laws have led previous authors to the conclusion that SMBH, growth and bulge formation regulate each other (Ho 2004; Benedetto et al. 2013). That means that mass of the SMBH is somehow tied to the structural parameters of the rest of the galaxy.

In this work, using more sophisticated techniques of measuring the bulge luminosity such as two-dimensional image decompositions (e.g., McLure & Dunlop 2001; Wandel 2002, Hüring & Rix 2004, Hu 2009, Sani 2011), produces a new tighter correlation between spiral arm pitch angles and the bulge luminosities of their host galaxies. The structure of this work is as follows: in Section 2, I briefly describe the sample. Section 3 is an analysis and discussion of the results. The conclusions are given in Section 4.

Sample

In this work, a sample of 40 Spitzer/IRAS (3.6μm) spiral galaxies were selected (see Table 1) The bulge luminosity estimates in this work are based on a two-dimensional (bulge - bar - disk) decomposition program which more accurately models the Spitzer/IRAC 3.6 μm images (Laurikainen et al. 2005).

The sample consisted of Hubble types ranging from Sa to Sc for which it is possible to measure pitch angle for each galaxy.

For this study, we measured the spiral arm pitch angles (P) of a sample of nearly face-on spiral galaxies by first using IRAF to determine the ellipticity and major-axis position angle in order to deproject the galaxy images to face-on by assuming that spiral galaxy disks are essentially circular. Then a two-dimensional Fast Fourier Transform (2DFFT) was applied to the deprojected images in order to measure the spiral arm pitch angles (Davis et al. 2012 & Treuthardt et al. 2012). This method removes a great deal of the uncertainty present in the measurement of the pitch angles of spiral galaxies (Davis et al. 2012).

We obtained spiral arm pitch angles of 18 spiral galaxies from the literature that were derived using B and K band images (Seigar et al. 2006, Davis et al. 2012). Spiral arm pitch angle has been shown to be independent of the wavelength at which it is measured (Seigar et al. 2006a); so, a different band of images were used to determine P for our sample of spiral galaxies. The remaining 22 spiral arm pitch angles were measured by applying a

two-dimensional fast Fourier transformation (Schröder et al. 1994) to Spitzer/IRAC 3.6μm images, assuming logarithmic spirals.
In this study, a consistent sample of 40 spiral galaxies are considered, which consisted of 14 non-barred galaxies and 26 barred galaxies, 17 AGN-host galaxies and 23 non-AGN galaxies, and 16 galaxies with classical bulges and 24 galaxies with pseudobulges.

Bulge Luminosity

In this section we present a mid-infrared study of the scaling relations between SMBH masses and the structural parameters of the host spheroids in the galaxies that are represented by bulge luminosity (L_{bul}), based on two-dimensional disk-bulge-bar decompositions of Spitzer/IRAC 3.6 μm images of 40 galaxies with M_{BH}.
Although, there are problems in determining the bulge luminosity of spiral galaxies, as a result of the difficulty in getting the values precise for bulge–disk decomposition, we used 2D bulge-disk decompositions of Spitzer/IRAC 3.6 μm images of 40 galaxies, where there is a minimum in the bright foreground from interplanetary dust. In addition, we used SExtractor (Bertin & Arnouts 1996) to mask out the pixels from foreground stars or bright neighbors, background galaxies, and possible irregularly shaped regions such as dust lanes across the galaxy. In this work, we preferred to avoid compilations of L_{bul} values from various authors using different methods, as these involve a range of morphologies different from spiral galaxies in the M_{BH} - L_{bulge} relation.
The interesting thing about this study is that the bulge luminosity is based on a large number of pseudobulges, exceeding the number of pseudobulges used in most research (i.e. 5 in Hu 2009 or 9 in Sani 2011). The poor statistics of pseudobulges in other studies prevent reaching a firm conclusion about the nature of their relation with each component of the galaxy. This means that the sample in this work is one of the largest samples used thus far to study M_{BH}-host galaxy scaling relations compared with previous works.
Here we studied the relations between bulge luminosity (L_{bul}), and spiral arm pitch angle (P) listed in Table (1).

Measurement of the bulge luminosity (L_{bul})

The measurement of the bulge luminosity is based on a two-dimensional (bulge- bar-disk) decomposition program to model Spitzer/IRAC 3.6 μm images (Laurikainen 2005). The bulge luminosity was determined for a sample of 40 spiral galaxies by applying the two-dimensional multicomponent decomposition method. In this method, an exponential function was used to describe the disc:

$$I_d(r) = I_{od} \exp[-(r/hr)]$$

where I_{od} is the central surface density of the disc, hr is the radial scalength of the disc, and r is disc radius. The bulge is described by a Sersic function:

where I_{ob} is the central surface density of the bulge, hb is the scale parameter of the bulge, and β=1/n with n=sérsic index. The half-light radius (effective radius), r_e, of the bulge was obtained by converting h_b:

$$r_e = (b_n)^n h_b$$

where the value of b_n is a proportionality constant defined such that $\Gamma(2n) = 2\gamma(2n,b_n)$. Γ and γ are the complete and incomplete gamma functions, respectively. We use the approximation $b_n \approx 2.17n_b - 0.355$ (David 2010), where n_b is the bulge Sersic index.
The bars and ovals are estimated using a Ferrers or a Sersic function.

where I_{obar} is the central surface brightness of the bar, a_{bar} is the bar major axis, and nbar is the exponent of the bar model defining the shape of the bar radial profile.
The orientation parameters were estimated using Spitzer/IRAC 3.6 μm images of 40 galaxies with M_{BH} estimates. These images were used to measure the minor-to-major axis ratios (q = b/a), effective radii, the radial profiles of the isophotal major-axis position angles (φ) and the estimated inclinations of the disk using the mean values in the outer parts of the disks (Laurikainen 2005).
First, foreground stars were removed and all point sources from the Spitzer 3.6 μm images were masked out by using SExtractor (Bertin & Arnouts 1996), next, the surface brightness profiles were derived using the ELLIPSE routine in IRAF[1] (Jedrzejewski 1987, Laurikainen 2005). To change surface brightness units to mag arcsec^{-2}, the following formula was used:

Where S3.6μm is the flux value of the 3.6 μm band in units of MJy sr−1, ZP3.6μm is the IRAC zero magnitude flux density in Jy and is 280.9 (Reach et al. 2005).
Apparent magnitude was converted to absolute magnitude using luminosity distance and absorption in the galaxies according to the NED[2] database.

Measuring spiral arm pitch angle

Previous studies described logarithmic spirals in polar coordinates (Lin & Shu 1964; Kennicutt 1981; Elmegreen & Elmegreen 2004; Seigar & James 1998a, b, 2002; Seigar et al. 2006; Vallée 2002). This is a special kind of spiral curve that describes the arm in disk galaxies:

$$r = r_0 e^{\theta \tan(\varphi)}$$

where r is radius, θ is central angle, r_0 is initial radius when θ = 0, and pitch angle is $-90 \leq \Phi \leq 90$.
Because the spiral arm pitch angle has been shown to be independent of the wavelength at which it is measured, multi-band images were used to determine it for our sample of spiral galaxies (Seigar et al. 2006a).
Spiral arm pitch angles were measured using a two-dimensional fast Fourier transform (2DFFT) decomposition with logarithmic spirals of Spitzer/IRAC 3.6 μm images of 63 galaxies, with inclinations of $30^o \leq i \leq 60^o$. The 2DFFT program analyzes images of spiral galaxies and categorizes their pitch angles and number of arms. The two-dimensional fast Fourier transform decomposition program is fully described by I. Puerari in Schröder et al. (1994).
The amplitude of each Fourier component is given by:

where r and θ are polar coordinates, I(ln r, θ) is the intensity at position (ln r, θ), m represents the number of arms or modes, and p is the variable associated with the pitch angle P defined by $\tan(P) = -m/p_{max}$.
IRAF was used to determine the ellipticity values and major-axis position angle in order to deproject the 3.6 μm galaxy images to fully face-on by assuming circular outer isophotes. ELLIPSE in IRAF was used to derive inclination angle (α); (Hubble 1926; Jedrzejewski 1987), which is defined by:

[1] IRAF is distributed by the National Optical Astronomy Observatories, which is operated by the Associated Universities for Research in Astronomy, Inc., under cooperative agreement with the National Science Foundation
[2] http://nedwww.ipac.caltech.edu/

$$\alpha = \cos^{-1}(b/a)$$

where (a) is the semi-major axis and (b) is the semi-minor axis. Where the value 0^o describes a face-on galaxy and 90^o describes an edge-on galaxy,

A two-dimensional fast Fourier Transform (Schröder et al. 1994) was then applied to the deprojected 3.6 μm images. Assuming logarithmic spirals, the spiral arm pitch angles were measured by applying the relationship between SMBH and P discovered by Seigar et al. (2008).

Results and Discussion

By analyzing the sample of 40 spiral galaxies and plotting the L_{bul} − P correlation, we conclude that there is a new correlation between L_{bul} and P. In Table 2, we list the parameters of the best-fitting lines shown for this diagram.

Figures 1-3 illustrate the relations in L-spiral arm pitch angle (we assigned a particular marker to these galaxies according to their morphological bulge type: i.e. bulge and pseudobulge galaxies. In Fig. 1 we note that both pseudobulges and bulges are located between the fitting lines. The best-fitting lines are shown for this diagram:

Pearson's linear correlation coefficient for a correlation between SMBH and L_{bul} is 0.82 for both classical bulges and pseudobulges. This means a strong correlation exists between spiral arm pitch angle and bulge luminosity in late-type galaxies.

Figure 1 shows the correlation of the pitch angle with bulge luminosity distribution for the sample of galaxies described as “bulge” in Table 2, where the scatter looks somewhat large in the L_{bul}-P relation.

Based on the conclusions of Ferrarese (2002 [F02]), Ho (2004), and Ferrarese et al. (2006 [F06]), the L_{bul}-P relation supports the notion of regulated formation mechanisms and co-evolution for the galaxy’s bulge luminosity (the smallest structures in a galaxy) and the pitch angle of a galaxy's spiral arms (the largest structures in a galaxy).

During the decomposition process, the bulge luminosity was measured. For this figure, we have recomputed these values, especially for pseudobulges with $n \leq 2$, to get more accurate results.

Kormendy & Fisher (2008) pointed out that bulges have steep brightness profiles for bulge light in spiral galaxies that often dilute the contrast with the spiral structure, and that bulge light especially affects discernibly of the spiral structure very strongly at smaller galaxy radii. Note, the spiral structure depends little on radius which is essentially a property of the pseudobulge galaxy.

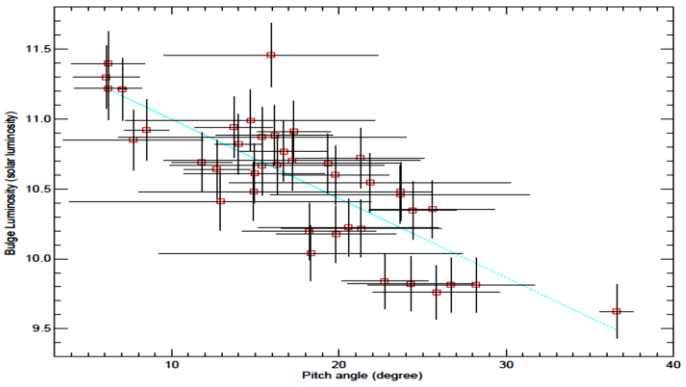

Figure (1): Bulge luminosity (L3.6) as a function of spiral arm pitch angle. The solid line is the fit to all spiral galaxies.

The fundamental L_{bul} – P scaling relation of spiral galaxies was examined while taking into account the nature of the bulge (classical or pseudobulge). Figure 2 illustrates the relations in L_{bul}-P, where the classical bulges and pseudobulges have prominent correlations. The best-fitting lines are shown for this diagram:

Pearson's linear correlation coefficient for the correlation between SMBH and L_{bul} are 0.87, and 0.78 for classical bulges and pseudobulges respectively. We note that Pearson's linear correlation coefficient values for classical bulges and pseudobulges of spiral galaxies are shown to have a strong correlation. These results have a significance of 99.6%, a 3σ.

Figure 2 also demonstrates that there is a statistically significant correlation between the luminosity of the bulge and the spiral arm pitch angle: galaxies with high bulge luminosity have smaller pitch angles. The correlation looks somewhat better for pseudobulges with $n \leq 2$. In addition, pseudobulges with small pitch angles follow the same scaling relations as classical bulges, while those with large pitch angles deviate from the scaling relations of classical bulges.

The pitch angle–bulge luminosity relation (non-barred, AGN, and non-AGN galaxies; Figure (3) shows the same behavior. There is a significant correlation between the pitch angle and the luminosity of the bulge for all of them.

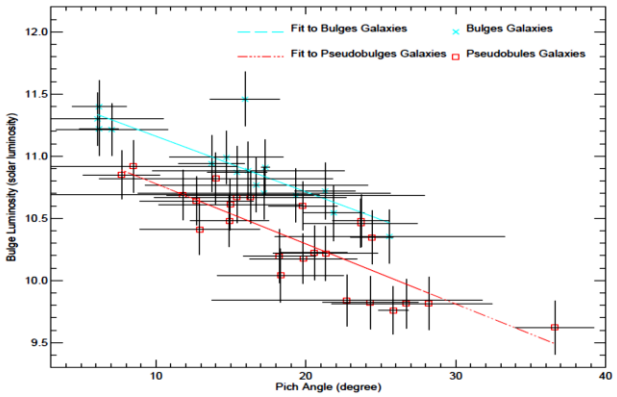

Figure (2): bulge luminosity ($L_{3.6}$) as a function of spiral arm pitch angle. The linear regression are shown as long dash and dash dot dot dot, respectively, for pseudobulges, and bulges galaxies.

Figure 3 shows a plot of SMBH masses calculated from the (L_{bul}-P) relation, for non-barred, non-AGN, and AGN galaxies. Pearson's linear correlation coefficient for a correlation between L_{bul} and P was found to be 0.78, 0.83, and 0.79 for non-barred, non-AGN, and AGN galaxies respectively.

Most of the AGNs are host to low-mass black holes (BHs) (Wandel 2000, Greene & Ho 2006, Hu 2008), so the slope of the L_{bul}–P relation in the AGNs is somewhat low when compared to non-barred, non-AGN galaxies. Pearson's linear correlation coefficient values for all types of galaxies are noted to have the significance level at which the null hypothesis of zero correlation is disproved, is 3σ.

The best-fitting lines are shown in this diagram:

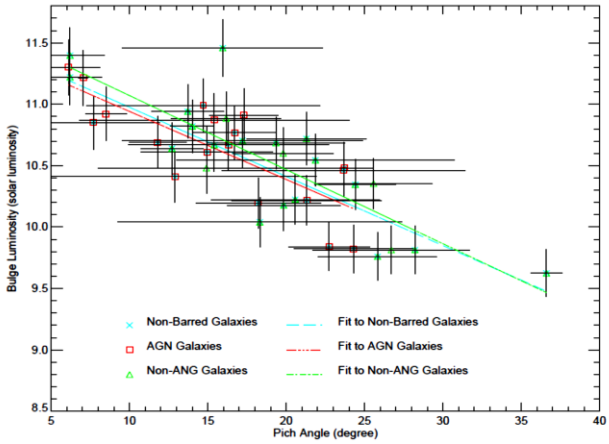

Figure (3): bulge luminosity ($L_{3.6}$) as a function of spiral arm pitch angle. The linear regression are shown as long dash, dash dot dot dot, dash dot and dashed, respectively, for, non-barred, Non-AGN, and AGN galaxies.

Conclusions

Based on this work, the following conclusions can be made:

1- The scaling relations were studied between the bulge luminosity (L_{bul}), and spiral arm pitch angles. The bulge Sérsic index (n) and effective radius (Re) were determined based on a 2D decomposition of 3.6 μm Spitzer/IRAC images of 40 spiral galaxies, and dispersion velocity values obtained from Hyperleda which were used to estimate the bulge luminosity.

2- The relations between bulge luminosity (L_{bul}), and spiral arm pitch angle (P) were investigated using 2D decomposition of Spitzer/IRAC images at 3.6 μm, and the best-fitting linear regressions are:

3- The results of this study indicate that secular evaluation for the pseudobulges and minor mergers for the classical bulges of spiral galaxies played an important role in growing supermassive black hole masses in center of spiral galaxies.

4- A mid-infrared (MIR) view of the M_{BH} scaling relations was used based on a 2D decomposition of Spitzer/IRAC images at 3.6 μm. The high performance of Spitzer/IRAC provided images of advanced quality in the MIR for the 40 spiral galaxies analyzed here. IRAC sensitivity permitted the clear identification of morphological features for spiral galaxies. Bulge luminosity and that of the bulge structure parameters was determined using two-dimensional bulge-disk decompositions of Spitzer/IRAC 3.6 μm images, with high accuracy. A new relation was found to exist between the spiral arm pitch angles and the bulge luminosities of disk galaxies.

Table 1. Columns: (1) galaxy name. (2) Hubble type taken from the Hyper-Leda catalogue. (3) Spiral arm pitch angle (P). Most of (P) taken from Berrier et al. (2013), and Davis et al. (2012). The spiral arm pitch angle given for M31, MW, and NGC 4945 are taken from Braun (1991), Levine et al. (2006) and Burg et al. (1986) respectively. (4) Bulge luminosity.

Name [1]	Leda Type [2]	P (deg) [3]	$L_{Bulge}(L_{\Theta})$ [4]
Circinus	Sb	26.7	9.81
IC 2560	SBb	16.3	10.7
NGC 224	Sb	8.5±1.3	10.9
NGC 613	Sbc	23.68±1.77)1(	10.5

NGC 1022	SBa	19.83±3.6)1(	10.2
NGC 1068	Sb	17.3±2.2)2(	10.9
NGC 1097	SBb	16.7±2.62)3(	10.8
NGC 1300	Sbc	12.7±1.8	10.6
NGC 1350	Sab	20.57±5.38)1(	10.2
NGC 1353	Sb	36.6±5.4)1(	9.62
NGC 1357	Sab	16.16±3.48)1(	10.9
NGC 1365	Sb	15.4±2.4)3(	10.7
NGC 1398	SBab	6.2±2)3(	11.2
NGC 1433	SBab	25.82±3.79)1(	9.76
NGC 1566	SABb	21.31±4.78)3(	10.2
NGC 1672	Sb	18.22±14.07)3(	10.2
NGC 1808	Sa	23.65±7.77)1(	10.5
NGC 2442	Sbc	14.95±4.2)1(	10.6
NGC 3031	Sab	15.4±8.6	10.9
NGC 3227	SABa	12.9±9	10.4
NGC 3368	SABa	14±1.4	10.8
NGC 3511	SABc	28.21±2.27)1(	9.81
NGC 3521	SABb	21.86±6.34)3(	10.5
NGC 3673	Sb	19.34±4.38)1(	10.7
NGC 3783	SBab	22.73±2.58)1(	9.84
NGC 3887	Sbc	24.4±2.6)2(	10.3
NGC 4030	Sbc	19.8±3.2)2(	10.6
NGC 4151	SABa	11.8±1.8	10.7
NGC 4258	SABb	7.7±4.2	10.9
NGC 4462	SBab	17.2±5.42)1(	10.7
NGC 4594	Sa	6.1	11.3
NGC 4699	SABb	6.2±2.2)1(	11.4
NGC 5054	Sbc	25.57±3.73)1(	10.4
NGC 5055	Sbc	14.9±6.9	10.5
NGC 6300	SBb	24.3±3.8)1(	9.82
NGC 6902	SBab	13.71±2.3)3(	10.9
NGC 7213	Sa	7.05±0.28)1(	11.2
NGC 7531	SABb	18.31±9.09)1(	10
NGC 7582	SBab	14.7±7.44)3(	11
NGC 7727	SABa	15.94±6.39)1(	11.5

Table 2: Linear correlation coefficient and linear regression coefficients of bulge luminosity as a function of the spiral arm pitch angle, $[\log(L_{Bul}) = \alpha - \beta P]$

Types of galaxies	A	β	No. of galaxies	correlation coefficient
All galaxies	11.56 ± 0.81	0.056 ± 0.015	40	0.87
Pseudobulge galaxies	11.6 ± 0.4	0.044 ± 0.01	25	0.78
Classical Bulge galaxies	11.26 ± 0.25	0.048 ± 0.013	16	0.78
Non-Barred galaxies	11.53 ± 0.7	0.056 ± 0.01	14	0.83
AGN galaxies	11.49 ± 0.4	0.055 ± 0.008	18	0.79
Non-AGN galaxies	11.67 ± 0.5	0.06 ± 0.009	23	0.83

Literature Cited

Agura H, A. Suzuki, T. Matsushita, T. Aoki and **M. Okuda**. 2003. Low resistivity transparent conducting Al-doped ZnO films prepared by pulsed laser. Thin Solid Films 445: 263-267.

Aller, M. C., & Richstone, D. O., 2007, Host galaxy bulge predictors of supermassive black hole mass, ApJ, 665, 120.

Benson, A. J., & Bower, R., 2010, Galaxy formation spanning cosmic history, MNRAS, 405, 1573-1623.

Bertin E., Arnouts S., 1996, SExtractor: Software for source extraction, A&AS, 117, 393.

Davies B., Origlia L., Kudritzki R. P., Figer D. F., Rich R. M., Najarro F., Negueruela I., Clark J. S., 2014,Chemical abundance patterns in the inner galaxy: the scutum red supergiant clusters, ApJ, 696, 2014-2925.

Davis, B. L., Berrier, J. C., Shields, D. W., Kennefick, J., Kennefick, D., Seigar, M. S., 2012,Spiral arm pitch angle using two-dimensional fast fourier transform decomposition measurement of galactic logarithmic, ApJS, 199:33.

Elmegreen, B. G., Elmegreen, D. M., and Hirst, A. C., 2004, A Constant Bar Fraction out to Redshift z ~ 1 in the Advanced Camera for Surveys Field of the Tadpole Galaxy, ApJ, 612, 191.

Ferrarese, L., and Merritt, D., 2000, A Fundamental Relation between Supermassive Black Holes and Their Host Galaxies, ApJ, 539, L9–L12.

Ferrarese, L., 2002, Beyond the Bulge: A Fundamental Relation between Supermassive Black Holes and Dark Matter Halos, ApJ, 578:90–97.

Gebhardt K. et al., 2000b, A Relationship between Nuclear Black Hole Mass and Galaxy Velocity Dispersion, ApJ, 539, L13.

Gebhardt, K., Rich R. M. and Ho L. C., 2005, A 20,000 M_{solar} Black Hole in the Stellar Cluster G1, ApJ, 634, 1093.

Graham A. & S. P. Driver, 2007a, A Log-Quadratic Relation for Predicting Supermassive Black Hole Masses from the Host Bulge Sérsic Index, ApJ, 655, 77.

Graham, A. W., Erwin, P., Caon, N., & Trujillo G., 2001, A Correlation between Galaxy Light Concentration and Supermassive Black Hole Mass ApJ, 563, L11.

Gültekin, K., et al., 2009b, A Quintet of Black Hole Mass Determinations, ApJ, 695, 1577.

Häring, N., and Rix, H.-W., 2004, On the Black Hole Mass-Bulge Mass Relation, ApJ, 604, L89.

Hu J., 2009, The black hole mass–bulge mass correlation: bulges versus pseudo-bulges, MNRAS, 386, 2242-2252.

Hubble, E. P., 1926, Extragalactic nebulae, ApJ, 64, 321.

Jedrzejewski, R. I., 1987, **Hu J.,** 2009, CCD surface photometry of elliptical galaxies. I - Observations, reduction and results, MNRAS, 226, 747.

Kennicutt, R. C., **1981**, The shapes of spiral arms along the Hubble sequence, AJ, 86, 1847.

Kormendy, J. and Richstone, D. O., Hu, Inward Bound---The Search For Supermassive Black Holes In Galactic Nuclei, 1995 ARA&A, 33, 581.

Kormendy, J., & Fisher, D. B., 2005, Structure and formation of elliptical and spheroidal galaxies, RevMexA&A (Serie de Conferencias), 23, 101.

Kormendy, J., and Gebhardt, K., 2001, Supermassive black holes in galactic nucleiJ., &, in AIP Conf. Proc. 586, 20th, Texas.

Lauer. T. R., Tremaine S., Rich stone D., and Faber. Selection S. M., 2007, Selection Bias in Observing the Cosmological Evolution of the M•-σ and M•-L Relationships, ApJ, 670, 249.
Laurikainen, E., Salo, H., and Buta, R., 2005, Multicomponent decompositions for a sample of S0 galaxies, MNRAS, 362, 1319.
Lin, C. C., and Shu, F. H., 1964, On the Spiral Structure of Disk Galaxies, ApJ, 140, 646.
Magorrian J., Tremaine S., Richstone D. et al., 1998, The Demography of Massive Dark Objects in Galaxy Centers, AJ, 115, 2285.
Marconi, A. and Hunt, L. K., 2003, The Relation between Black Hole Mass, Bulge Mass, and Near-Infrared Luminosity, ApJ 589, L21–L24.
McLure, R. J., & Dunlop, J. S., 2001, The cluster environments of powerful radio-loud and radio-quiet active galactic nuclei MNRAS, 321, 515.
Robertson B., Cox T. J., Hernquist L., Franx M., Hopkins P. F., Martini P., Springel V, 2006a, The Fundamental Scaling Relations of Elliptical Galaxies, ApJ, 641, 21.
Sani E., Marconi A, Hunt L. K., Risaliti G., 2011, The Spitzer/IRAC view of black hole-bulge scaling relations, MNRAS, 413:1479-94.
Schröder, M. F., Pastoriza, M. G., Kepler, S. O., and Puerari, I.,1994, A&AS, 108, 41.
Seigar, M. S., and James, P. A., 1998a, MNRAS, 299, 672.
Seigar, M. S., and James, P. A., 1998b, MNRAS, 299, 68532, 1391, 04.14.
Seigar, M. S., Bullock, J. S., Barth, A. J., Ho, L. C., 2006a, ApJ, 645, 1012.
Seigar, M. S., Kennefick, Kennefick, J., and Lacy, C.H.S., 2008, ApJ, 678, L93.
Seigar, M. S., 1998b, MNRAS, 299, 685.
Tremaine, S., Gebhardt, K. and Bender, R., 2002, ApJ, 574, 740.
Treuthardt, P., Seigar, M. S., Sierra, A. D., Al-Baidhany, I., Salo, H., 2012, MNRAS,
Valeri. P. Frolov and Igor D. Novikov, 1998, Black Hole Physics: Basic Concepts and New, Developments, Kluwer academic publishers.
Vallée, J. P., 2002, ApJ, 566:261-266.
Wald, Robert M., 1984, General Relativity, University of Chicago Press.
Wandel, A., 2002, ApJ, 565, 762.

Study of New Correlations between Bulge Velocity Dispersion and Bulge luminosity of Spiral Galaxies

Wasmaa A. Jabbar[1], Ismaeel A. Al-Baidhany[1*], Ashwaq Ali Ismail[2]
[1]Department of Physics, College of Education, Mustansiriyah University, Baghdad – Iraq
[2] Educational Rusafa Directorate-1
***Author for correspondence: E-mail: ismaeel_2000@uomustansiriyah.edu.iq.**

Abstract:
In this work, we have studied new correlations between velocity dispersion of the bulge and bulge luminosity, using 40 images of spiral galaxies.
This paper is based on two dimensions, bulge-disc-bar decompositions of images of 40 spiral galaxies at 3.6μm from Spitzer/IRAC with velocity dispersion values. Our estimates of velocity dispersions from the literature. We identified the bulges of spiral galaxies into classical bulges and pseudo-bulges by using model decomposition, and compare their characteristics with velocity dispersions. Using these data, we analysed the behaviour of the coefficients and the intrinsic dispersion. In this work, novel correlations had been submitted in this work as far as authors know. Throughout this paper, we use H_0=70kms^{-1}M pc^{-1}, Ωm=0.3 and ΩΛ=0.7.
Keywords: galaxies: classical bulges – pseudo-bulges, photometry – infrared.

المستخلص:
في هذا العمل، درسنا الارتباطات الجديدة بين تشتت سرعة الانتفاخ وإضاءة الانتفاخ باستخدام 40 صورة لمجرات حلزونية. تستند هذه الورقة إلى بعدين، تحلل شريط الانتفاخ القرصي لصور 40 مجرة حلزونية عند 3.6 ميكرومتر من Spitzer/IRAC مع قيم تشتت السرعة. تقديراتنا لسرعة تشتت من الأدبيات. حددنا انتفاخات المجرات الحلزونية في الانتفاخات الكلاسيكية والانتفاخات الزائفة باستخدام نموذج التحلل ومقارنة خصائصها مع تشتت السرعة. باستخدام هذه البيانات، قمنا بتحليل سلوك المعاملات والتشتت الجوهري. في هذا العمل، تم تقديم ارتباطات جديدة في هذا العمل على حد علم المؤلفين. في هذا البحث، نستخدم H_0=70kms^{-1}M pc^{-1}, Ωm=0.3 and ΩΛ=0.7.
كلمات المفتاحية: المجرات: الانتفاخات الكلاسيكية - الانتفاخات الزائفة، القياس الضوئي - الأشعة تحت الحمراء.

Introduction

During the last ten years, researches of galaxies drove to the detection that there are many tight relationships locally among the center of galaxies and the global features of their hosts. Accordingly, astronomers think that the energy emitted play significant functions in forming the characteristic of the components of the host galaxies [1, 2, 3].
There is growing proof that point out those correlations among the center of galaxies and almost the possible parameters of the host galaxies. The mass of the central (SMBH) of galaxy relates with bulge velocity dispersion (σ*) [4, 5, 6], with luminosity of the bulge of the galaxy (L_{bul}) [7, 8, 9, 10, 11], with the staller mass of bulge (M_{bulge}) [8, 10], with rotation velocity [12], with effective radius of the bulge [9], the Sersic index [13, 14], with the integration of effective radius of the bulge and dispersion velocity [15], and spiral arm pitch angles [16].
In this work, the sample galaxies are divided into those classical bulges and those pseudobulges based on the value of Sérsic indices (n_b) and the ratio of bulge-to-total (B/T) luminosities. Two methods were used for this classification: first, classical bulges have n_b> 2 whereas, pseudobulges have $n_b \leq 2$ [17]. Second, the value (B/T) of classical bulge is (0.4), and the value (B/T) of pseudobulge is (0.16)[7, 17]. The morphological Hubble types of spiral galaxies have taken from HYPERLEDA[1].

[1]http://leda.univ-lyon1.fr/

In this paper, using sophisticated techniques of measuring the bulge luminosity on a two dimensions, decomposition of images of 40 spiral galaxies at band 3.6 μm from Spitzer/IRAC and stellar velocity dispersions, produces an even tighter relationship among the luminosity of bulges and the parameters of the bulges (stellar velocity dispersions) for (classical bulges, pseudobulges, barred, non-barred, AGN, and non-AGN).

Methods

The bulge luminosity Measurement (L_{bulge}).

The magnitudes of the luminosity of bulges are using a program of 2D (bulge - bar - disk) decomposition from Spitzer/IRAC at 3.6 um band [18]. The luminosity of bulge determined for 40 images of spiral galaxies based on 2D decomposition technique. In this technique, the exponential function applied to characterize the galactic disc:

$$I_d(r) = I_{od} \exp[-(r/h_r)]$$

where I_{od} is the density of central surface of the disc, h_r is the radial disc scale length, and r is radius of the disc. The exponential function applied to characterize the bulge that described by a Sersic function:

$$I_b(r_b) = I_{0b} \exp\left[-(r_b/h_b)^{\beta}\right]$$

where I_{ob} is the density of central region of the bulge, h_b is the parameter of scale of the bulge, and $\beta=1/n$, where (n) is the index of sérsic parameter. The half-light radius (r_e), for the bulge was gotten by using h_b,

$$r_e = (b_n)^n h_b$$

where: b_n is a constant of proportionality, that is $\Gamma(2n) = 2\gamma(2n,b_n)$, and γ and Γ are the incomplete and complete gamma functions. In this work, used the approach $b_n \approx 2.17n_b - 0.355$ [19], where n_b is Sersic index for the bulge.

The bars are measured using a Sersic function:

$$I_{bar}(r_{bar}) = I_{0bar}(1 - (r_{bar}/a_{bar})^2)^{n_{bar}+0.5}, \; r_{bar} < a_{bar}$$
$$= 0 \qquad\qquad\qquad\qquad , \; r_{bar} > a_{bar}$$

where I_{0bar} is the center of region brightness for the b_{ar}, a_{bar} is the major axis of bar, and n_{bar} is the indicator of the bar model.

First, front stars have been removed and all the sources of point from the images using SExtractor programme [20], next, applying the ELLIPSE routine in IRAF[2], the profiles of surface brightness were derived [18, 21]. To change the units of surface brightness to mag arcsec^{-2}, the next formula was applied:

$$\mu_{3.6\mu m} = -2.5 \times \log_{10}\left[\frac{S_{3.6\mu m} \times 2.35 \times 10^{-5}}{ZP_{3.6\mu m}}\right]$$

Where $S_{3.6\mu m}$ is the measurement of flux of the 3.6 μm by units of MJy sr^{-1}, $ZP_{3.6\mu m}$ is the IRAC zero magnitude flux density in Jy and the value is 280.9 [22, 23].

Apparent magnitude ($m_{3.6\mu m}$) was transformed to absolute magnitude ($M_{3.6\mu m}$) was transform applying luminosity distance of the galaxies based on the (NED) database.

The resultant 3.6 μm magnitude of each object is listed in column 3 of Table (1) Absolute magnitudes were measured applying the standard relation:

$$M_{3.6\mu m} = m_{3.5\mu m} - 5 \log d + 5 \quad \ldots (1)$$

Where (d) is the luminosity distance in parsecs. The luminosity of bulge of the galaxy was estimated using a relation:

$$\log (L_{3.6\mu m}/L_o) = 0.4(-M_{3.6\mu m} + 3.24) \quad \ldots (2)$$

[2] IRAF is distributed by the National Optical Astronomy Observatories, which is operated by the Associated Universities for Research in Astronomy, Inc., under cooperative agreement with the National Science Foundation

Measurement bulge velocity dispersion:

In this work, dispersion velocity were gotten in spiral galaxies from the literature, and applying the relation for circular velocity (V_c) and dispersion velocity (σ^*) [12].

The relationship of V_c– σ_* is one of the best common methods applied to measure The velocity of the stellar surrounding component (bulge) [2, 12]. This is found by estimating the rotation velocity in the disk of galaxy. This relation derive from the observation that rotation velocity relate with the dispersion velocity.

The rotation velocity (V_c) of spiral galaxies were transformed to velocity dispersion (σ_*) applying the relation [12]:

$$\log V_c = (0.84 \pm 0.09) \log \sigma + (0.55 \pm 0.19) \quad \dots (3)$$

Results and discussion

By analyzing the sample of 40 images of galaxies and studying of the L_{bulge} – σ^* correlation, we concluded there is a novel correlations between L_{bul} and σ^*. In Table (2), we list the parameters shown for the best-fitting lines for these diagrams.

According to the NED database, we used luminosity distance of the spiral galaxies to convert the apparent magnitude to absolute magnitude.

The bulge luminosity was calculated using the magnitudes obtained with the two-dimensional decomposition at 3.6 μm and applying the standard relation:

$$\log L_{3,6}/L_{\odot} = 0.4(-M_{3.6} + 3.24)$$

where (3.24) is the value of absolute magnitude of the Sun at 3.6μm band [23]. An uncertainty of ±0.2 d_{ex} was assumed for the bulge luminosities [24].

To determine the bulge luminosity – dispersion velosity relations, we used the following form: $L_{bul} = \propto + \beta(logx - x_{\circ})$. The fitting results of L_{bul} – σ^* correlations are presented in Table (2).

Figure (1) explains the relationship in (L_{bulge}- σ^*) (we appointed special These galaxies' marker based on their morphological type of the bulge - i.e. galaxies have classical bulges and pseudobulges in Figure (1) was found that both classical bulges and pseudobulges are existing among the fitting line. The best-fitting line is displayed for this figure:

$$\log_{10} L_{3.6} = (0.01 \pm 0.01)\sigma * + (9.07 \pm 0.35)$$

Pearson's linear relation coefficient for a relation for L_{bulge} and dispersion velocity is 0.74 for classicalbulges and pseudobulges. That implies, a good relationship exists among bulge luminosity and the dispersion velocity in spiral galaxies. Figure (1) illustrates the relation of bulge luminosity with the dispersion velocity division for the sample of spiral galaxies characterized the bulges in Table (2), we noted the scatter looks somewhat not large in the L_{bul}-σ^* relation.

In this work, we presented a study of the scaling relations for parameters of the host in the spiral galaxies, which are shown by bulge luminosity (L_{bulge}), using 2D- disk - bulge-bar decompostions at 3.6 μm band of 40 galaxies.

The good about this work is that the bulge luminosity is used a big number of pseudobulges overriding the number of pseudobulges applied in most of the researches as far as authors know [25, 26]. That means that a sample in this study is the largest samples used so far to study L_{bulge}- σ^* relations compared with previous works.

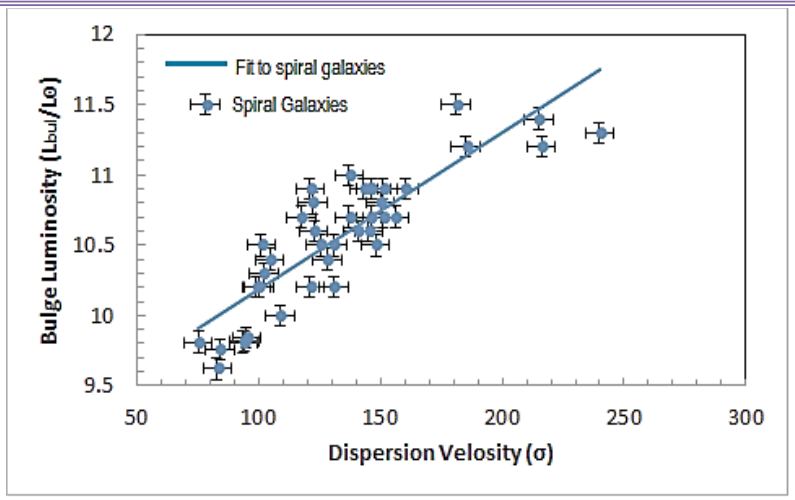

Fig 1: Bulge luminosity ($L_{3.6}$) versus the dispersion velocity (σ*). The line is the fit to galaxies

The fundamental L_{Bulge} – σ* scaling relationships of galaxies was studied taking into calculation the nature of the bulge (classic or pseudo-bulges). Figure (2) clarifies the relationships in L_{bul}-σ*, and the classicalbulges and pseudobulges have distinguished relations. This diagram shows the best-suited lines:

$$\log_{10} L_{3.6} = (8.81 \pm 0.4) + (0.012 \pm 0.001)\sigma * \quad \text{pseudobulges}$$
$$\log_{10} L_{3.6} = (9.6 \pm 0.25) - (0.008 \pm 0.0013)\sigma * \quad \text{classical bulges}$$

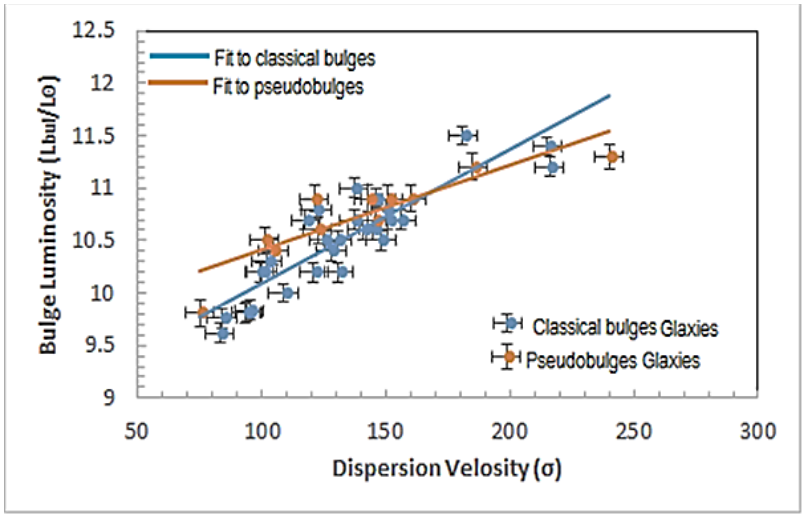

Fig. 2: Bulge luminosity ($L_{3.6}$) as a function of the linear regressions for pseudobulges, and bulges galaxies respectively

Figure (2) presents the L_{bulge} versus σ* divison for the galaxies represented as classicalbulge and pseudobulge in Table (2), we found the large scatter in the L_{bulge}- σ* relation was noted by us and many authors for another correlations [25, 26].

Pearson's linear coefficient was found for correlations for $L_{3.6}$ and σ* are 0.77 and 0.78. We find that Pearson's linear correlation coefficient value for the two kinds of galaxies

shows a moderate correlation. Attention has been drawn by a number of researchers [14, 25, 27, 28, 29] to the coexistence of pseudobulges and σ*.

Also, the figure above shows that 12 out of 23 pseudobulges galaxies are consistent with the relationship for classic bulges, and the others are inconsistent with the linear regression for this correlation.

Obviously, in these kind of structures for spiral galaxies appears to be better correlated with the small classical bulge [26, 28, 29, 30]. Multiple studies confirmed that classicalbulges and pseudo-bulges can coexist in the same galaxy [7, 31, 32, 33, 34, 35]. The two-dimensional bulge-disk decompositions [18] of Spitzer/IRAC 3.6 μm is very important to identify the type of the central bulge [18, 28, 36], whether, classical bulge or pseudobulges or both of them.

These outlier galaxies would then have (σ*) which corresponds to their original L_{bul}, but a lower current L_{bulge}. This could illustrate why they are outliers in the L_{bul}-σ* correlation.

The bulge luminosity – dispersion relations (barred, and non-barred galaxies) (Figure (3) explain the behaviour are the same. Pearson's linear coefficient for a relation for L_{bul} and σ* are 0.77, and 0.781 for barred and non-barred, galaxies, respectively. There is a significant correlation between the luminosity of bulge and dispersion velocity for all of them. This diagram shows the best suited lines:

$$\log_{10} L_{3.6} = (8.95 \pm 0.5) + (0.012 \pm 0.002)\sigma * \text{ barred galaxies}$$
$$\log_{10} L_{3.6} = (9.6 \pm 0.25) - (0.01 \pm 0.001)\sigma * \text{ Non} - \text{barred galaxies}$$

Figure (4) displays a plot of (L_{bul}-σ*) relation, for AGN, and non-AGN galaxies, respectively. Pearson's linear coefficient for a relation for L_{bul} and σ* are 0.74, and 0.76 for AGN, and non-AGN galaxies. The best fitting lines for this diagram are:

$$\log_{10} L_{3.6} = (9.11 \pm 0.7) + (0.010 \pm 0.001)\sigma * \text{ AGN galaxies}$$
$$\log_{10} L_{3.6} = (9.6 \pm 0.25) - (0.01 \pm 0.001)\sigma * \text{ Non} - \text{AGN galaxies}$$

As most of the AGNs have low-mass black holes (BHs) [25, 27]. A comparison to non-barred, non-AGNs, it is very low in the AGNs in the slope of the L_{bul}–σ* relationship for all types of galaxies, Pearson's linear correlation coefficient values were noted to have the degree of significance at Which is disproved at 3σ by the null hypothesis of zero correlation.

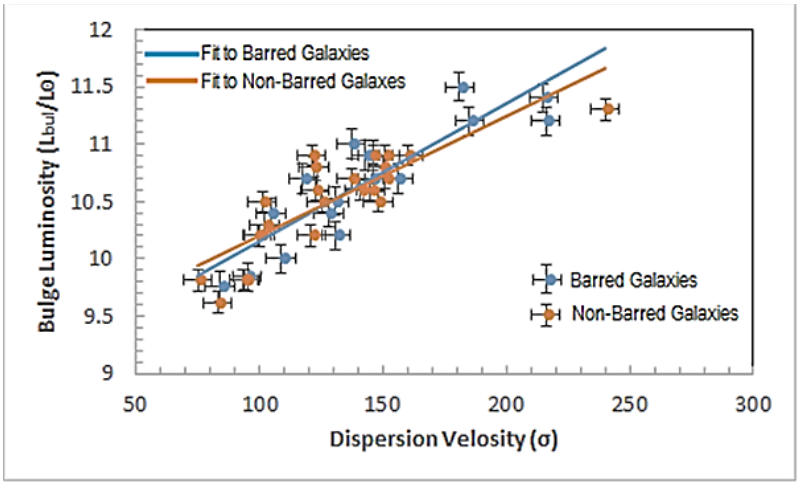

Fig. 3: Bulge luminosity (L) versus the linear regressions for barred, and non-barred galaxies respectively.

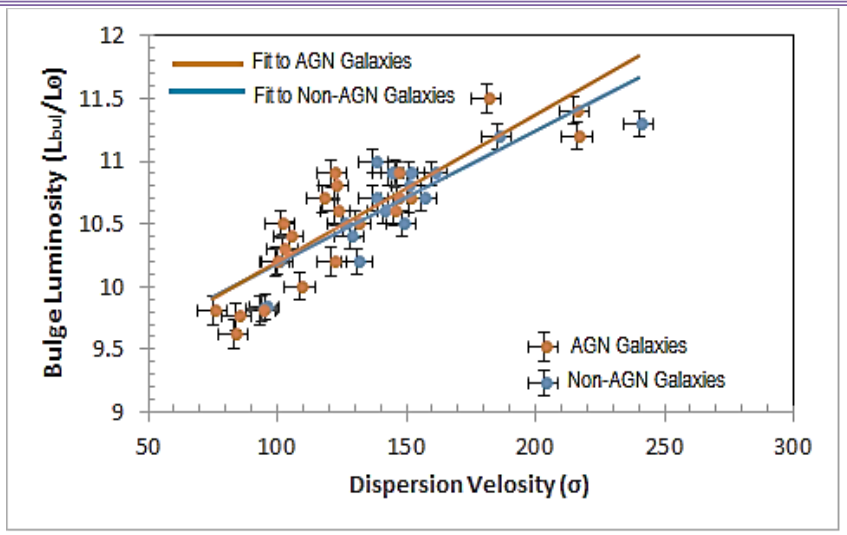

Fig. 4: Bulge luminosity (L) versus the linear regressions for Non-AGN, and AGN galaxies respectively.

Table (1): Estimated Galaxy Parameters. Columns: (1) names of galaxy. (2) Hubble type of spiral galaxy (3) Stellar Velocity dispersion, references: [11, 12, 25, 26, 27, 37, 38, 39, 40, 41, 42, 43, 44, 45, 46,47, 48, 49, 50, 51, 52, 53, 54,55, 56]; (*) dispersion velocity estimated from V − σ* relation. (4) Bulge luminosity. (5), B-Barred galaxy; nB - Non-Barred galaxy. (6) AGN and non-AGN. (7), C – classicalbulge; P – pseudo-bulge.

Name (1)	Leda Type (2)	σ* (km/sec) (3)	$L_{Bulge}(L_{\odot})$ (4)	B or nB (5)	AGN or AGN (6)	C or P (7)
Circinus	Sb	75	9.81	nB	nAGN	P
IC 2560	SBb	137	10.7	B	AGN	P
NGC 224	Sb	160±8	10.9	nB	AGN	P
NGC 613	Sbc	125.3±18.9	10.5	B	AGN	P
NGC 1022	SBa	99	10.2	B	nAGN	P
NGC 1068	Sb	151±7	10.9	nB	AGN	P
NGC 1097	SBb	150	10.8	B	AGN	P
NGC 1300	Sbc	145±22	10.6	B	nAGN	P
NGC 1350	Sab	120.91±2.08*	10.2	B	nAGN	P
NGC 1353	Sb	83	9.62	B	nAGN	P
NGC 1357	Sab	121±14	10.9	nB	nAGN	P
NGC 1365	Sb	151±20	10.7	B	nAGN	P
NGC 1398	SBab	216±20	11.2	B	nAGN	C
NGC 1433	SBab	84±9	9.76	B	nAGN	C
NGC 1566	SABb	100±10	10.2	B	AGN	P
NGC 1672	Sb	130.8±2.09*	10.2	B	AGN	C
NGC 1808	Sa	148	10.5	B	AGN	P
NGC 2442	Sbc	140.74±2.18*	10.6	B	AGN	P
NGC 3031	Sab	143±7	10.9	nB	AGN	C
NGC 3227	SABa	128±13	10.4	B	AGN	C
NGC 3368	SABa	122±(28,24)	10.8	B	nAGN	P
NGC 3511	SABc	93.56±2.04*	9.81	B	nAGN	P
NGC 3521	SABb	130.5±7.1	10.5	B	nAGN	C

NGC 3673	Sb	117.45±2.07*	10.7	B	nAGN	C
NGC 3783	SBab	95±10	9.84	B	AGN	C
NGC 3887	Sbc	102.01±2.05*	10.3	B	nAGN	P
NGC 4030	Sbc	122.43±2.1*	10.6	nB	nAGN	P
NGC 4151	SABa	156±8	10.7	B	AGN	C
NGC 4258	SABb	146±15	10.9	B	AGN	P
NGC 4462	SBab	146±8	10.7	nB	nAGN	C
NGC 4594	Sa	240±12	11.3	nB	AGN	P
NGC 4699	SABb	215±10	11.4	B	nAGN	C
NGC 5054	Sbc	104.48±2.05*	10.4	nB	nAGN	C
NGC 5055	Sbc	101±5	10.5	nB	nAGN	P
NGC 6300	SBb	94±5	9.82	B	AGN	P
NGC 6902	SBab	145.86±2.1*	10.9	B	nAGN	C
NGC 7213	Sa	185±20	11.2	nB	AGN	C
NGC 7531	SABb	108.7±5.6	10	B	nAGN	C
NGC 7582	SBab	137±20	11	B	AGN	C
NGC 7727	SABa	181±10	11.5	B	nAGN	C

Table (2): coefficients of linear correlation and linear regression of bulge luminosity and of the dispersion velosity, [$\log(L_{Bul}) = \alpha - \beta\sigma^*$]

Types of galaxies	α	β	No. of galaxies	correlation coefficient
All galaxies	11.56 ± 0.81	0.056 ± 0.015	41	0.87
Pseudobulges galaxies	11.6 ± 0.4	0.044 ± 0.010	25	0.78
Classical Bulges galaxies	11.26 ± 0.25	0.048 ± 0.013	16	0.78
Barred galaxies	11.53 ± 0.70	0.056 ± 0.010	14	0.83
Non-Barred galaxies	11.53 ± 0.70	0.056 ± 0.010	14	0.83
AGN galaxies	11.49 ± 0.40	0.055 ± 0.008	18	0.79
Non-AGN galaxies	11.67 ± 0.50	0.06 ± 0.009	23	0.83

Conclusions

In this work, novel correlations had been submitted in this work as far as authors know. We found new relations observed in the local Universe for the bulge luminosity and the stellar dispersion velocity of the host bulges. The analysis of this result is based a programme of two dimensions decomposition of 3.6 μm band from Spitzer/IRAC of 40 images of galaxies.

The relationships between bulge luminosity (L_{Bul}), and the dispersion velocity (σ^*) were investigated using 2D decomposition of Spitzer/IRAC galaxies at 3.6 μm, and the best-fitting lines regressions were:

$\log_{10} L_{3.6} = (9.07 \pm 0.35) - (0.011 \pm 0.001)\sigma *$

$\log_{10} L_{3.6} = (8.81 \pm 0.4) - (0.012 \pm 0.01)\sigma *$ (pseudobulges)

$\log_{10} L_{3.6} = (9.60 \pm 0.25) - (0.008 \pm 0.001)\sigma *$ (classical bulges)

$\log_{10} L_{3.6} = (8.95 \pm 0.5) - (0.012 \pm 0.002)\sigma *$ (Barred)

$\log_{10} L_{3.6} = (9.6 \pm 0.25) - (0.01 \pm 0.001)\sigma *$ (Non − Barred)

$\log_{10} L_{3.6} = (9.11 \pm 0.7) - (0.010 \pm 0.001)\sigma *$ (AGN)

$\log_{10} L_{3.6} = (9.6 \pm 0.25) - (0.01 \pm 0.001)\sigma *$ (Non − AGN)

In this work, the results support the finding of the previous studies that indicated secular evaluation for the pseudobulges of spiral galaxies and minor mergers for the classical bulges played an important function in studying the universe.

Acknowledgments:
The authors would like to thank Mustansiriyah University (www.uomustansiriyah.edu.iq) Baghdad- Iraq for its support in the present work.

References

[1] Benson A. J.; Bower R. (2010) MNRAS, 405, 1573-1623.
[2] Al-Baidhany, I., Rashid. H. G., Chiad, S. S., Habubi, N. F., Jandow, N. N, Jabbar, W. A.,7, Abass, k. H., 2018, Novel Relationship among Spiral Arm Pitch Angles (p) and momentum parameter of the host spiral galaxies, IOP Conf. Series: Journal of Physics: Conf. Series 1003: 012107.
[3] Ismaeel A Al-Baidhany, Sami S Chiad, Wasmaa A Jabbar, Rasha A Hussein, Firas F K Hussain and Nadir F Habubi, 2019, Theoretical investigation for the relation (supermassive black hole mass) – (spiral arm pitch angle): a correlation for galaxies with classical bulges, IOP Conf. Series: Materials Science and Engineering 571, 012118.
[4] Ferrarese L and Merritt D 2000 ApJ 539L9–L12.
[5] Gebhardt K 2000, ApJ, 539 L13.
[6] Tremaine S Gebhardt K and Bender R 2002 ApJ. 574 740.
[7] Kormendy, J., & Kennicutt, R. C. 2004, ARA&A, 42, 603 (KK04).
[8] Magorrian J Tremaine S and Richstone D. 1998 AJ, 1152285.
[9] Marconi A and Hunt L K 2003 ApJ 589 L21–L24.
[10] Häring N and Rix H.-W 2004, ApJ 604 L89.
[11] Gültekin K 2009 ApJ. 695 1577.
[12] Ferrarese L 2002 ApJ 578 90–97.
[13] Graham A W Onken C. A Athanassoula E and Combes F 2011 412 (4) 2211-2228.
[14] Graham A. & S. P. Driver, 2007, ApJ, 655, 77.
[15] Aller M Cand Richstone D O 2007 ApJ 665 120.
[16] Seigar, M. S., Kennefick, D., Kennefick, J., & Lacy, C.H.S. 2008, ApJ, 678, L93.
[17] Fisher D Band Drory N 2008 AJ 136 773.
[18] Laurikainen, E., Salo, H., & Buta, R. , MNRAS, 362, 1319.
[19] Ismaeel A. Al-Baidhany, Sami Salman Chiad, Wasmaa A. Jabbar, Nadir Fadhil Habubi, Tahseen H. Mubarak, Abdulhussain Abbas Khadayeir, Ehssan S. Hassan, Mohamed Odda Dawod and Khalid Haneen Abass, 2019, A New Correlation between Galaxy Stellar Masses and Spiral Arm, IOP Conf. Series Journal of Physics Conf. Series 1234 (2019) 012105.
[20] Bertin E., Arnouts S., 1996, SExtractor: Software for source extraction, A&AS, 117, 393.
[21] Jedrzejewski, R. I., 1987, Hu J., 2009, CCD surface photometry of elliptical galaxies. I- Observations, reduction and results, MNRAS, 226, 747.
[22] Rees, M.J., 1984a, Ann. Rev. Astr. Ap., 22, 471.
[23] Oh, S.-H., de Blok,W. J. G.,Walter, F., Brinks, E., & Kennicutt, R. C. 2008, AJ,136,2761.
[24] Ismaeel A. Al-Baidhany, Sami Salman Chiad, Wasmaa A. Jabbar, Nadir Fadhil Habubi1, Tahseen H. Mubarak, Abdulhussain Abbas Khadayeir, Ehssan S. Hassan, Mohamed Odda Dawod and Khalid Haneen Abass, 2019, A Comparison between Different Methods to Study the Supermassive Black Hole Mass - Pitch Angle Relation, IOP Conf. Series Journal of Physics Conf. Series 1294 (2019) 022010.
[25] Hu J., 2009, ArXiv:0908.2028;2009.
[26] Sani E Marconi A Hunt L K and Risaliti G 2011, MNRAS413 14 79-94.
[27] Greene J. E., Ho L. C., 2006, ApJ 641, L21.

[28] Nowak N., J. Thomas, P. Erwin, R. P. Saglia, R. Bender and R. I. Davies,, Mon. Not. R. Astron. Soc. 403, 646–672 (2010).
[29] Treuthardt, P., Seigar, M. S., Sierra, A. D., Al-Baidhany, I., Salo, H., 2012, On the link between central black holes, bar dynamics, and dark matter halos in spiral galaxies, MNRAS, 423, 3118..
[30] Davis, L. B., Graham A. W., & Seigar, M. S. 2018, Updating the (supermassive black hole mass) (spiral arm pitch angle) relation: a strong correlation for galaxies with pseudobulges, MNRAS (1-18)
[31] Erwin P., Beltrán J. C. V., Graham A. W., Beckman J. E., 2003, When Is a Bulge.
[32] Athanassoula E. 2005, MNRAS, 358, 1477.
[33] Kormendy J and Richstone D O 1995ARA&A 33 581.
[34] Erwin P., 2008, IAU Symposium 245, pp. 113–116.
[35] Erwin, P. 2007, in IAU Symposium 245, Formation and Evolution of Galaxy Bulges, ed. M. Bureau et al. (Cambridge: Cambridge Univ. Press).
[36] Lauer. T. R., Tremaine S., Rich stone D., & Faber.Selection S. M., (2007), ApJ, 670, 249.
[37] Lucey J. R., Guzman R., Steel J., Carter D.; 1997, MNRAS, 287, 899.
[38] Beifiori A., Sarzi M., Corsini E. M., Dalla Bont`a E., Pizzella A., Coccato L., Bertola F.,, 2009, ApJ, 692, 856 (B09),.
[39] García-Burillo, S., Combes, F., Hunt, L. K., Boone, F., Baker, 2003, A.J., et al. . Astron. Astrophys. 407:485.
[40] Davies B., Origlia L., Kudritzki R. P., Figer D. F., Rich R. M., Najarro F., Negueruela I., Clark J. S., 2009, ApJ, 696, 2014,
[41] Douglas 1995, ApJS, 100, 105, A,.
[42] Lauer, T. R., Faber, S. M., Richstone, D., et al. 2007, ApJ, 662, 808,
[43] Oliva, E., Origlia, L., Kotilainen, J.K., Moorwood, A. F. M., 1995, A&A 301, 55.
[44] Whitmore, B. C., McElroy, D. B., & Tonry, J. L., 1985, (ISSN 0067-0049), vol. 59, Sept. 1985, p. 1-21.
[45] Berrier JOEL C. et al., 2013, ApJ, 769, 132.
[46] Nelson C. H., Whittle M.; 1995, Astrophys. J., Suppl. Ser. 99, 67.
[47] Hooft, G. (2009). Introduction to the Theory of Black Holes. Institute for Theoretical Physics / Spinoza Institute.
[48] Idiart, T. P., de Freitas Pacheco, J. A., Costa, R. D. D. 1996, AJ 112, 2541.
[49] Difference between dynamical masses and stellar masses of the bulge in spiral galaxies, Al-Baidhany, I.A., Chiad, S. S., Jabbar, W.A., Habubi, N. ., Abass, K. H., NeuroQuantology, 18(1), pp. 76-82, 2020.
[50] Al-Baidhany, I. A., Jabbar, W. A., Habubi, N. F., Chiad, S. S., Abass, K. H., A new relation between the absolute magnitudes of bulges and spiral arm pitch angles (p), NeuroQuantology 18(2), pp. 8-14, 2020.
[51] Bower G. A., Richstone D. O., Bothun G. D., and Heckman T. M.; 1993, Astrophys. J., 402, 76.
[52] Cappellari M., et al. 2006, MNRAS, 366, 1126.
[53] Bettoni D., Galletta G.; 1997. Astron. Astrophys. Suppl. Ser., 124, 61.
[54] Combes, F., Baker A. J., Schinnerer E., et al., 2009, A&A, 503, 73.
[55] Ma, J. 2001, Chin. J. Astron. Astrophys., 1, 395.
[56] Lake G., Dressler A.; 1986, Astrophys. J., 310, 605.

The Co-Evolution of Supermassive Black Holes and Their Hosts

Tareq Hashim Abbood[1], Wasmaa Jabbar[1], Ismaeel Al-Baidhany[1]*, Ashwaq Ali Ismail[2]

[1]Department of Physics, College of Education, Mustansiriyah University, Baghdad – Iraq
[2] Educational Rusafa Directorate-1
***Author for correspondence: E-mail: ismaeel_2000@uomustansiriyah.edu.iq.**

Abstract:

In this paper, we presented more information about the co-evolution of supermassive black holes and their hosts. This work divided into many sections: first, a short history of black holes, Second, Supermassive black holes and their hosts which contain: Bulge luminosity (L_{Bulge}), Spiral arm pitches angle (P), and Rotation velocity (V_{rot}).

المستخلص:

في البحث الحالي، قدمنا مزيدًا من المعلومات حول التطور المشترك للثقوب السوداء الهائلة ومضيفيها. ينقسم هذا العمل إلى عدة أقسام: أولاً، تاريخ قصير للثقوب السوداء، وثانيًا، الثقوب السوداء فائقة الكتلة ومضيفها الذي يحتوي على: لمعان الانتفاخ (L_{Bulge})، وزاوية ميل الذراع الحلزونية (P) وسرعة الدوران (Vrot).

A short history of black holes

Black Hole is a region of space-time where gravity is so strong that nothing, not even light, can escape from it (Wald 1984). The astonishing idea of that even light could not escape from a celestial object was first hypothesized in 1783 by John Michell. An amateur British astronomer wrote a letter to the Royal Society in 1783 which stated: "If the semi-diameter of a sphere of the same density as the Sun were to exceed that of the Sun in the proportion of 500 to 1, a body falling from an infinite height towards it would have acquired at its surface greater velocity than that of light, and consequently supposing light to be attracted by the same force in proportion to its vis inertiae, with other bodies, all light emitted from such a body would be made to return towards it by its own proper gravity" (Michell 1784).

In 1796, thirteen years after Michell's letter, the mathematician Pierre-Simon Laplace pointed out the same idea (Thorne 1994), which he referred to as a dark stars. At the time, the hypothesis was not widely accepted because it was not understood that light, as a wave, could be influenced by gravity (Laplace 1796).

Both scientists Mitchell and Laplace, understood the concept of escape velocity, which is the speed essential to escape an object's gravity. For escape velocity to exceed the speed of light, the mass of the parent body (in this case the dark star) has to be above a certain limit. Under these circumstances, light could not escape from the star's gravity (Michell 1784 & Laplace 1796). In 1916, Albert Einstein who was one of the most brilliant scientists in physics published his research on the General Theory of Relativity. The theory of General Relativity was expressed mathematically in a set of 10 extremely complex, coupled, nonlinear partial differential field equations. From these field equations, the idea of black holes could be derived. Einstein's equations showed that mass curves space and time and that gravity is a result of that curvature i.e., by bending space, mass (or gravity) influences the path a light ray travels (Einstein 1915). Furthermore, from Einstein's earlier work on Special Relativity, it was already known that the speed of light was a constant, as well as a universal speed limit.

In 1916, Karl Schwarzschild, a German physicist introduced the modern concept of the black hole. He discovered a mathematical solution to Einstein's field equations that

described the gravitational field of a point mass; this solution described the space and time around any spherical mass including the distance which known as the Schwarzschild Radius (r_s). This radius described the distance from the center of a sphere at which light cannot escape, where the mass of a black hole is entirely inside its Schwarzschild radius (Schwarzschild 1916).

In 1930, Subrahmanyan Chandrasekhar, an Indian physicist used special relativity and Fermi-Dirac statistics to derive the mass limit of a white dwarf (1.4 solar masses). Below this mass limit, a stellar remnant's gravitational collapse would be prevented by the Pauli exclusion principle. In other words, the electrons become degenerate, and the inward gravitational pull is balanced by outward electron degeneracy pressure. A white dwarf with a mass greater than this limit is unable to support itself against its own gravitational pull and crunches into a neutron star (Chandrasekhar 1931), an object that is supported by neutron degeneracy pressure. Later, in 1939, Robert Oppenheimer and his colleagues predicted that neutron stars have an upper mass limit of approximately three solar masses (the Tolman–Oppenheimer–Volkoff limit). Above this limit, gravity overcomes neutron degeneracy, and the object would collapse into black holes (Oppenheimer 1939). In 1968, the American physicist John Archibald Wheeler used the term "black hole" (Hooft 2009). By the 1960s, the concept of black holes had generated great interest among physicists, astronomers, and the other people as well.

Astronomers observed many types of black holes which can be classified into three groups: stellar mass black holes, intermediate mass black holes (IMBHs) and supermassive black holes (SMBHs) (Gebhardt & Rich 2005). The distinction between normal black holes and SMBHs is that normal black holes are believed to be the end point of stellar evolution for the most massive stars. The possible end products of stellar evolution are white dwarfs, neutron stars (usually observed as pulsars), and black holes. Stars that have masses greater than around 5 times the mass of the Sun may end up as a black hole (Valeri & Igor 1998). A SMBH is the largest type of black hole. They are typically found in the centers of galaxies, with masses in the range $\approx 10^5$ to $10^9 M_\odot$.

Supermassive black holes (SMBHs) are common at the center of all or most of galaxies (Mogorrian et al., 1998; Ferrarese & Merritt, 2000) as observed at high sensitivities and resolution with the Hubble Space Telescope (HST). In addition, their masses are in the range of hundreds of thousands to billions of solar masses (Kormendy & Richstone 1995; Richstone et al. 1998; Kormendy & Gebhardt 2001).

Over the last decade, studies of galaxies have led to the discovery that there are many strong or tight correlations locally between the masses of the SMBHs and the global properties of the spheroid components of their hosts. This suggests an intriguing link between galaxy formation and SMBH growth (Yuexing 2007). As a result, astrophysicists believe that the energy released by growing SMBHs play important role in shaping the properties of the structure of their host galaxies (Benson 2010; Fabian 2012).

There is increasing evidence which indicates that relationships between the mass of the SMBH and almost or all the possible parameters of the host galaxy bulges. This suggests that SMBHs play an important role in galaxy formation. Most galaxy bulges contain a central SBH whose mass strongly correlates with stellar velocity dispersion(σ_*) within the effective radius (r_e) (M_{BH}-σ_*); (Ferrarese & Merritt 2000; Gebhardt et al. 2000a; Tremaine et al. 2002) with the bulge luminosity or spheroid luminosity of the galaxy (L_{bul}) (M-L_{Bulge}; Kormendy & Richstone 1995; Magorrian et al. 1998; Marconi & Hunt 2003- hereafter, MH03;Häring & Rix 2004; Gültekin et al. 2009), with the bulge mass (M_{bulge}) (Magorrian et al. 1998, MH03, Häring & Rix 2004, hereafter HR04), and circular velocity (Ferrarese 2002), with the galaxy light concentration (Graham et al. 2001), the dark matter halo

(Ferrarese 2002), with the effective radius (Marconi & Hunt 2003), the Sersic index (Graham & Driver 2001, 2007), with the gravitational binding energy and gravitational potential (Aller & Richstone 2007), combination of bulge velocity dispersion, effective radius and/ or intensity (Aller & Richstone 2007), with the radio core length (Cao & Jiang 2002), and the inner core radius (Lauer et al. 2007).

As mentioned above, all scaling laws have led previous authors to the conclusion that SMBH, growth and bulge formation regulate each other (Hu 2009; Bettoni D. 1997). That means that mass of the SMBH is somehow tied to the structural parameters of the rest of the galaxy.

Using more sophisticated techniques of measuring the bulge luminosity such as two-dimensional image decompositions (e.g., McLure & Dunlop 2001; Wandel 2002, Hüring & Rix 2004, Hu 2009, Sani 2011), produces an even tighter correlation between SMBH mass and the host galaxy bulge parameters.

Kormendy & Richstone (1995) pointed out that the estimated central quiescent galaxy black hole masses of eight galaxies have a tight correlation with their host galaxy bulge luminosities. Magorrian et al. (1998) used the determinations for a BH sample of 32 nearby galaxies and suggested that the supermassive black hole mass, M_{BH}, is proportional to the bulge mass M_{bulge}, and luminosity of the host galaxy bulge, such that on average $M_{bh}/ M_{bulge} = 0.006$, with a rather large scatter about ±0.5 dex. Based on collections of M_{bh} values from various studies, Kormendy (2000) and H (2009) found a lower mean ratio of $M_{bh}/ M_{bulge} = 0.0015$-$0.002$, with a large scatter. These correlations imply that the processes which drive the more intimately linked with galaxy evolution and processes which drive SMBH growth (Erwin 2011).

The correlations between the mass of supermassive black holes (SMBHs) and properties of their host galaxies helped to understand the mechanism of nuclear energy by the formation and evolution of BHs (e.g., Rees1984; Tremaine et al. 2002).

Two strong correlations which can be used to estimate the SMBH mass are as following: First, the SMBH correlation with the bulge velocity dispersion. Gebhardt et al. (2000b, G00) and Ferrarese & Merritt (2000) investigated a significantly tighter correlation of M_{BH} with the bulge velocity dispersion σ_*, with some disagreement concerning the slope of this relation. (Ferrarese 2000, Gebhardt 2000;Tremane et al. 2002). Second the correlation with spiral arm pitch angle (Seigar et al. 2008), which has a lower intrinsic scatter, compared with other correlations.

Supermassive Black Holes and Their Hosts

1. Bulge luminosity (L_{Bulge})

The previous works to determine the bulge luminosity by Marconi & Hunt 2003, Gultekin et al. 2009, Hu 2009 and Sani 2011 attempted to compensate for the different methods and analysis techniques employed by several bands (V, K, 3.6um), like using the program GALFIT, and BUDDA. All of which arrive at different values for the slope of the classical bulges and pseudobulges galaxies $M_{BH} - L_{bulge}$ correlation.

Marconi & Hunt (2003, hereafter MH03) measure the bulge properties of 37 near-infrared galaxies by a two-dimensional bulge/disk decomposition program GALFIT (Peng et al.) 2002). They obtain tight M_{bh}-L_{bulge} and M_{bh}-M_d relations, where M_d is the bulge dynamical mass. Using more sophisticated techniques of measuring the bulge luminosity or dynamical modelingof the host galaxy, such as two-dimensional image decompositions (e.g., McLure & Dunlop 2001; Wandel 2002, Häring & Rix 2004, Hu 2009, Sani 2011), produces a tighter correlation between SMBHs and the host galaxy. Sani et al. (2011) investigated a new relations between SMBH masses and luminosity, bulge mass, effective

radius, velocity dispersion of the host galaxies, based on Spitzer/ IRAC 3.6 µm images of 35 spiral galaxies.

2. Spiral arm pitch angle (P)

The previous works have found that central SMBH mass is strongly related with spiral arm pitch angle of its host (Seigar et al. 2008, Davis et al. 2012, Berrier et al. 2013). Pitch angle is the angle between a line tangent to the arm in a spiral galaxy at a given radius and a line tangent to a circle at the same radius. The degree of twist of the spiral arms is a characterization of the pitch angle, where the galaxies with small and large pitch angles have tightly wound spiral arms and open arms respectively (Kennicutt 1981; Ma 2001; Savchenko & Reshetnikov 2011). The measurement of spiral arm pitch angle gives a measure of how tightly the spiral arms of a galaxy are wound. Since the creation of a morphological classification scheme of galaxies by Hubble (1926), authors have competed to investigate the wide correlation of the spiral and morphological type of the observed galaxies (e.g. Kennicutt 1981).

There are a variety of methods for measuring the pitch angle, some of them is based directly on the search for the angle between the tangents to the spiral arm and to the circumference centered at the galaxy nucleus. Also, some other methods are based on a Fourier analysis of the point's distribution in the spiral arms of a galaxy (Athanassoula 2005).

In these methods, the common feature is that they all require determining the orientation of galactic disks in space, which are described by the position angle and the inclination. For simplicity, the spiral galaxies are assumed as infinitely thin disks (i.e. a spiral galaxy is described as an oblate spheroid where the mathematics and result for the oblate spheroid is very similar), so the inclination angle (i) can be estimated by using the standard formulation for described by (Hubble 1926).

Although it is clear that an inclination angle derived by this equation is not exact enough, most researchers use it in their research (Ma 2001).

For this study we measured spiral arm pitch angle of a sample of nearly face-on spiral galaxies and used IRAF to determine the ellipticity and major-axis position angle in order to deproject the images to face-on by assuming that spiral galaxy disks are essentially circular. Then two-dimensional Fast Fourier Transform (2DFFT) was then applied to the deprojected images in order to measure the spiral arm pitch angles (Davis 2012 & Treuthardt 2012).

This method is in removes a great deal of the uncertainty present in the measurement of the pitch angles of spiral galaxies (Davis 2012).

Seigar et al. (2008) discovered a significant correlation between how tightly wound a spiral arm is and the SMBH mass in the nuclei of disk galaxies. This correlation provides a simplistic and relatively quick method to estimate SMBH mass by calculating spiral pitch angle of nearby galaxies (Davis et al. 2012; Berrier 2013).

Seigar et al. (2006a,b) and Davis et al. (2012) have concluded in their research that pitch angle does not depend measurably on the image's band, where they found consistency between B-band and NIR-band in the measurements of pitch angles by using 2D fast Fourier transform (2DFFT) analysis with logarithmic spirals.

3. Rotation velocity (V_{rot})

In 1981 and 2011, Kennicutt and Savchenko published two papers in which the relation between the spiral arm pitch angles, and its maximum rotation velocity were studied. They found a tight correlation between the spiral arm pitch angles and maximum rotation velocity.

Although, there is only a weak correlation between the pitch angles and the arm structures and with the bulge-to-disk ratio (Roberts 1976), a few researchers (as Kennicutt 1981, Savchenko 2011) have pointed out that a good correlation exists between the maximum rotation velocity and the pitch angle of the spiral arm, suggesting that the form of spiral pattern is principally set by kinematic parameters (Verschuur et al.1988).

References

Aller, M. C., & Richstone, D. O., 2007, ApJ, 665, 120.
ApJ, 597, 929.
Athanassoula E. 2005, MNRAS, 358, 1477.
Benson, A. J., & Bower, R. 2010, MNRAS, 405, 1573, ; Benson A. J.; Bower R. (2010) MNRAS, 405, 1573-1623.
Berrier JOEL C. et al., 2013, ApJ, 769, 132.
Bettoni D., Galletta G.; 1997. Astron. Astrophys. Suppl. Ser., 124, 61.
Chandrasekhar S., 1931, The Maximum Mass of IdealWhite Dwarfs, ApJ, 74, 81.
Gao, L., Jenkins, A., Kauffmann, G., Navarro, J. F. and Yoshida, N., 2006, MNRAS, 365, 11.
Davis, B. L., Berrier, J. C., Shields, D. W., Kennefick, J., Kennefick, D., Seigar, M. S., Lacy, C. H. S., & Puerari, I. 2012, ApJS, 199, 33,
Einstein A., 1915, Zur allgemeinen Relativitätstheorie, Sitzungsberichte der-
Elmegreen, B. G., Elmegreen, D. M., and Hirst, A. C.,2004., ApJ, 612, 191.
Erwin P. and Gadotti D. A., Advances in Astronomy,Volume 2012, Article ID 946368, doi:10.1155/2012/946368.
Ferrarese, L., and Merritt, D., 2000, ApJ 539, L9–L12.
Ferrarese, L., 2002., ApJ 578:90–97.
Gebhardt K. et al. 2000b, ApJ, 539, L13.
Gebhardt, K., Rich R. M. and Ho L. C., 2005, ApJ, 634, 1093.
Graham A. & S. P. Driver, 2007, ApJ, 655, 77.
Graham, A. W., Erwin, P., Caon, N., & Trujillo, I., 2001, ApJ, 563, L11.
Gültekin, K., et al. 2009, ApJ, 695, 1577.
Häring, N., and Rix, H.-W. 2004, ApJ, 604, L89.
Hooft, G. (2009). Introduction to the Theory of Black Holes. Institute for Theoretical Physics / Spinoza Institute.
Hu J., 2009, ArXiv:0908.2028;2009.
Hubble, E. P. 1926, ApJ, 64, 321.
Jedrzejewski, R. I. 1987, MNRAS, 226, 747.
Kennicutt, R. C. 1981, AJ, 86, 1847.
Kormendy, J. and Richstone, D. O., 1995, ARA&A, 33, 581.
Kormendy, J., & Fisher, D. B. 2005, RevMexA&A (Serie de Conferencias), 23, 101.
Kormendy, J., & Gebhardt, K. 2001, in AIP Conf. Proc. 586, 20th Texas.
Laplace P.-S., 1796, Exposition du Système du Monde. Imprimerie du Cercle-Social,
Lauer, T. R., Faber, S. M., Richstone, D., et al. 2007, ApJ, 662, 808,
Lauer. T. R., Tremaine S., Rich stone D., & Faber.Selection S. M., (2007), ApJ, 670, 249.
Ma, J. 2001, Chin. J. Astron. Astrophys., 1, 395.
MacArthur, L. A., Courteau, S., & Holtzman, J. A. 2003, ApJ, 582, 689.
Magorrian J., Tremaine S., Richstone D. et al., 1998, AJ, 115, 2285.
Mancini, L., & Feoli, A., 2012, A&A, 537, A48.
Marulli, F., Bonoli, S., Branchini, E., et al. 2008, MNRAS, 385, 1846.
McLure, R. J., & Dunlop, J. S. 2001, MNRAS, 321, 515.

Michell J., 1784,, On the Means of Discovering the Distance, Magnitude, &c. of the galaxies.
Oppenheimer, J.R.; Snyder, H. (1939). "On Continued Gravitational Contraction". Physical Review 56 (5): 455–459.
Peng et al. 2002, Astronomical Journal (AJ), 124, 266.
Rees, M.J., 1984a, Ann. Rev. Astr. Ap., 22, 471.
Richstone, D., et al. 1998, Nature, 395, A14.
Roberts, M.S., 1976. Comments Astrophys. 6:105
Robertson B., Cox T. J., Hernquist L., Franx M., Hopkins P. F., Martini P., Springel V. 2006a, ApJ, 641, 21.
Sani E., Marconi A, Hunt L. K., Risaliti G., 2011, MNRAS. 2011; 413:1479-94.
Savchenko S. S., and Reshetnikov V. P., 2011, Astron. Lett., 2011, Vol. 37, No. 12, pp. 817-825.
Savchenko S.S.,and V.P. Reshetnikov V.P., Mon. Not. R. Astron. Soc. 000, 1–11 (2013).
Schröder, M. F., Pastoriza, M. G., Kepler, S. O., & Puerari, I. 1994, A&AS, 108, 41.
Schwarzschild K., 1916, Über das Gravitationsfeld eines Massenpunktes nach der Ein-
Seigar, M. S., Bullock, J. S., Barth, A. J., & Ho, L. C. 2006a, ApJ, 645, 1012.
Seigar, M. S., Ho, L. C., & Barth, A. J. 2006b, Bulletin of the AAS, 38, 1190.
Seigar, M. S., Kennefick, D., Kennefick, J., & Lacy, C.H.S. 2008, ApJ, 678, L93.
Thorne 1994, pp. 123–124, Thorne, Kip S. (1994). Black Holes and Time Warps. Norton, W. W. & Company, Inc.
Tremaine, S., Gebhardt, K. and Bender, R., 2002, ApJ, 574, 740.
Treuthardt, P., Seigar, M. S., Sierra, A. D., Al-Baidhany, I., Salo, H., 2012.
Valeri. P. Frolov and Igor D. Novikov, 1998, Black Hole Physics: Basic Concepts and New Developments, Kluwer academic publishers.
Verschuur G. L. and Kellermann K. I., 1988, Galactic and Extragalactic Radio Astronomy, Berlin, Springer.
Wald, Robert M. (1984). General Relativity. University of Chicago Press.
Wandel, A. 2002, ApJ, 565, 762.

Study the Film of Hydroxyapatite Sputtering by Radio Frequency Plasma

Raheem Lafta Ali
Department of Physics, College of Education, Mustansiriyah University

Abstract

Titanium alloys have been used in biomedical applications because of their biocompatibility and mechanical properties. However, it has a possible toxic effect resulting from released vanadium and aluminum. The (HAP) coated Ti-6Al-4V alloy prevented releasing of undesirable vanadium and aluminum. The aim of this paper is to investigate the structural and mechanical properties of Ti-6Al-4V alloy by coating with (HAp). This coating was prepared by Radio Frequency Plasma Sputtering (RF) method. The thin film of HAp was improved the structural, composition, roughness and hardness were characterized by X-ray diffraction (XRD), Field Emission- Scan Electron Microscope (FE-SEM), atomic force microscope (AFM) and Vickers hardness respectively. The HAp films were crystalline structure. AFM showed different roughness of Ti-6Al-4V when uncoating and as-deposited HAp thin film.

المستخلص:

تستخدم سبائك التيتانيوم في التطبيقات الطبية الحيوية بسبب توافقها الحيوي وخصائصها الميكانيكية. ومع ذلك، يمكن أن يكون له تأثير سام ناتج عن إطلاق الفاناديوم والألمنيوم. الطلاء بمادة هدروكسيدالابتايت HAp تمنع إطلاق الفاناديوم والألمنيوم غير المرغوب فيهما. الهدف من هذا البحث هو دراسة الخصائص التركيبية والميكانيكية لسبائك Ti-6Al-4V المطلية بمادة HAp. تم تحضير هذا الغشاء الرقيق بطريقة رش البلازما بالترددات الراديوية (RF). تم تميز الهيكل والتركيب والخشونة بواسطة حيود الأشعة السينية (XRD)، المجهر الالكتروني الماسح الانبعاث الضوئي (FE-SEM)، ومجهر القوة الذرية (AFM) على التوالي. اظهرت النتائج لافلام الهدروكسيد الابتايت المطلية على السبيكة زيادة في الهيكل البلوري والخشونة والصلابة.

Introduction

The pure (cpTi) titanium and its alloys (such as Ti-6Al-4V) have been utilized for load bearing implants in dentistry, osteosynthesis and orthopedics due to their excellent biocompatibility, lightweight, high-strength, corrosion resistance and relatively low density[1]. These properties are not high enough to promote direct growth of the bone tissue or reduced the healing period and also Ti-6Al-4V alloy has a possible toxic effect resulting from released vanadium and aluminum [2]. A modification of metal surface has been employed to controlling tissue–titanium interactions; reduce the time for bone fixation and to prevent releasing of undesirable ions from the alloy [3]. These problems can be solved by using coating layers from bioinert materials as bioceramic HAp. Where, these materials are major inorganic component of human bone matrix and have a crystal structure identical to human bone and teeth minerals [4]. The coated thin films do not release ions into surrounding tissue of the body as do metallic biomaterials so that the coating layers on metallic biomaterials to prevent metallic ion release from orthopedic implants made of Ti6Al4V [5].

Many techniques, such as sol gel [6], Plasma electrolytic oxidation (PEO) [7], Electrophoretic deposition (EPD) [8], dip coating process[9], Ion Beam Assisted deposition (IBAD) [10], pulsed laser deposition (PLD) [11], plasma spray[12] and RF plasma magnetron sputtering can be used to deposit HA coatings. RF sputtering has several useful applications such as high RF sputtering rates of metals and insulators at low

pressures and provision of a DC bias on the substrate surface; RF could also be used to sputter insulators, semiconductors, and metal [13]. This technique can produce thin, uniform, dense coatings that are homogeneous in composition and structure [14].

Materials and Methods

Ti-6Al-4V samples used in this project were acquired from WG (William Gregor Ltd, London, United Kingdom). Circular (Ti-6Al-4V) samples are cut from rod with 30mm diameter and 3 mm thickness. All samples were abraded successively using SiC grinding paper with different grits started from 80 grit, and continued by 120, 230, 400, 600,800, 1000 and 1200 grit to obtain flat and scratch free surface and then polishing with diamond suspension start (1, 3, 6, 9, 15 µm) for a smooth and mirror polished surface. A grinding and polishing machine model: metaserv 250, buehler was utilized and then cleaned ultrasonically and washed with acetone and deionized water.

RF sputtering was utilized to prepare thin film of HA_P on Ti6Al4V alloy by using high purity (99.99%) HA_p target, a base pressure was evacuated to (1×10^{-5} mbar) by a combination of rotary and turbomolecular pump, then the argon gas (Ar) was passed till the pressure reached (1×10^{-3} mbar), and then the target was cleaned by pre-sputtering (with 30 W RF power) for 15 min. Ar (99.99%) was supplied as reactive gas at a flow ratio of 10 sccm. The distance between the substrate and the target was maintained at 80 mm for all deposition experiments with a RF power 200 W for 1 h duration. During the sputtering process, the temperature rose to approximately 80 because of self-heating.

Various techniques for surface analysis, structure examination and properties evaluation are used to investigate modified surface such as XRD analysis was carried out within the 20–60° range using a (PANalytical X'Pert PRO MRD PW3040, Almelo, Netherlands) with a Cu Kα radiation (λ= 1.541 Å) to identify the phases developed of specimens of Ti6Al4V alloy. FESEM was performed using a (Leo-Supra 50VP, Carl Zeiss, Germany) equipped with an energy dispersive X-ray (EDX) system.. Element distribution in the surface of treated and untreated samples is evaluated using EDX mapping. The surface roughness of the film was measured by using atomic force microscope (AFM) (Dimension Edge, Bruker) in the Tapping operation mode and a NanoDrive dimension edge-apping, image-processing software.

Result:

Figure (1) shows the X-ray diffraction patterns of uncoated Ti-6Al-4V alloy. It is observed in the figure1 that the lines of Ti-6Al-4V are 100, 002, 110, 101 and 102 at 2θ values 35.46°, 38.27°, 39.98°, 40.7° and 53.24°, respectively which belong to α and β phases of Ti-6Al-4V.

The coated thin films of HA_P appear lines of the XRD with the following Miller indices (hkl): (002), (100), (101), (110) and (102), they belong to the Ti-6Al-4V alloy and (313) belong to the HA_p phase which proved the data reported for hexagonal $Ca_5(PO_4)_3OH$ substrate as indicated in Figure (2). This result proved that the crystalline of HA_p layer became better.

Figures (3) and (4) display Field Emission Scanning Electron Microscope (FESEM) images of uncoated Ti-6Al-4V alloy and the coated with hydroxyapatite by radio frequency plasma deposition RF for 1h, respectively. The substrate sample in Figure (3) shows many scratches and smooth surface due to its grinding and polishing. The HA_p thin film was formed on whole surface of substrate. HA_p thin film was found to be the crystalline structure as indicated in Figure 4.

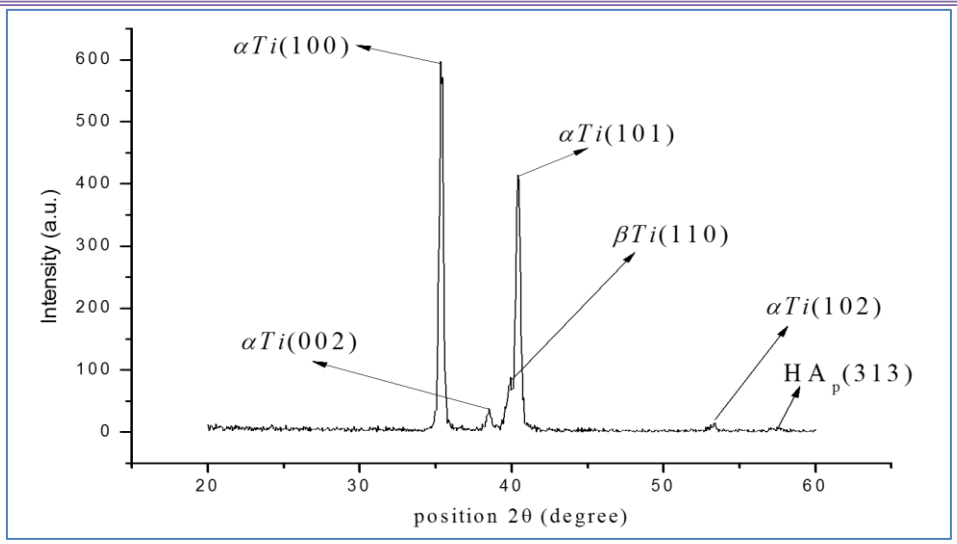

Figure 2: X-ray diffraction pattern of HA_P coated Ti-6Al-4V alloy.

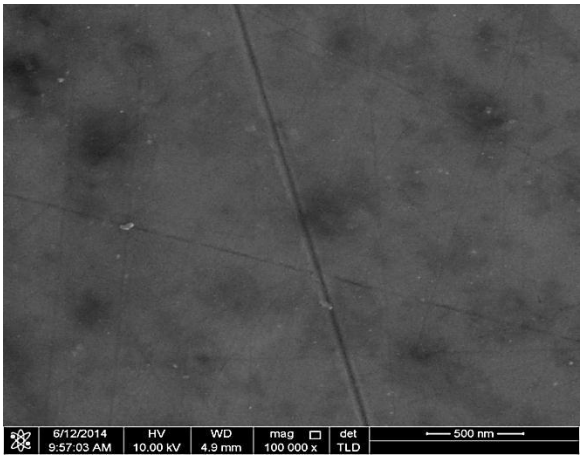

Figure 3: FESEM images of the untreated Ti-6Al-4V substrate

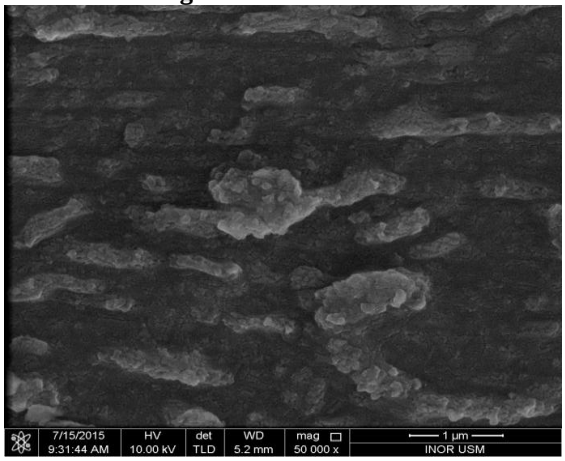

Figure 4: FESEM images of the HAP nanostructure deposited on Ti-6Al-4V substrate

Field-emission scanning electron microscope images of cross-sectional structure were used to measure the average layer thickness of HA_p on Ti-6Al-4V alloy was 257.4 as indicated in Figure 5.

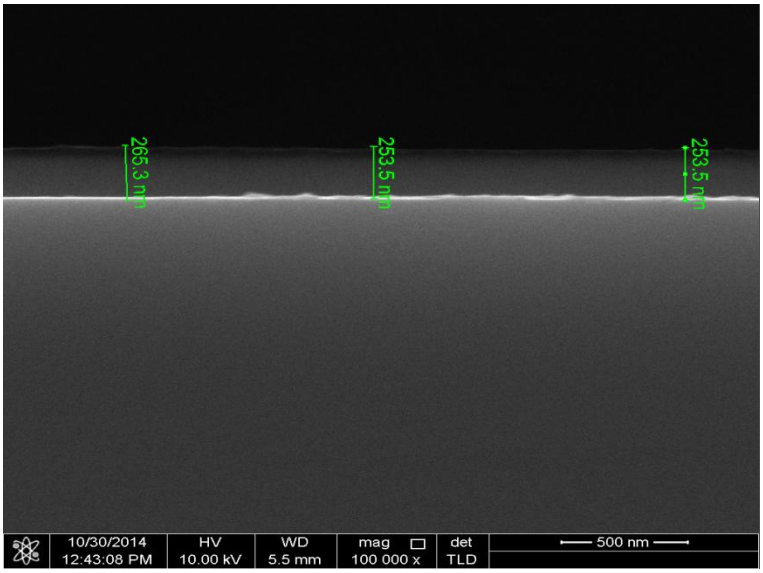

Figure 5: FESEM cross-section of the HAP nanostructure deposited on Ti-6Al-4V

Surface morphology plays an important role in biocompatibility materials. In order to study the influence of the surface properties on apatite layer formation and hardness properties, samples of uncoated Ti-6Al-4V and HA_P coated Ti-6Al-4V were used to characterize the change in the surface properties. A surface roughness of the samples after RF plasma treatment was conducted using atomic force microscope AFM.

The uncoated Ti-6Al-4V specimen in Figure 6 shows many scratches and smooth surface due to its grinding and polishing with low roughness. It was 6.54 nm. The surface topography of HA_P coatings on Ti-6Al-4V alloy is shown in Figure (7). The surface topography of the thin film was rough and showed layer with longitudinal grooves over the whole surface. The HA_P layer coated alloy had the crystalline phase resulted harder layer. The roughness values increased with HA_P coated Ti-6Al-4V alloy where they were 6.54 nm and 146 nm, respectively as indicted in Table (1).

Table 1: Morphological characteristics from AFM images for Ti-6Al-4V substrate And HAP coated Ti-6Al-4V alloy

Material	Roughness (nm)
Ti-6Al-4V substrate	6.54
HA_P coated Ti-6Al-4V alloy	146

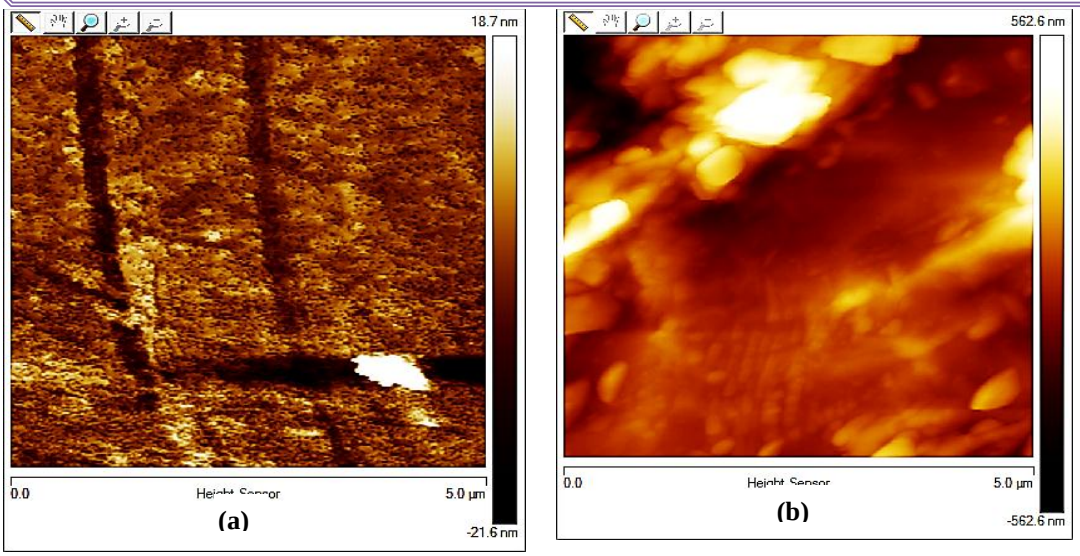

Figure 6: AFM images of Ti-6Al-4V substrates (a) 2D and (b) 3D

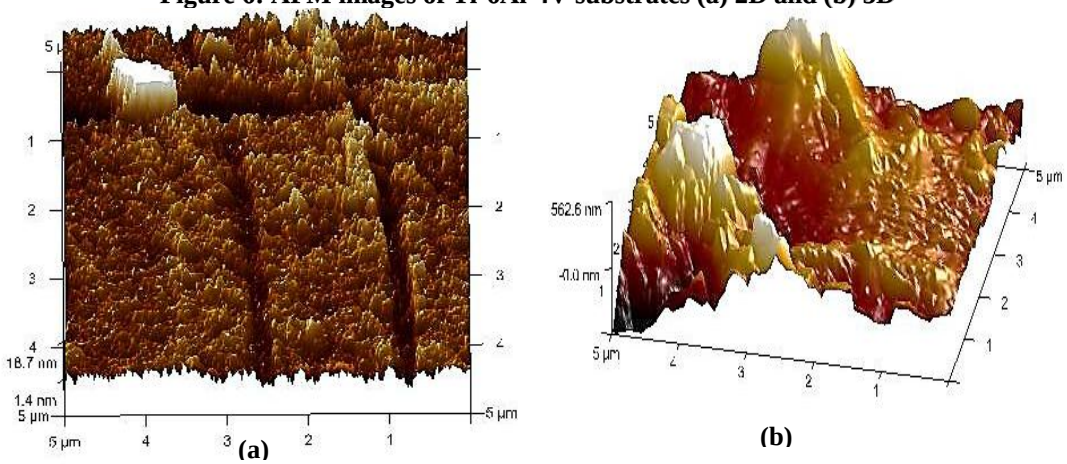

Figure 4.13: AFM images of HAP nanostructure on Ti-6Al-4V substrate with 5µm×5µm scanning area (a) 2D and (b) 3D

Conclusions:

The present study concludes that coating of Ti-6Al-4V alloy with HAp has crystalline phase. The surface topography of uncoated Ti-6Al-4V and the coated thin films of HA_P are significantly difference in surface roughness. The coating of HA_P on Ti-6Al-4V alloy is good method to form excellent hardness layer and prevent releasing of undesirable ions from the alloy.

References

[1] Gemelli, E., A. Scariot, N. Heriberto, 2007.Thermal characterization of commercially pure titanium for dental application. Mat. Res., 10-3.

[2] Elias, C. N., J. H. C. Lima, R. Valiev and M. A. Meyers, 2008. Biomedical applications of Titanium and its alloys. Biological Materials science.

[3] Richard, C., Petersen, 2015. Titanium Implant Osseointegration Problems with Alternate Solutions Using Epoxy/Carbon Fiber – Reinforced Composite. available in

PMC January 27.

[4] Baek-Hee lee and Naoto Koshizaki, 2008. Nanostructured hydroxyapatite/TiO2 Composite coating applied to commercially pure titanium by a co-sputtering technique. Nanotechnology, 19: 415303(7pp).

[5] Davide Zaffea, Carlo Bertoldib Ugo Consolob, 2004. Accumulation of aluminum in lamellar bone after implantation of titanium plates, Ti–6Al–4V screws, hydroxyapatite granules. Biomaterials, 25:3837–3844.

[6] Sajjad Jafari, Mehdi Mazar Atabaki, Jamaliah Idris, Comparative study on Bioactive coating of Ti-6Al-4V alloy and 316 L stainless steel. Association of Metallurgical Engineers of Serbia, (AMES), UDC: 669.295.5'71'292.018.8; 621.794.6.

[7] Yeung, Wk, G. C., Reilly, 2013. Matthew. In vitro biological response of plasma electrolytically oxidized and plasma-sprayed hydroxyapatite coating on Ti-6Al-4V alloy. Aug; 101(6): 939- 49. Doi: 10.1002/jbm. b32899.

[8] Corni, I., M. P. Ryan, A. R. Boecacelni, 2008.Electrophoretic deposition: from traditional ceramics to nanotechnology. J Eur ceram Soc., 28: 1353-1367.

[9] Seriven, L.E., 1988. Physics and applications of dip coating and spin coating. Better ceramics through chemistry 3rd 717-729.

[10] Zhi-Ye Qiu, Cen Chen, Xiu-Mei, Wang and In-Seop Lee, 2014. Advances In the surface modification techniques of bone-related implants for last 10 year. Regenerative Biomaterials, 67–79.

[11] Emanuel Axente, Gabriel Socol, 2022. Pulsed Laser Deposition of Thin Films: Recent Advances and Challenge. Coatings. MDPI.

[12] Mohseni, E., E. A. R. Zalnezhad, 2014. Comparative investigation on the adhesion of hydroxyapatite coating on Ti–6Al–4V implant: Bushroa, International Journal of Adhesion & Adhesives, 48: 238

[13] Yunzhi Yanga, B., Kyo-Han Kimc, Joo B. L. Onga, 2005. A review on calcium phosphate coatings produced using a sputtering process-an alternative to plasma spraying. Biomaterials, 26: 327

[14] Hee Ay Ching, Dipanker Choudhury, Md Julker Nine and Noor Azuan Abu Osman, 2014. Review effects of surface coating on reducing friction and wear of orthopaedic. Implants. Sci. Technol. Adv. Mater., 15: 014402 (21pp).

التحليل الجيواحصائي لبعض متغيرات الملوثات البيئية للمياه الجوفية باستخدام تطبيقات الجيوماتكس- قضاء الزوراء إنموذجا

د. عبير يحيى احمد، زينب جبر عواد
الجامعة المستنصرية – كلية التربية

المستخلص:

يهدف البحث الى الوقوف على المتغيرات الكيمائية والفيزيائية والبايلوجية وتاثيرها على تلوث المياه الجوفية، والتي تعد المصدر الرئيسي للمياه في منطقة الدراسة وعدم وجود بنى تحتية ومحطات لتصفية المياه ومعالجتها وبدور التقنيات الجغرافية الحديثة واستخدام أدوات التحليل الجيواحصائي داخل بيئة نظم المعلومات الجغرافية وتحديد الملوثات البيئية على المياه الجوفية مكانياً لوضع الحلول لمتخذي القرار وتشخيص المشاكل التي تواجه المياه الجوفية في المنطقة تم استخدام عدة أدوات للتحليل الاحصائي لقياس التلوث منها طريقة Krnging بجميع عملياتها وخوارزمياتها الستة التابعة Kringing ومنها (العادية والبسيطة والاحتمالية والعامة والدليل والاستدراكية) واستخدام أداة المسافة الموزونة (IDW) ليتم بناء قاعدة بيانات خرائطية بيئية لملوثات الابار في المنطقة.

Geostatistical Analysis of Some Variables of Underground Environmental Pollutants using Geomatics- Al-Zawra District is the Model

Abstract:

The research aims to identify the chemical, physical and biological variables and their impact on the pollution of groundwater, which is the main source of water in the study area, the absence of infrastructure and water purification and treatment plants, the role of modern geographic techniques and the use of geostatistical analysis tools within the GIS environment and the identification of environmental pollutants on groundwater Spatially to develop solutions for decision makers and diagnose the problems facing groundwater in the region, several tools were used for statistical analysis to measure pollution, including the Krnging method with all its operations and its six Kringing algorithms, including (normal, simple, probabilistic, general, evidence and remedial) and using the weighted distance tool (IDW) to build a database Environmental mapping of well pollutants in the region.

اولاً: المقدمة

تؤدي العديد من العوامل إلى تردي نوعية المياه الجوفية وتلوثها ومن أهمها تسرب المياه العادمة ورشحها للأسفل لتصل إلى المياه الجوفية وتلوثها أو وصولها لمصادر تغذية المياه الجوفية وتلوثه ليقوم بدوره بتلويث المياه الجوفية، اذ تحتوي هذه الملوثات على كميات وتراكيز عالية من النترات والبكتيريا والفيروسات والمعادن الثقيلة.

تعد ظاهرة التلوث البيئي من أهم المشكلات التي تهدد كوكبنا اليوم، نظراً لعلاقته بالنشاط البشري نتيجة فعاليات الإنسان التي قد تلحق الضرر بالبيئة الطبيعية، ومنها تلوث المياه الجوفية في مدينة بغداد الذي جاءَ انعكاساً للمتغيرات الجغرافية المتعددة مما يتطلب ضرورة تشخيص آثار تلك الملوثات (الطبيعية والبشرية) والعمل على دراسات متعمقة لإيجاد الحلول الناجزة من خلال وصف وتحليل وتباين قيم عناصر تلك المتغيرات التي تساهم في تلوث المياه.

ثانياً: منطقة الدراسة

يقع قضاء الزوراء (نطاق الدراسة) على بعد (10) كم شرقي مركز العاصمة بغداد في جانب الرصافة ويبلغ عدد سكانها قرابة (300.000) الف نسمة يتوزعون على مساحة تقدر بعشرات الكيلو مترات وهي منطقة سكنية مكتضة جدا بالسكان وتزاول العمل بمعامل الطابوق كسمة رئيسية للمنطقة ومنها جاءت التسمية. وجغرافيا تجدر الاشارة الى ان المنطقة جزء من السهل الرسوبي والتي تقع في منطقة الرصيف غير المستقر (Zone Mesopotamia) وأن اتجاه تدفق المياه الجوفية في جانب الرصافة تكون من أنماط التدفق من الشمال الشرقي باتجاه الجنوب والجنوب الغربي ومناخها من المناخات الشبه جافة لطيلة اشهر السنة ولا تمتلك المنطقة ماء اسالة او شبكة توزيع مياه نظامية بل تعتمد على حفر الابار نتيجة ارتفاع اسعار الماء الصالح للشرب الذي

يباع بخزانات سعة (100) لتر على سكان المنطقة في افضل الحالات كما تعاني المنطقة من تدهور حقيقي على صعيد جميع الخدمات وتراجع الوعي البيئي والصحي والاجتماعي وانحسار مستوى التعليم لادنى مستوياته نتيجة تفشي الفقر والبطالة في المنطقة كما موضح في الخريطة رقم (1). (3)

خريطة رقم (1): موقع منطقة الدراسة

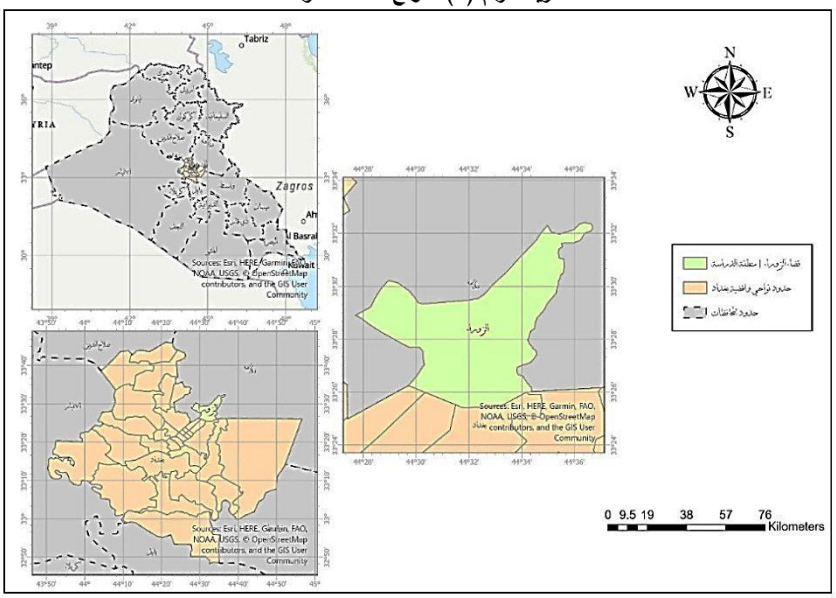

المصدر: من عمل الطالبة بالاعتماد على: 1. خرائط المساحة العسكرية وخرائط استحداث الأقاليم وزارة التخطيط
2. مخرجات برنامج ArcPro V 2.

ثالثاً: مشكلة البحث وتساؤلاته

يتجه العالم كله صوب التطور المعلوماتي التقني ومن الطرق الحديثة للتحليل الاحصائي ووصف الحالة وتفسيرها والوقوف على المشاكل بما يتلائم مع الأهداف ومع تحديد أماكن الابار وتحليل نتائج الملوثات مكانياً نضع عدة تساؤلات وحسب الاتي:

1. هل من الممكن بواسطة تطبيقات الجيوماتكس اعداد خرائط للملوثات وتحديد الملوثات مكانياً.
2. ما فائدة التحليل الجيو احصائي بواسطة تقانة وتطبيقات الجيوماتكس.
3. كيف يمكننا تحديد مواقع واعماق الابار ونسب التلوث فيها.

رابعاً: فرضية الدراسة

يمكن تحديد فرضيات البحث حسب الاتي:

1. التحليل الاحصائي بواسطة التقانات الحديثة تساهم في بناء نماذج تفاعلية إحصائية لملوثات الابار.
2. معرفة القيم والنسب بين الملوثات وكميات المياة وبذلك يمكن انتاج وتحليل خرائط للمنطقة.

خامساً: اهداف البحث

يهدف البحث للوصول الى عدة نقاط منها:

1. تحديد الملوثات البيئية مكانيا بطرق الاشتقاق المكاني المتعددة.
2. بناء نماذج واخراجها خرائطياً ومقارنتها مع المواصفات العالمية والعراقية لجودة المياه.
3. تحليل نتائج التحليل المكاني وتحديد الابار الأكثر تلوثاً ومعالجتها.

سادساً منهجية البحث

تعتمد الدراسة على المنهج العلمي الاستقرائي للتوصل الى فهم طرق الاشتقاق المكاني بعد تهيئة البيانات الحقلية واخراجها على شكل خرائط وتصنيفها مع استخدام المنهج التقاني الذي يعتمد على البرمجيات الحديثة المتعلقة بتطبيقات الجيوماتكس المكانية لاخراج نسب الملوثات بصوره خرائطية رقمية.

طريقة العمل

تم الاعتماد على بيانات الثلوث التي تم الحصول عليها من الدراسة الميدانية وتم تحليل العينات في مختبرات العلوم والتكنلوجيا مأخوذة من آبار المياه الجوفية الموجودة ضمن منطقة الدراسة بحسب احداثياتها باستخدام جهاز GPS نوع Garman وتم تحديد الميل الهيدروليكي ومستوى الماء الثابت والمتغير وانتاجية الابار من المياه تناسباً مع عدد سكان المنطقة ولكن وقوف الدراسة على مشكلة الملوثات ووضع الحلول لها كما هو موضح في الخريطة رقم (2 و3 و4).

خريطة (2) الميل الهيدروليكي وانتاجياتها لمياه ابار منطقة الدراسة

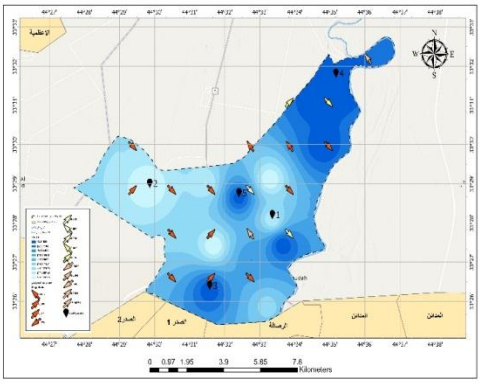

المصدر: من عمل الباحثين على بيانات المسح الميداني، باستخدام برنامج (ArcGIS Pro).

خريطة رقم (3) مستوى الماء الثابت لمياه ابار منطقة الدراسة

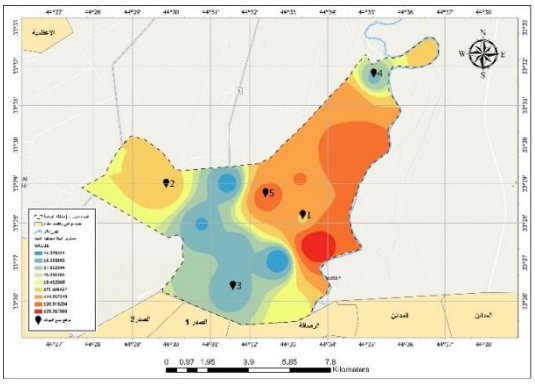

المصدر: من عمل الباحثين على بيانات المسح الميداني، باستخدام برنامج (ArcGIS Pro)

خريطة رقم (4) مستوى الماء المتغير

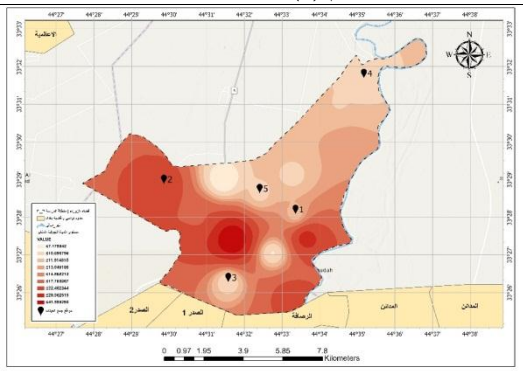

المصدر: من عمل الباحثين على بيانات المسح الميداني، باستخدام برنامج (ArcGIS Pro).

مفهوم التصنيف والتحليل الإحصائي Interpolation

عادة ما تكون زيارة كل موقع في منطقة الدراسة لقياس ارتفاع أو تركيز أو حجم ظاهرة ما أمرًا صعبًا أو مكلفًا. بدلاً من ذلك، يمكنك قياس الظاهرة في مواقع عينة متفرقة استراتيجيًا، ويمكن تعيين القيم المتوقعة لجميع المواقع الأخرى. ويمكن أن تكون نقاط الإدخال متباعدة بشكل عشوائي أو منتظم أو تستند إلى مخطط أخذ العينات.

ان الاشتقاق المكاني لمجموعة البيانات النقطية وبعض المقاييس، مثل الارتفاع أو التركيز أو المقدار (على سبيل المثال، الارتفاع أو الحموضة أو مستوى الضوضاء). تقوم أدوات الاشتقاق المكاني بعمل تنبؤات من قياسات العينة لجميع المواقع في مجموعة البيانات النقطية للمخرجات، سواء تم إجراء قياس في الموقع أم لا.

توجد طرق متنوعة لاشتقاق المكاني لكل موقع ؛ يشار إلى كل طريقة على أنها نموذج. مع كل نموذج، توجد افتراضات مختلفة للبيانات، ونماذج معينة أكثر قابلية للتطبيق على بيانات محددة – على سبيل المثال، قد يفسر أحد النماذج التباين المحلي بشكل أفضل من الآخر. ينتج كل نموذج تنبؤات باستخدام حسابات مختلفة.

تنقسم أدوات الاشتقاق المكاني عمومًا إلى طرق حتمية وإحصائية جغرافية:

تقوم طرق الاشتقاق المكاني بتعيين قيم للمواقع بناءً على القيم المقاسة المحيطة وعلى الصيغ الرياضية المحددة التي تحدد نتائج الدراسة وهي عدة طرق وعلى النحو الاتي: (Esri.com)

1. خاصية Kringing (4)

على الرغم من عدم وجود اتفاق حول العدد المثالي للأصناف، فأن هناك اتفاقاً عاماً مفاده، أن الإدراك الذهني للإنسان لا يمكن أن يميز بسهولة لأكثر من (11) تصنيفاً أو رمزاً للمساحة بالتدرج الرمادي، والذي يعتمد على الخصائص المختلفة للبيانات وتوزيعها وتميزها ودقتها المكانية وتوقيعها على الخريطة التي يتم إدراكها من قبل القارئ أو المستخدم، وأن هذه الخرائط يمكن تعميمها، وأن مثل هذه الخرائط (الخرائط الإحصائية) Statistical Maps المبنية على اصناف الفئات مختارة بحسب المقاييس والتصانيف الإحصائية (classify) لبيانات المعالم الجغرافية بأنماطها التوقيعية مع المحافظة على البيانات والمعالم المهمة اثناء تغيير المقياس من الكبير إلى الصغير بغية الوصول إلى التعميم الإحصائي لهذه البيانات لأجل تصنيف وتمثيل بيانات التلوث البيئي للمياه الجوفية في منطقة الدراسة ثم استخدام التحليل الإحصائي (Geostatistical Analysis) من خلال استخدام (خاصية Kringing) في تشخيص الآبار الاكثر كثافة للتلوث للعسرة ونسبة امتزاز الصوديوم ونسبة الاملاح المذابة وبناء نماذجها عن طريق مخرجات الطرق الستة لخاصية Kringing والتنبؤ في وسط كل منحنى، إذ يمكن أن تنتج خريطة للتنبؤ تمثل السطح كله. وأن طريقة كريكنج Kringing فهي احد طرق التحليل الإحصائي القائمة على التخمين المكاني، إذ تستخدم نماذج إحصائية تسمح بإنتاج خرائط متنوعة، وأن الهدف النهائي هو إنتاج سطح القيم المتوقعة، وتتضمن التنبؤات والخطأ القياسي للتنبؤ، فمثلاً إذا كنت تريد أن تعرف كفاءة التوقع، يمكن إنتاج ثلاثة أنواع مختلفة من خرائط التنبؤ، ويمكن النظر في الشكل التالي الذي يفترض ان التنبؤات تتوزع في ثلاثة مواقع من خلال استخدام عمليات المؤشرات الثابتة. (5)

سيكون التنبؤ في وسط كل منحنى، إذ يمكن أن تنتج خريطة للتنبؤ تمثل السطح كله، وبالنظر إلى الأرقام الثلاثة على اليسار، ستكون المنطقة تحت المنحنى على يمين الخط المتقطع في حالة التنبؤ قيمة التنبؤ أكبر من 1 وهكذا، وبالنظر إلى الأرقام الثلاثة على اليمين، إذا كنت ترغب في التنبؤ الكمي مع 5 في المئة من احتمال الى اليمين، وسوف تكون القيمة في خط متقطع (مأخوذ من المحور س)، مرة أخرى، يتغير توزيع التنبؤات لكل موقع الشكل (1) وهكذا، عند عقد ثابت الاحتمال، يتم إنتاج خريطة كمية للسطح كله، ويمكن إنتاج خرائط الخطأ القياسية للتنبؤ والخرائط الاحتمالية، كما في الصورة (1) والجدول (2) استخدام الأساليب ومخرجات طريقة كريكنج إلى جانب الافتراضات الرئيسة.

الشكل (1) التنبؤ بطريقة كريكنج

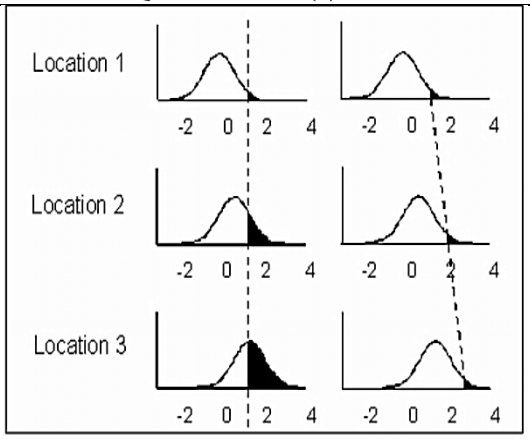

صورة (1) طريقة عمل خاصية كريكنج في ربط البيانات

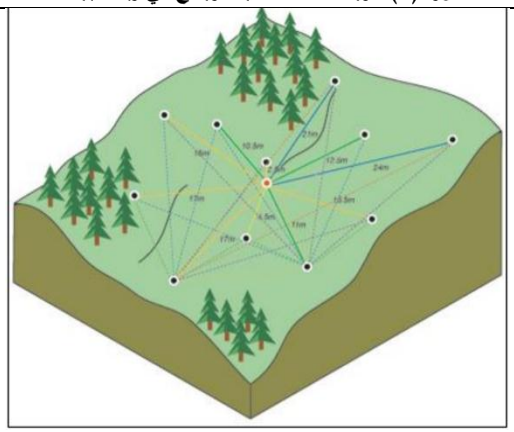

الجدول (2) أساليب ومخرجات طريقة كريكنج

طرق Kriging	التوقعات Predictions	الاخطاء القياسية للتنبؤ Prediction standard errors	الخرائط الكمية Quantile maps	الخرائط الاحتمالية Probability maps	الأخطاء القياسية للمؤشرات Standard errors of indicators
العادية Ordinary	X	X	X *	X *	
العامة Universal	X	X	X *	X *	
البسيطة Simple	X	X	X *		
الدليل Indicator				X	X
الاحتمالية Probability				X	X
الاستدراكية Disjunctive	X **	X **		X **	X **

X– إمكانية عمل الطريقة في الخاصية

*– يتطلب افتراض التوزيع العادي متعدد المتغيرات

**– الافتراض المطلوب للوضعية الثنائية المتغاير

تحتوي طريقة Kringing على ستة طرق وهي احدى طرق التحليل الإحصائي للاستكمال المكاني، تضع في حساباتها قياس الارتباط المكاني بين نقط التحكم المرصودة لوصف الاختلاف في السطح، لذلك فأن النقاط التي تكون متقاربة من بعضها لها درجات خاصة من العلاقات الرياضية الخاصة بها، وأما النقاط التي تكون منفصلة بشكل واسع فأنها تصبح مستقلة إحصائياً، ويتم حساب الارتباط المكاني بين النقط داخل محيط معين، أو بين نقط التحكم كلها، ثم يتم تحديد مواقع النقاط المستنبطة والقيم التي تحملها تبعاً لقيم الارتباط فيها (داود، 2012، 57)، وهذه الطرق هي: (6)

1. العادية Ordinary
2. البسيطة Simple
3. الاحتمالية Probability
4. العامة Universal
5. الدليل Indicator
6. الاستدراكية Disjunctive

تتطلب هذه الطرق بيانات ذات نمط توقيع نقطي (Point)، يحتوي على بيانات وفي صدد هذه الدراسة تم استخدام التلوث من العسرة Hardness ونسبة امتزاز الصيدوم SAR ومجموع الاملاح الذائبة TDS، وسيتم تطبيق هذا المتغير بجميع الطرق السابقة الذكر، ومن ثم معرفة اي الطرق أكثر كفاءة من خلال نمط التمثيل الذي تتخذه الظاهرة.

وفي هذا البحث تم استخدام طريقتين وهما الطريقة العادية Ordinary والطريقة العامة Universal لتطبيقهم على نسبة امتزاز الصوديوم Sodium absorption ratio (SAR) وعسرة المياه Hardness ومجموع المواد الصلبة الذائبة TDS للإبار حسب العينات من الدراسة الميدانية.

أولاً: الطريقة العادية Ordinary (7)

هي أحد الطرق الخاصة بـ Kringing التي تمتلك المرونة الكافية لتمثيل بيانات ثابتة، وتم تحديد عسرة المياه Hardness ونسبة امتزاز الصوديوم SAR، ونسبة الاملاح المذابة TDS للإبار حسب العينات من الدراسة الميدانية كما موضح في الخرائط رقم (5-19) والتي تمثل كل من (Spherical، Circular، linear، Exponetial، Gaussian).

- عسرة المياه Hardness

خريطة رقم (5) خريطة العسرة Hardness حسب الطريقة العادية Ordinary Spherical

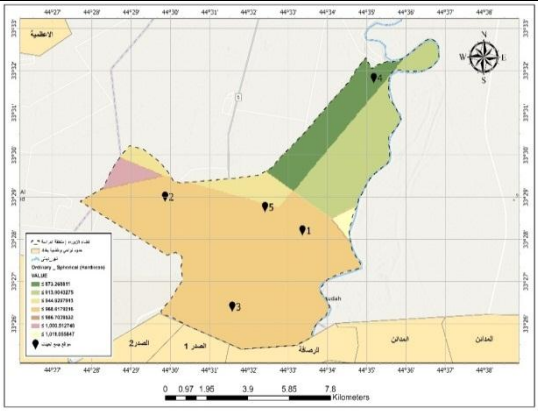

المصدر: من عمل الباحثين على بيانات المسح الميداني، باستخدام برنامج (ArcGIS Pro).

خريطة رقم (6) خريطة العسرة Hardness حسب الطريقة العادية Ordinary Circular

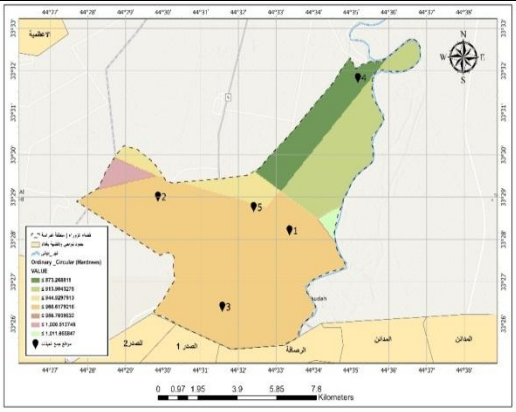

المصدر: من عمل الباحثين على بيانات المسح الميداني، باستخدام برنامج (ArcGIS Pro).

خريطة رقم (7) خريطة العسرة Hardness حسب الطريقة العادية Ordinary linear

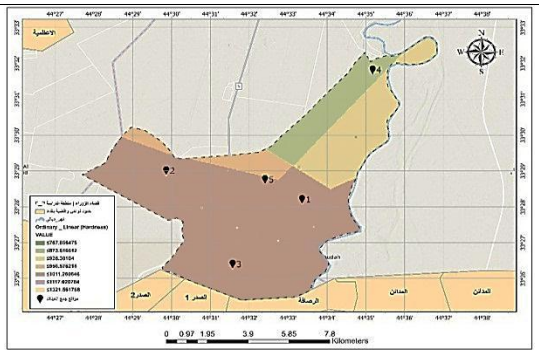

المصدر: من عمل الباحثين على بيانات المسح الميداني، باستخدام برنامج (ArcGIS Pro).

خريطة رقم (8) خريطة العسرة Hardness حسب الطريقة العادية Ordinary Exponetial

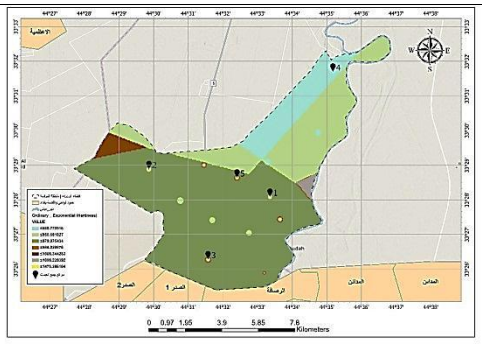

المصدر: من عمل الباحثين على بيانات المسح الميداني، باستخدام برنامج (ArcGIS Pro).

خريطة رقم (9) خريطة العسرة Hardness حسب الطريقة العادية Ordinary Gaussian

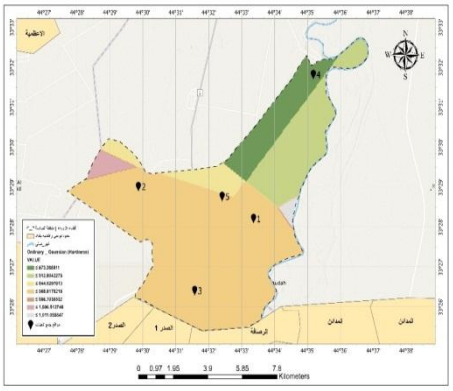

المصدر: من عمل الباحثين على بيانات المسح الميداني، باستخدام برنامج (ArcGIS Pro).

- نسبة امتزاز الصوديوم SAR

خريطة رقم (10) خريطة SAR حسب الطريقة العادية Ordinary Spherical

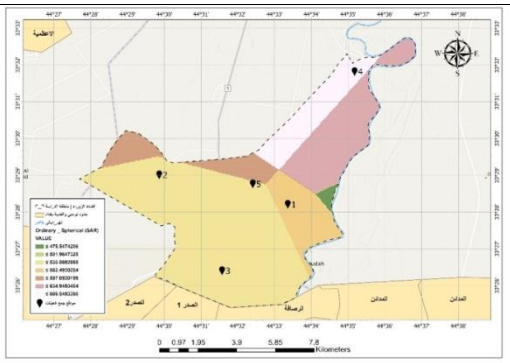

المصدر: من عمل الباحثين على بيانات المسح الميداني، باستخدام برنامج (ArcGIS Pro).

خريطة رقم (11) خريطة SAR حسب الطريقة العادية Ordinary Circular

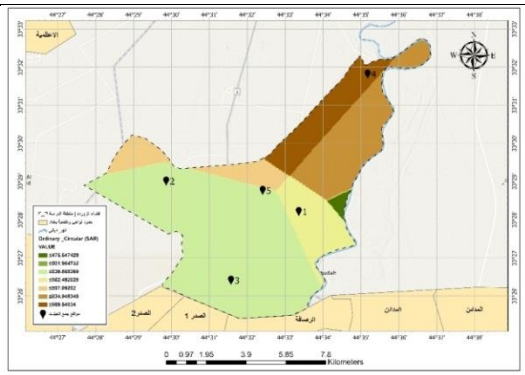

المصدر: من عمل الباحثين على بيانات المسح الميداني، باستخدام برنامج (ArcGIS Pro).

خريطة رقم (12) خريطة SAR حسب الطريقة العادية Ordinary linear

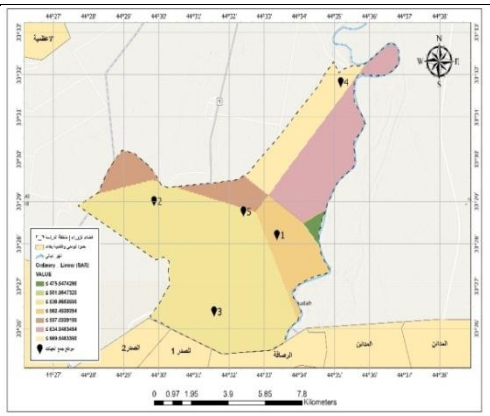

المصدر: من عمل الباحثين على بيانات المسح الميداني، باستخدام برنامج (ArcGIS Pro)

خريطة رقم (13) خريطة SAR حسب الطريقة العادية Ordinary Exponetial

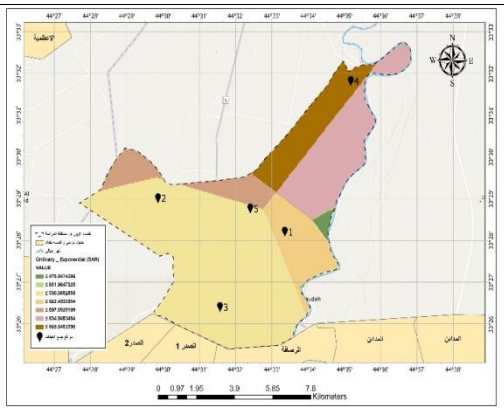

المصدر: من عمل الباحثين على بيانات المسح الميداني، باستخدام برنامج (ArcGIS Pro).

خريطة رقم (14) خريطة SAR حسب الطريقة العادية Ordinary Gaussian

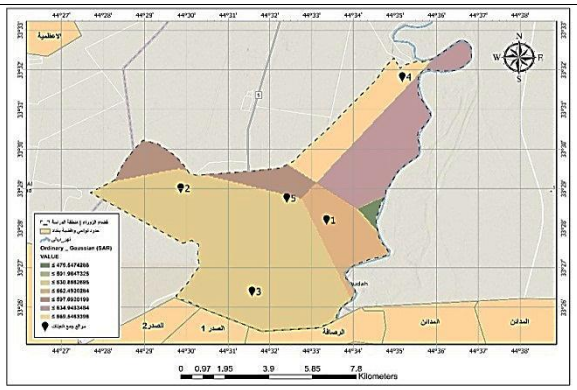

المصدر: من عمل الباحثين على بيانات المسح الميداني، باستخدام برنامج (ArcGIS Pro).

- نسبة الاملاح المذابة TDS

خريطة رقم (15) خريطة TDS حسب الطريقة العادية Ordinary Spherical	خريطة رقم (16) خريطة TDS حسب الطريقة العادية Ordinary Circular
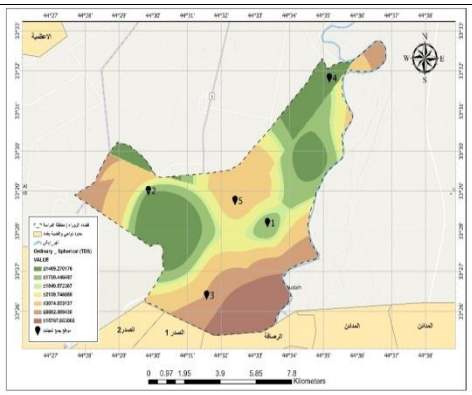	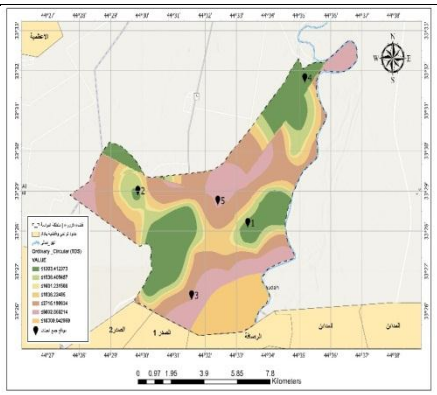
المصدر: من عمل الباحثين على بيانات المسح الميداني، باستخدام برنامج (ArcGIS Pro).	المصدر: من عمل الباحثين على بيانات المسح الميداني، باستخدام برنامج (ArcGIS Pro).
خريطة رقم (17) خريطة TDS حسب الطريقة العادية Ordinary linear	خريطة رقم (18) خريطة TDS حسب الطريقة العادية Ordinary Exponetial
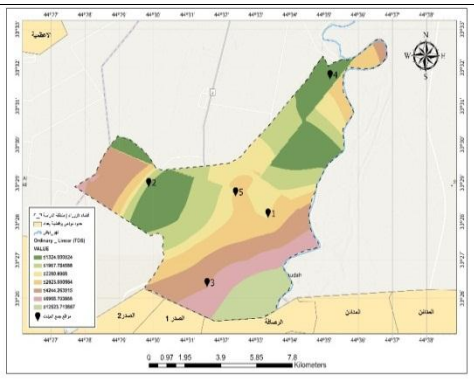	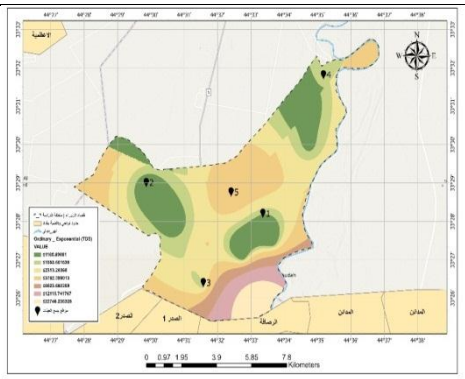
المصدر: من عمل الباحثين على بيانات المسح الميداني، باستخدام برنامج (ArcGIS Pro).	المصدر: من عمل الباحثين على بيانات المسح الميداني، باستخدام برنامج (ArcGIS Pro).

خريطة رقم (19) خريطة TDS حسب الطريقة العادية Ordinary Gaussian

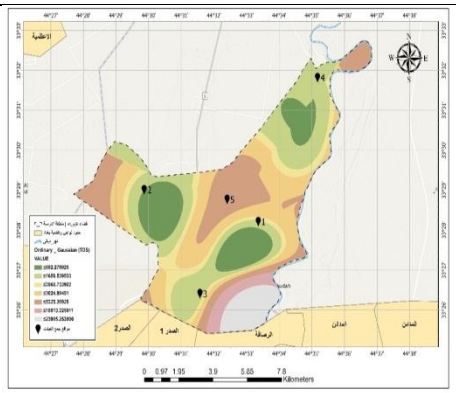

المصدر: من عمل الباحثين على بيانات المسح الميداني، باستخدام برنامج (ArcGIS Pro).

ثانياً: الطريقة العامة Universal

هي احدى الطرق التي تعتمد على النمط العشوائي في التمثيل، إذ تفترض خط عشوائي منحنى يمتد لمسافة طويلة، وتم تحديد عسرة المياه Hardness وامتزاز الصوديوم SAR مجموع المواد الصلبة الذائبة TDS للإبار حسب العينات من الدراسة الميدانية كما موضح في الخرائط رقم (20-25) والتي تمثل كل من Linear driftQuadratic drift.

- عسرة المياه Hardness

خريطة رقم (20) خريطة العسرة Hardness حسب الطريقة العامة Linear drift Universal

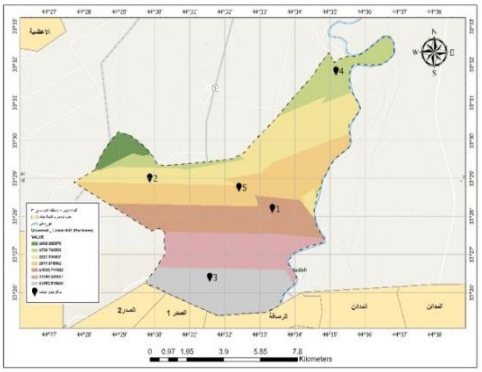

المصدر: من عمل الباحثين على بيانات المسح الميداني، باستخدام برنامج (ArcGIS Pro).

خريطة رقم (21) خريطة العسرة Hardness حسب الطريقة العامةQuadratic drift Universal

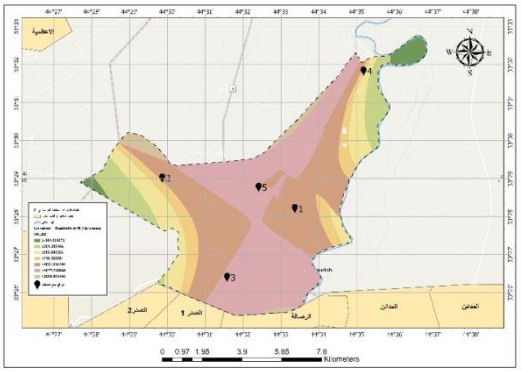

المصدر: من عمل الباحثين على بيانات المسح الميداني، باستخدام برنامج (ArcGIS Pro).

- نسبة امتزاز الصوديوم SAR

خريطة رقم (22) خريطة SAR حسب الطريقة العامة Linear drift Universal

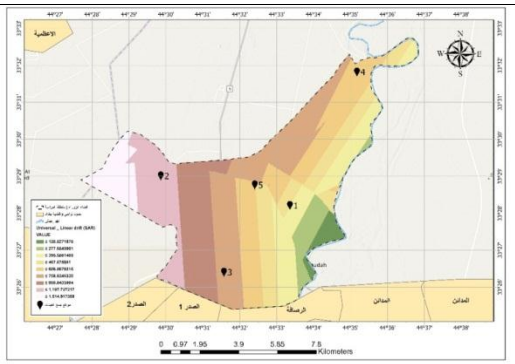

المصدر: من عمل الباحثين على بيانات المسح الميداني، باستخدام برنامج (ArcGIS Pro).

خريطة رقم (23) خريطة SAR حسب الطريقة العامة Quadratic drift Universal

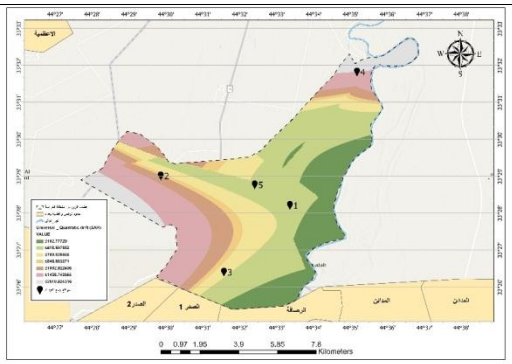

المصدر: من عمل الباحثين على بيانات المسح الميداني، باستخدام برنامج (ArcGIS Pro).

- مجموع الاملاح المذابة TDS

خريطة رقم (24) خريطة TDS حسب الطريقة العامة Linear drift Universal

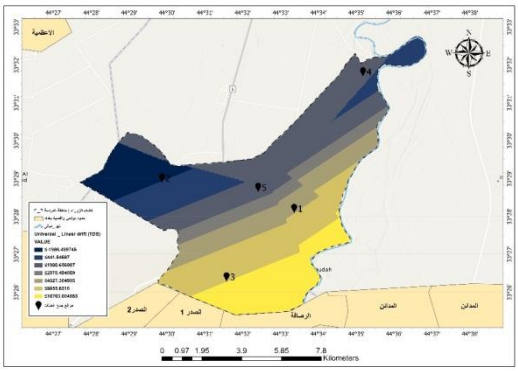

المصدر: من عمل الباحثين على بيانات المسح الميداني، باستخدام برنامج (ArcGIS Pro).

خريطة رقم (25) خريطة TDS حسب الطريقة العامة Quadratic drift Universal

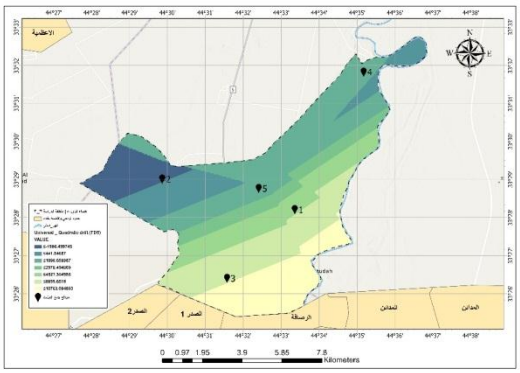

المصدر: من عمل الباحثين على بيانات المسح الميداني، باستخدام برنامج (ArcGIS Pro).

طريقة المسافة الموزونة المعكوسة Inverse Distance Weighted (IDW)

تمثل هذه الطريقة مفهوم الارتباط المكاني، اذ تعتمد على تقدير ارتفاع النقطة المجهولة عن طريق حساب المسافات من النقطة الى النقاط الأخرى المعروفة، وتمت المسافة الاوزان بان تفترض بان القيمة الأقرب الى النقطة المجهولة لها تأثير أكبر على القيمة اذ انها لا تأخذ بالحسبان أي اتجاهات، بل قيم النقاط المعلومة والمسافات التي تفصلها عن النقاط المجهولة، فالنقاط المعلومة الأقرب لها تأثير اكبر من النقاط البعيد. عند استخدام طريقة مقلوب المسافة الموزونة فان القيم المشتقة لا تتجاوز القيم المستخدمة، وهذا الأسلوب له ارتباط وثيق بالمسافة، اذ ان القيم تتناقص مع المسافة بمعنى ان القيم المتنبئة لن تتجاوز قيم العينات المعلومة فالتنبؤ سوف يكون محصورا بين القيم المعلومة. وتنتج نقاط مكورة (Bulls Eyes) حول المواقع.

قام الباحث بتطبيق هذه الطريقة على كل SAR وعسرة المياه Hardness ومجموع المواد الصلبة الذائبة TDS للإبار حسب العينات من الدراسة الميدانية كما موضح في الخرائط رقم (26 و27 و28) والتي تمثل كل من (Hardness، TDS،SAR).

- عسرة المياه Hardness

خريطة رقم (26) خريطة العسرة Hardness حسب الطريقة IDW

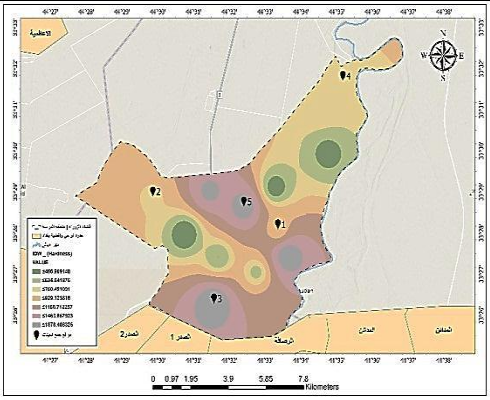

المصدر: من عمل الباحثين على بيانات المسح الميداني، باستخدام برنامج (ArcGIS Pro).

خريطة رقم (27) خريطة SAR حسب الطريقة IDW

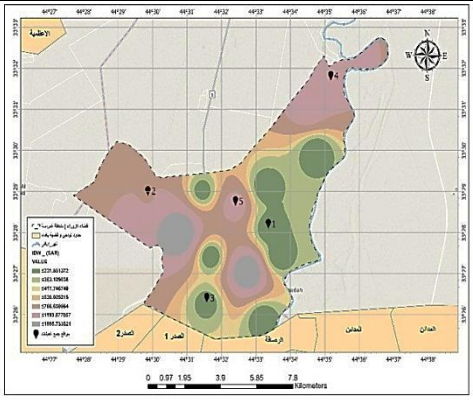

المصدر: من عمل الباحثين على بيانات المسح الميداني، باستخدام برنامج (ArcGIS Pro).

خريطة رقم (28) خريطة TDS حسب الطريقة IDW

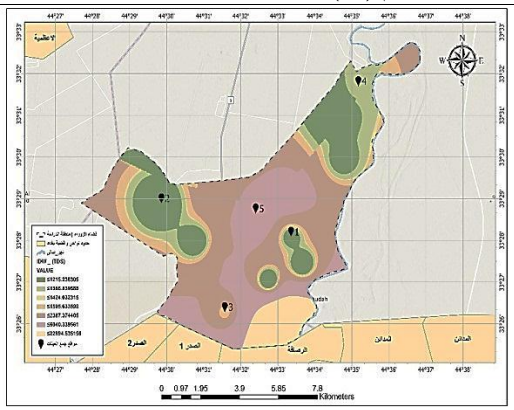

المصدر: من عمل الباحثين على بيانات المسح الميداني، باستخدام برنامج (ArcGIS Pro).

الدراسة الميدانية والمطابقة

من خلال الدراسة للمياه الجوفية في قضاء الزوراء تم تحديد الخواص الفيزيائية والكيميائية اذ أظهرت النتائج أن درجة حرارة المياه تعتمد على الموسم وكذلك على الخصائص الهيدروجيولوجية للطبقات الحاملة للمياه، في حين كان كل من الاس الهيدروجيني pH والإيصالية الكهربائية ECe كانت جيدة وتصنف المياه على أنها جيدة إلى يمكن استخدامها. أما وجود اللون نعتقد أن السبب يعود إلى احتوائها على ايون الحديد والمنجنيز الذائب وبقايا مواد عضوية.

العناصر الكيميائية التي تؤثر على المياه الجوفية

مقاييس منظمة الصحة العالمية (WHO) والمقاييس العراقية (IQS) لمياه الشرب هي المياه الصالحة للشرب والاستخدامات المنزلية، والمياه المستخدمة في الصناعات. الغذاء الذي يتوافق في خصائصه مع متطلبات المواصفة القياسية الدولية كما هو مبين بالجدول رقم (1).

ملحق رقم (1) المواصفات العالمية والعراقية والامريكية لتحديد صلاحية مياه الشرب

المعامل Parameter	مواصفات منظمة الصحة العالمية WHO،1996 (ملغم. لتر$^{-1}$)	المواصفات القياسية العراقية IQS,1996(ملغم. لتر$^{-1}$)	مواصفات وكالة حماية البيئة الامريكية USEPA,1975(ملغم. لتر$^{-1}$)
TDS	1000	1000	500
pH	6.5-9.5	6.5-8.5	-
العسرة الكلية (TH)	-	500	500
K^{+}	-	-	20
Na^{+}	200	200	200
Mg^{2+}	50	50	125
Ca^{2+}	200	150	200
Cl^{-}	250	250	250
SO_4^{2-}	250	250	250
HCO_3^{-}	-	-	500
NO_3	50	50	-

FAO standards (chemical properties)

ملحق رقم (2) مواصفات منظمة الزراعة والاغذية (1989،FAO) لتحديد صلاحية مياه الري

ت	طبيعة المشكلة	قيمة الحد الادنى من الاستعمال		
		لاتوجد	قليلة – متوسطة	شديد
1	الملوحة (EC) $ds.m^{-1}$ عند 25°م	0.7 >	3.0 – 0.7	3 <
2	مجموع الاملاح الذائبة (ppm)	450	2000 – 450	2000 <
	نسبة امتزاز الصوديوم	قيمة التوصيل الكهربائي EC		
	3 – 0	0.7<	0.2 – 0.7	0.2 >
	6 –3	1.2 >	0.3 –1.2	0.3 >
	12 – 6	1.9 <	0.5 –1.9	0.5 >
	20 –12	2.9 <	1.3 –2.9	1.3 >
	40 –20	5 <	2.9 –5	2.9 >
3	التأثيرات الجانبية للايونات			
	الصوديوم($meq.L^{-1}$) الري السطحي	3 >	9 –3	9 <
	الكلوريد ($meq.L^{-1}$) الري السطحي	4 >	10 – 4	10 <
4	التأثيرات العرضية الاخرى			
	النترات$N-No_3$ ($meq.L^{-1}$)	0.5 >	30 –5	30 <
	البيكاربونات ($meq.L^{-1}$)	1.5 >	8.5 –1.5	8.5 <
	درجة التعادل pH	8.4 – 6.5	-	-

جدول رقم (4) ملوثات الاثار البيئية

OBJECTID	X	Y	TDS	WATER_TYPE	SAR	HARDNESS
1	44.55318	33.43153	22901	CHLORIDIC	27.92	1122.64
5	44.51286	33.46629	700	SULPHATIC	1996	239.19
6	44.55597	33.46801	880	BICARBONA	7.8	796.32
7	44.52418	33.48343	1950	CHLORIDIC	108	1577.9
8	44.52822	33.4569	2406	SULPHATIC	19.9	466.32
9	44.49768	33.48133	488	BICARBONA	757	736.43
10	44.52618	33.4379	1444	CHLORIDIC	107.33	1878.73
11	44.55469	33.48506	3344	SULPHATIC	19.2	322.33
12	44.57911	33.49897	950	BICARBONA	4.2	368.02
13	44.57538	33.51729	580	CHLORIDIC	1065	743.14
14	44.58624	33.52815	1308	CHLORIDIC	1028.8	753.49
15	44.54586	33.45079	420	SULPHATIC	1996	574.82
16	44.56079	33.45724	450	BICARBONA	6.1	1795.53
17	44.5401	33.47726	3593	CHLORIDIC	1026.58	1733.43

4.5 الخصائص الكيمائية

لقد لوحظ كذلك بأن الأس الهيدروجيني لجميع عينات المياه في فصل الصيف كان يتراوح بين (7.3–7.9)، مما يعطي أنطباعا واضحا على أن هذه المياه تميل إلى الصفة القاعدية الضعيفة. اما في فصل الشتاء كان يتراوح بين (7.3–8.11)، مما يعطي أنطباعا واضحا على أن هذه المياه تميل إلى الصفة القاعدية القوية.

بينت القراءات المسجلة لمجموع الأملاح الذائبة أنها كانت تتراوح طيلة فترة الفحص بين (1325–2855)، والتوصيلية الكهربائية تراوحت بين 1920–2368 (cm/µs) (2.21–4.61) وبذلك يتضح الفرق بينها وبين ما هو مسموح به من قبل منظمة الصحة العالمية والتي أقرت بأن أعلى تركيز مسموح به يجب أن لا يتجاوز 1000ppm لمجموع الأملاح الذائبة و (1600cm/µs) للتوصيلية الكهربائية، وعليه فأن هذه المياه غير صالحة للأستهلاك وإن إرتفاع قيم التوصيلية الكهربائية يعود إلى زيادة تركيز الأملاح الذائبة وذلك لتماس المياه مع التربة، اذ أن التوصيلية الكهربائية تعطينا دليلا واضحا على وجود القوة الأيونية للمحلول المائي والذي يعتمد بصورة أساسية على كمية الأملاح الذائبة ويتناسب هذين المتغيرين تناسبا طرديا، او الذي يبين انخفاض قيمة TDS في الأشهر المطرية نتيجة زيادة نسب المياه المتغلغلة إلى داخل التربة ثم إرتفاعها كذلك بحد أعلى في الأشهر الحارة نتيجة إرتفاع معدلات التبخير.

أما الأشكال التالية توضح تغاير هذه التراكيز مع فترة الفحص، تبرز العلاقة بين مجموع الأملاح الذائبة وكلا من الكالسيوم والصوديوم والمغنيسيوم والبوتاسيوم والكلوريدات والكبريتات يبين أن مجموع الأملاح الذائبة قد شهدت أزديادا ملحوظا خلال فترة الأشهر الحارة والذي يمكن ان نعزوه الى إرتفاع درجة الحرارة وإزدياد نسبة تبخر المياه. وعليه يمكن توقع تسجيل تراكيز عالية للعسرة الكلية في تلك النماذج والتي تراوحت بين (767-1327) ppm كما موضح في الشكل رقم (4 و8)، ويعزز إرتفاع العسرة الكلية إلى إرتفاع تركيز أيون الكبريتات في مياه الآبار.

الاستنتاجات:

توصلت الدراسة إلى جملة من النقاط أهمها:

1- التطرق إلى المفاهيم والمعادلات العامة لجميع مؤشرات كريكنج ولأول مرة من خلال ترمة بيئة النظام.

لكل طريقة من الطرق معادلة ونمط تمثيل وتخمين خاص يعكس الافتراض المتوقع عند تمثيل الخط المتقطع الافتراضي.

2- عند التطرق إلى جميع المؤشرات توصل البحث إلى أن الطريقة الاحتمالية أرب إلى الدقة، وذلك لاعتمادها على الارتباط القائم على خوارزمية معقدة في داخل النظام.

التوصيات:

1- ضرورة التعمق في المعادلات المعقدة لكل طريقة وتطبيقها يدوياً من خلال الذهاب إلى أهل الاختصاص وفك الرموز الخاصة به كي يتسنى لنا الفهم الأكثر لكل طريقة.

2- اختيار آبار كثيرة في منطقة الدراسة ومن ثم العمل على طريقة كريكنج والخروج إلى نتائج وبعد ذلك أخذ عينات قليلة وتمثيلها أيضاً بنفس الطريقة ومقارنة النتائج ومعرفة أيهما أقرب إلى الواقع لأن العينات تتناسب دقتها طردياً مع زيادتها فكلما زاد عدد العينات زادت الدقة وكلما قلت زادت نسبة التعميم وارتفعت نسبة الخطأ.

3- يمكن استخدام تقنيات التحليل الإحصائي المكاني وفق آلية الاستكمال كأدوات لتحليل طبيعة توزيع المياه الجوفية وتباينها المكانية والزمانية، وتعطي نتائجها كارتوكرافياً لا تقل قيمتها عن نتائج خرائط التمثيل النسبي Choropleth، إلا أن الخصائص الإحصائية لقيم قواعد البيانات مثل طبيعة التوزيع والقيم المتطرفة قد تؤثر على دقة نماذج السطح.

المراجع:

(1) القصاب، عمر عبد الله، التعميم الآلي في نظم المعلومات الجغرافية، رسالة ماجستير غير منشورة، جامعة الموصل، كلية التربية للعلوم الإنسانية، قسم الجغرافية، 2010.

(2) بدن، التعميم الخرائطي النموذجي: هو عملية اشتقاق انموذج مكاني للبيانات المعممة عن البيانات الأصلية مع الحفاظ على كمال ودقة محتواها اثناء تغيير المقياس.

(3) رشيد، ذكرى، التوزيع الجغرافي للمرائب المختارة في بغداد، الرصافة، رسالة ماجستير (غير منشورة)، كلية التربية للبنات، جامعة بغداد، 2002.

(4) جميع المفاهيم التي سترد في متن هذا البحث والاشكال هي من بيئة نظام Arc GIS.v.10.3 ولا حاجة لذكرها وتكرارها في كل صفحة.

(5) داود، جمعة محمد، أسس التحليل المكاني في اطار نظم المعلومات الجغرافية GIS، ط1، مكة المكرمة، المملكة العربية السعودية، 2012.

(6) Anselin, L, spatial statistical (modeling in GIS Invironment, In Maguire, D. J, etal. Ceds) GIS, Spatial Analysis and modeling, 2005.

(7) George F. Jenks. generalization in Amman, Jordan statistical mapping, annals of the association of American geographer, 1963.